Helmholtz-Institut für Strahlen- und Kernphysik

der Rheinischen Friedrich-Wilhelms-Universität Bonn

Simulations with the $\overline{\text{P}}$ANDA Micro-Vertex-Detector

Dissertation
zur Erlangung des akademischen Grades
Doctor rerum naturalium
(Dr.rer.nat)

vorgelegt von

Dipl.-Phys. Ralf Kliemt

geboren in Suhl

2012

Angefertigt mit der Genehmigung der
Mathematisch-Naturwissenschaftlichen Fakultät der Rheinischen
Friedrich-Wilhelms-Universität Bonn

Neue ergänzte Ausgabe 2014

1. Gutachter: Prof. Dr. Kai-Thomas Brinkmann
2. Gutachter: Prof. Dr. Ulrike Thoma
Tag der Promotion: 17.07.2013
Erscheinungsjahr: 2013

Abstract

The $\overline{\mathsf{P}}$ANDA experiment will be built at the upcoming FAIR facility at GSI in Darmstadt, featuring antiproton-proton reactions hadron physics in a medium energy range. Charm physics will play an important role and therefore secondary decays relatively close to the interaction zone as well. The MVD will be the detector closest to these and will provide high-quality vertex position measurements. Alongside the detector layout and hardware development a detailed detector simulation and reconstruction software is required. This work contains the detailed description and the performance studies of the software developed for the MVD. Furthermore, vertexing tools are introduced and their performance is studied for the MVD.

Disclaimer

Parts of this work have been published in the simulations chapter of the Technical Design Report for the MVD [1]. Because the MVD is a collaborative project some studies have been performed or assisted by other members. Whenever this was the case the TDR is referred to.

Contents

Chapter 1

Introduction

In todays physics, computer simulations have taken an indispensable role. Benefiting from the steep rise of available and affordable computing power, in all branches of physics simulations are performed. Theoretical predictions and the production of simulated observables are compared with with experimental data. The complexity of such simulations varies strongly, reaching from small tools, such as the calculation of the Poissonian distribution of nuclear decays, over particle billiards, wave package propagation in arbitrary potentials, galaxy modeling or the description of atomic orbital bindings in complex substances.

In high energy physics these possibilities developed the custom to simulate whole experimental setups, including everything from the particle reactions, the geometry description, detection performance and reconstruction. Experimental results can be properly corrected for any detector related effects (acceptance, resolution, systematics) and theoretical approaches can be compared coherently. Furthermore the simulation of detector components assists the designing process and the reconstruction strategy development.

Usually the available computing power is the limiting factor to the amount of detail being reasonable to implement in simulations. The advance of computing technology in the last two decades was mainly driven by higher clock frequencies in each generation of CPU's, matching Moore's law [2]. This development slows down in these years because technical limits become harder to overcome. Therefore the number of CPU's in standard computers was increased, gaining computing speed by working in a parallel manner. In particle physics that structure of processing is well established as data can be divided into pieces (usually reaction events) to be processed concurrently. Local computing farms as well as distributed grid computing are the working horses in that field. With the increased accessibility to other performant hardware in standard computers, such as the graphics processors and the vector banks on CPU's, the next step in terms of performance is being taken nowadays.

1.1 Overview

This work is placed in the field of hadron physics and the associated detector physics and simulations. It is focussed on the simulations of and with the MVD, a track-

ing detector for the $\overline{\text{P}}$ANDA [3] apparatus. It is of great importance to understand the tools and frameworks being used in a large scale experiment and collaboration such as $\overline{\text{P}}$ANDA. In this introductory chapter the physics background of $\overline{\text{P}}$ANDA, the experiment layout, the MVD and the PandaRoot software framework are presented. Chapter 2 and 3 deal in detail with the simulation software designed for the MVD and the vertexing tools developed in the scope of this work. Results of performance studies and data comparisons are presented in chapter 4.

1.2 Physics Questions

The $\overline{\text{P}}$ANDA experiment will cover a broad physics program (see [4] for further information) focussed on the strong interaction. Quantum Chromo Dynamics (QCD) is the usual theoretical approach to the strong force. Due to the self-interacting gluons the coupling strength α_s depends on the energy and different means of solving have to be applied in the different energy regimes. In the high energy range QCD can be approached with perturbation theory with great success as α_s becomes very small. Lower energies lead to a steep rise in the strong coupling, causing the quark confinement, and other methods have to be applied. Calculations and predictions are performed e.g. with lattice QCD, effective field theory or potential model calculations. However, the experimental knowledge in this field is still limited and new measurements are necessary to improve the insight about hadron structure.

Choice of Probe Antiprotons are the probe particles in $\overline{\text{P}}$ANDA interacting with hydrogen or a nuclear target. The main reason of that choice is to be free in the quantum numbers of the initial state and the expectedly high formation cross sections. At the common positron-electron colliders the initial state for hadron production has the quantum numbers of a photon (the virtual photon from the annihilation, $J^{PC} = 1^{--}$) which limits the number of produceable heavy neutral resonances (e.g. J/ψ but not η_c). Complete and partial annihilation as well as rearrangement graphs and diffractive production are accessible with antiprotons, serving the broad scientific program of $\overline{\text{P}}$ANDA .

With its dedicated accelerator ring HESR [5] $\overline{\text{P}}$ANDA can measure resonances by performing an energy scan with the beam. The achievable resolution will surpass the beam momentum and reconstruction resolutions, as shown in figure 1.1, and will give access to the resonance widths in addition to its masses. With antiproton beam momenta ranging from 1.5 GeV/c to 15 GeV/c, which corresponds to center-of-mass energies of 2.3 GeV to 5.5 GeV in the $\overline{p}p$ system, it is situated in a medium energy regime. As shown in figure 1.2 thresholds for open charm mesons, charmonia and charmed baryons are accessible as well as many predicted exotic states.

Open Charm Spectroscopy $\overline{\text{P}}$ANDA will contribute greatly to the experimental knowledge of open charm carrying mesons (in general D mesons) as well as charmed baryons (Λ_c, Σ_c, Ξ_c, etc.). Mesons carrying one charmed and one lighter quark, can be seen similarly to the hydrogen atom. The heavy charm quark is the fixed center and the light quark populating the energy levels in the potential expressed in the various

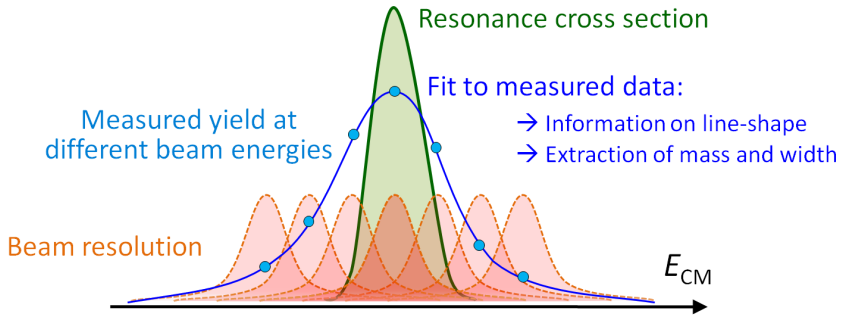

Figure 1.1: Scheme of a beam scan across a particle resonance which is extracted with a better resolution than beam quality and reconstruction uncertainties would allow in a single measurement (see [4], figure from [6]).

D meson states. Figure 1.3 shows prediction and measurement for D and D_s mesons. It is visible that the predictions hold to some extent for the ground states and angular excitations, however higher excitations have not been seen, yet.

Open charm hadrons decay only weakly, therefore these particles have a comparably long lifetime and flight path. With good vertex measurement it is possible to separate these particles from background reactions which typically originate in the interaction point.

Charmonium Spectroscopy Neutral mesons comprise in the view of the constituent quark model solely one quark-antiquark pair and one gluon. In the sector of the three lightest quarks the mass eigenstates are usually described by SU(3) group theory from the $|q\bar{q}'\rangle$ states. The constituents q and q' can have different flavors and their mass difference is often neglected. However the mass eigenstates differ slightly from this pure SU(3) description. For example, in the case of the ϕ meson, which is to be the $|s\bar{s}\rangle$ state by SU(3), a small contribution of $|u\bar{u}\rangle$ and $|d\bar{d}\rangle$ is mixed to the content. The same idea would apply for the extension by the charm quarks to SU(4), however the mass of the charm quarks is so large, that the mixing is neglected for $|c\bar{c}\rangle$ systems. Here the situation is similar to positronium (hence the name charmonium), allowing to study the binding forces through the excitation spectrum both below and above the open charm threshold. Figure 1.4 shows prediction and measured data for the charmonium states. Below the $D\overline{D}$ threshold the states are well established and match the prediction. Above the $D\overline{D}$ threshold only four states are established and many states, labelled with X, Y and Z, require further measurement to deduce their properties and place in the spectrum. Depending on the measurement outcome the theoretical description of charmonium has to be reiterated.

Search for Gluonic Excitations and Exotic States When describing hadrons with valence quarks there is a priori no restriction how many quarks, antiquarks and gluons are combined, except for the color has to combine to white. The two basic combinations of quarks are mesons, a $(q\bar{q})$ pair bound by a gluon, and bosons, three

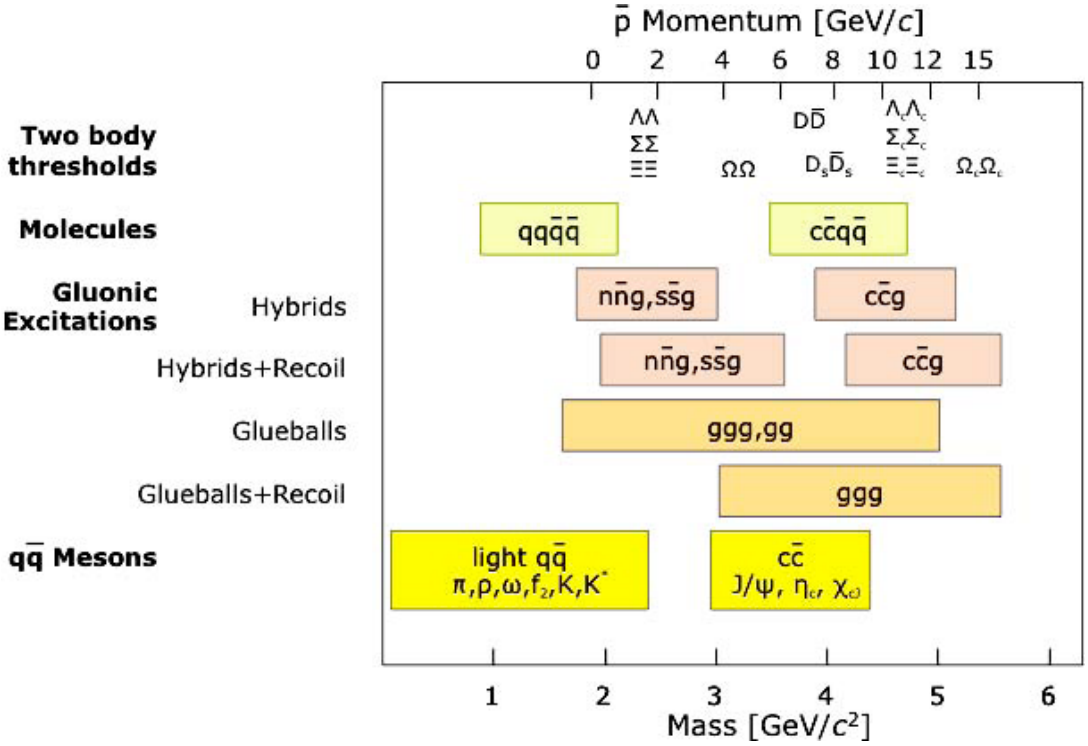

Figure 1.2: Available hadron mass range in $\overline{\text{P}}$ANDA and the associated required antiproton beam momentum on the upper scale [7]. The energy regions of exotic state predictions are shown as well.

quarks (qqq) bound by three gluons. Going further, an additional quark-antiquark pair could be present forming a tetraquark ($qq\bar{q}\bar{q}$), a pentaquark object ($qqqq\bar{q}$) or molecular structures of two mesons $(q\bar{q})(q\bar{q})$ or of one meson and a baryon $(qqq)(q\bar{q})$. Additional gluons may excite a particle state to a hybrid ($q\bar{q}g$) and there is even the possibility to create color neutral objects without any quarks, called glueballs (ggg). In the usual quark model, one finds that not all quantum numbers are allowed, e.g., for mesons the combinations J^{PC} of 0^{--}, 0^{+-}, 1^{-+}, 2^{+-}, etc., are forbidden. This is one region to look for exotic states, which are allowed to yield these numbers. Exotic states with allowed quantum numbers will mix with the non-exotic particles, which makes their identification much more complicated.

$\overline{\text{P}}$ANDA envisages to measure in places of interest with high precision to identify or falsify the existence of these exotic states and, if seen, to determine their nature.

Other Topics In most hadron physics experiments all particles are produced and measured in vacuum. How hadrons behave in the vicinity of nuclear matter is a question only partly answered. Some experiments tackled this questions and found mass and width modifications of, e.g. the ϕ mesons by examining its decay into two leptons [8]. $\overline{\text{P}}$ANDA will contribute to that field of research in the charm sector by using a heavy nuclear target, such as xenon or gold, instead of hydrogen.

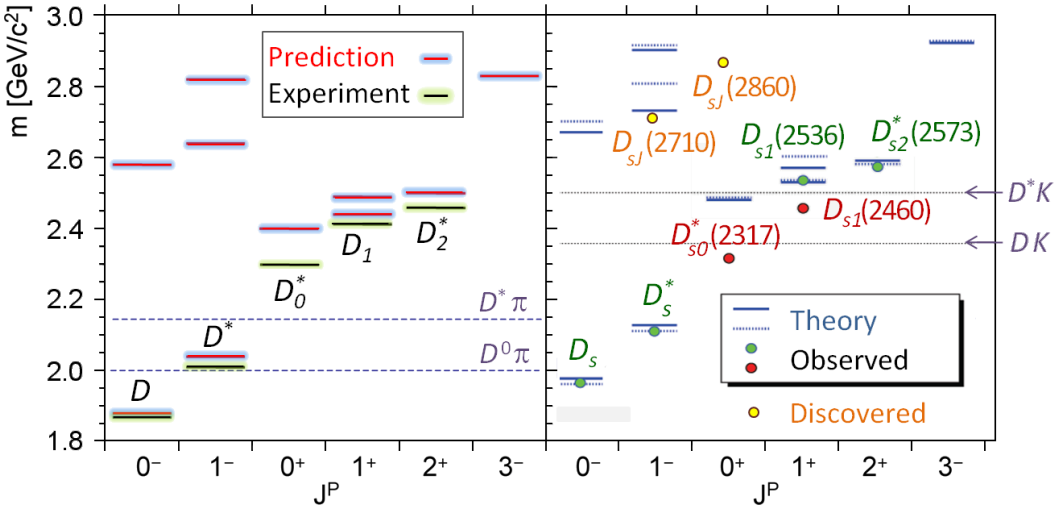

Figure 1.3: Predicted and measured states of D and D_s mesons (figure from [6]).

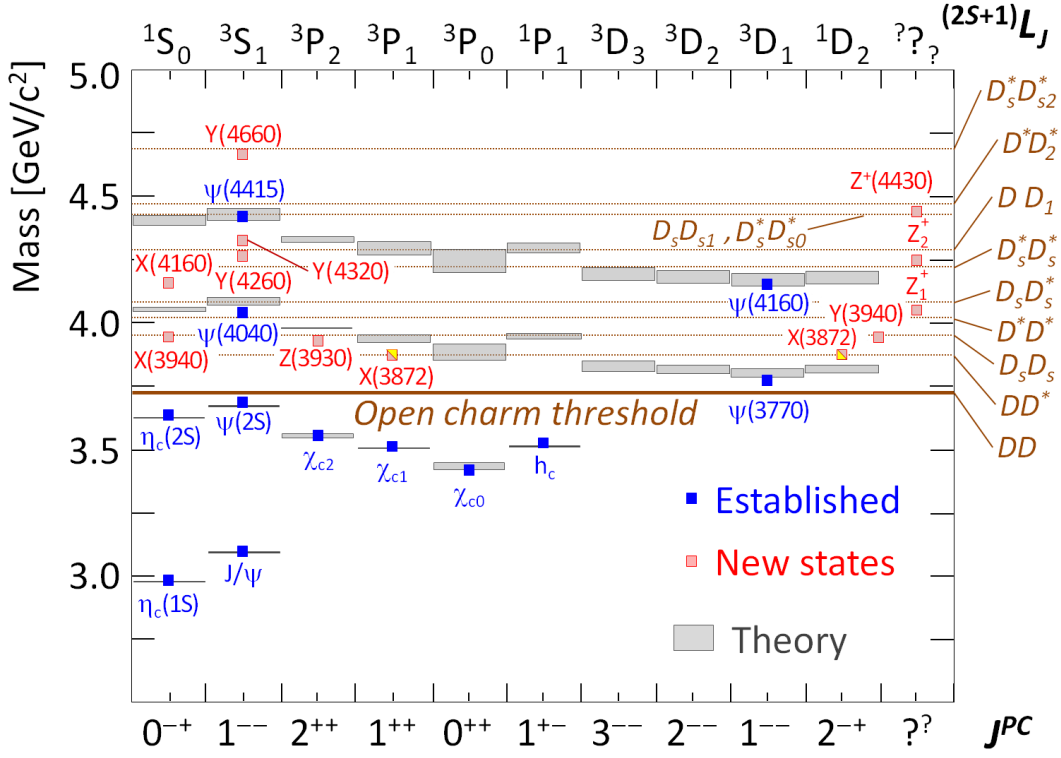

Figure 1.4: Predicted and measured charmonium states. Above the $D\overline{D}$ threshold both theory and experiment require improvement (figure from [6]).

Furthermore the annihilations can be studied in electroweak channels, e.g. Drell-Yan processes, with very high statistics. This enables the measurement of the electromagnetic form factor and parton distributions.

In antiproton-nucleon reactions strangeness carrying baryons (Λ, Ξ, etc.) are produced. Using a secondary target to stop and capture these in nuclei their behavior bound in a nucleus will give new insight about the forces inside nuclei. This is done by a dedicated experiment extension which will allow to measure the capturing vertex as well as the relaxation photons.

1.3 The $\overline{\text{P}}$ANDA Experimental Setup

The accelerator facility at GSI[1] is going to be greatly extended by the FAIR project [9]. One of the major experiments, the $\overline{\text{P}}$ANDA detector (Anti*p*roton *An*nihilation at *Da*rmstadt, see [3]), will be built to measure antiproton-proton and antiproton-nucleus reactions at medium energies. $\overline{\text{P}}$ANDA is as fixed-target experiment, thus the distribution of the reaction products covers the complete polar angle range with a strong enhancement in forward directions (see figure 1.5). This anisotropy increases with higher beam momentum. Typical momenta for the reaction products are 100 MeV/c to 1 GeV/c.

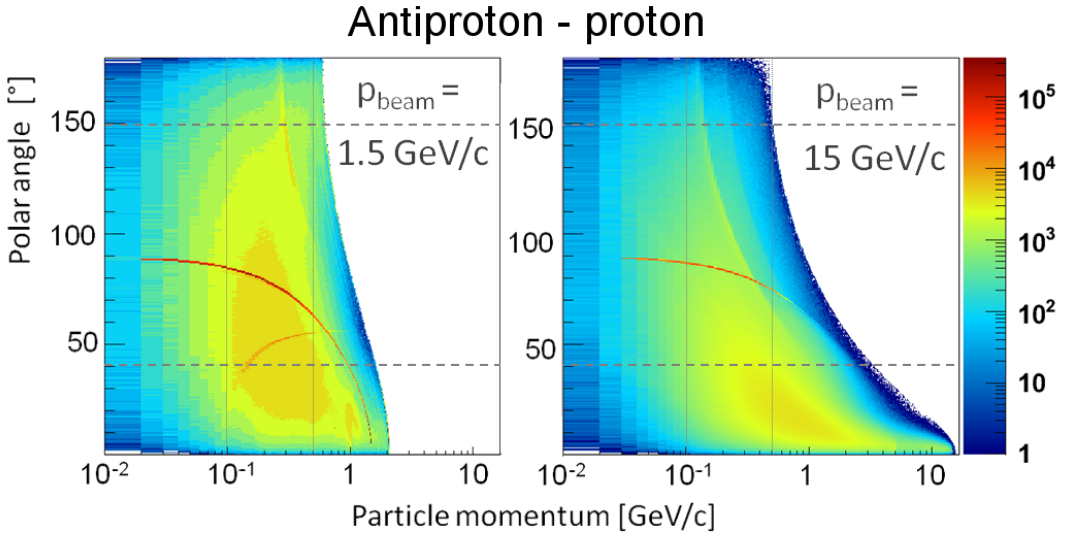

Figure 1.5: Expected particle distribution in polar angle and momentum for antiproton-proton reactions at 1.5 GeV/c (left-hand side) and 15 GeV/c (right-hand side) of beam momentum produced with the DPM event generator. The dashed lines indicate the angular coverage of the MVD barrel part. The high yield curves starting at 90° come from the recoil protons of elastic scattering.

$\overline{\text{P}}$ANDA as a fixed target experiment consists of two spectrometers, the Target Spectrometer surrounding the interaction region, followed by the Forward Spectrometer further downstream. Figures 1.6 and 1.7 give an overview of the detector components

[1] Gesellschaft für Schwerionenforschung, Darmstadt, Germany

in both spectrometer parts. The detector is a composite of many sensitive subsystems serving the measurement with track information, calorimetry and PID. There are three basic shapes in the subsystems: Barrel-shaped components at high polar angles ($\theta \approx 22^\circ \ldots 150^\circ$) disk-shaped parts as caps to these barrels ($\theta \approx 5^\circ \ldots 22^\circ$) and the Forward Spectrometer as a sequence of walls ($\theta < 10^\circ$). The components are introduced by their function in the sections below.

A superconducting solenoid magnet generates a 2 T strong field along the z-axis. In the forward spectrometer a 2 Tm strong dipole is present which is also part of the accelerator ring and will be ramped accordingly. An illustration of the field strength distribution simulations in the barrel part is given in figure 1.8.

1.3.1 Beam and Target

Every fixed target experiment has to solve how beam and target are brought together in its special way. In $\overline{\text{P}}$ANDA the concept is to let hydrogen, in the form of frozen pellets, fall at 60 m/s through the focussed beam with a rate of 100 kHz. With optical tracking above the detector volume and vertex reconstruction of high-statistic events the position of individual $25 \ldots 40$ µm large pellets will be known with a very good precision despite the large position spread of 1 mm. Heavy nuclear targets are under development and will probably be heavy gases or thin wires.

The accelerator ring for cooled antiproton beams, called HESR[2] ([11, 12, 5]), will provide brilliant antiproton beams between 1.5 GeV/c and 15 GeV/c. Stochastic and electron cooling will reduce the momentum spread to $\Delta p/p \approx 10^{-5}$ in the high resolution mode. The mean design interaction rate in the high luminosity mode is 2×10^7 annihilations per second. Both the falling pellets and the extraction gap in the beam will produce an alternating pattern of luminosity putting high demands on the readout and data acquisition electronics. The accelerator will be able to perform precise energy scans over an interesting mass region.

1.3.2 Charged Particle Tracking

The expected multiplicities of charged particles in each event are well below 20, thus the reactions give relatively clean events, compared to experiments with higher energies or heavier targets. To cover all the different regions of the experiment with tracking modules efficiently, four detector systems are foreseen. Innermost there is the Micro Vertex Detector (MVD), giving high precision 3D hit information close to the interaction point in a wide polar angle range ($3^\circ < \theta < 150^\circ$). This is followed by the central tracker, a Straw Tube Tracker (STT [13]), covering angles of 10° to 140° measuring particle track curvatures precisely. The more forward region in the barrel spectrometer part will be covered by Gas Electron Multiplier (GEM) disk stations, which provide 3D hit points. Planar straw tube stations will measure particle curvatures in the forward spectrometer. Two stations each are positioned before, inside and after the dipole magnet.

[2]High Energy Storage Ring

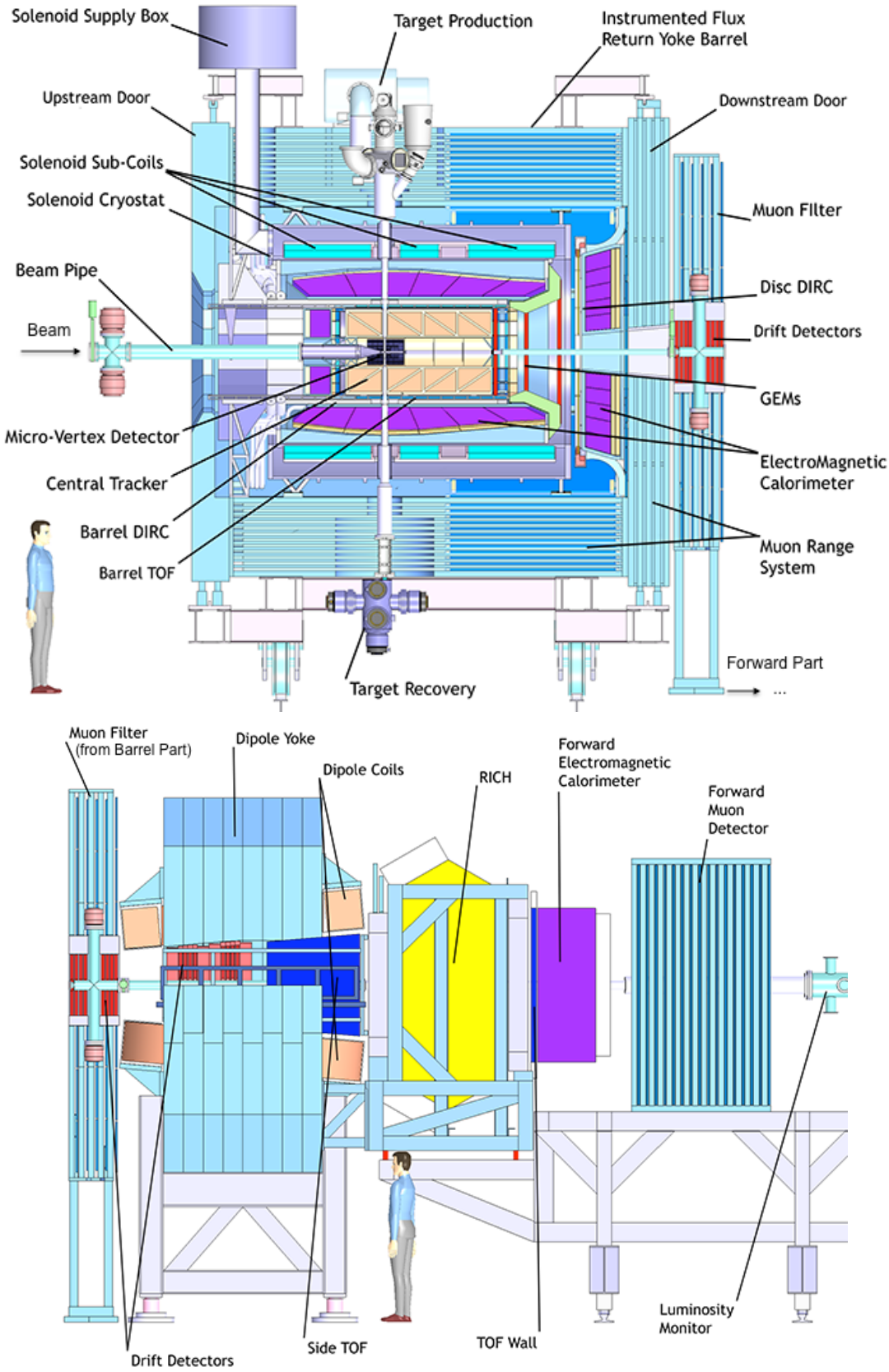

Figure 1.6: Side view of the $\overline{\text{P}}$ANDA detector. The Target Spectrometer is shown in the upper and the Forward Spectrometer, continued at the muon filter, in the lower image.

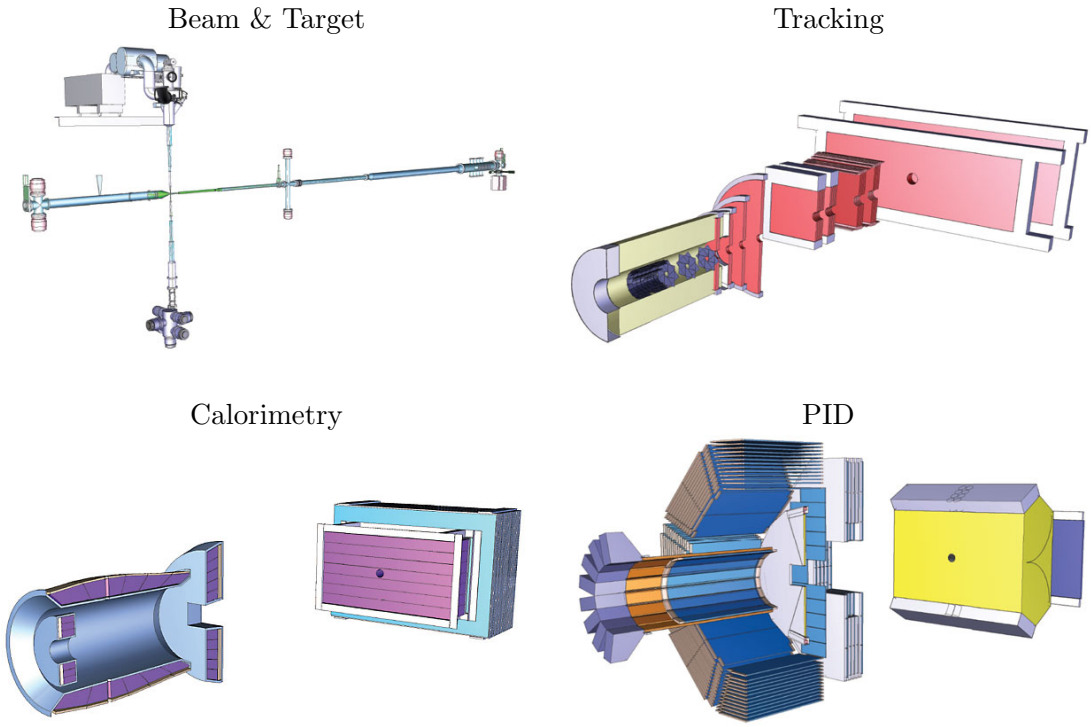

Figure 1.7: CAD images for the functional systems of $\overline{\text{P}}$ANDA which are beam and target, tracking, calorimetry as well as particle identification.

1.3.3 Particle Identification System

Trajectory measurement alone does not yield all properties of a particle as one last component of the four-momentum still has to be determined. This can be achieved by measuring the energy, time of flight, velocity or the energy loss ($\mathrm{d}E/\mathrm{d}x$). In $\overline{\text{P}}$ANDA there are several particle identification (PID) systems, covering the barrel and forward region.

To measure the velocities of low momentum charged particles, several time of flight (TOF) detectors made of fast acting scintillators are foreseen. These give the stop signal for the time measurement, while the MVD will provide the start time. Charged particles traveling with high momentum, instead, are identified with velocity measurements from the Cherenkov detectors. In the barrel spectrometer that is accomplished with DIRC[3] detectors while in the forward spectrometer it is a RICH[4] detector. Because the Cherenkov detectors are good at separating protons and kaons from each other and from pions and muons, but the latter two overlap strongly, a muon identification is added as well. It comprises gaseous detector planes inside the iron flux return yoke of the magnet which in turn acts as strong absorber material. Muons are then identified by their low interaction with the absorber, compared to the pions which should be stopped in the first layers. In the forward spectrometer this sandwich structure is introduced as the last wall of detector elements.

[3]Detection of Internally Reflected Cherenkov radiation
[4]Ring Imaging Cherenkov Detector

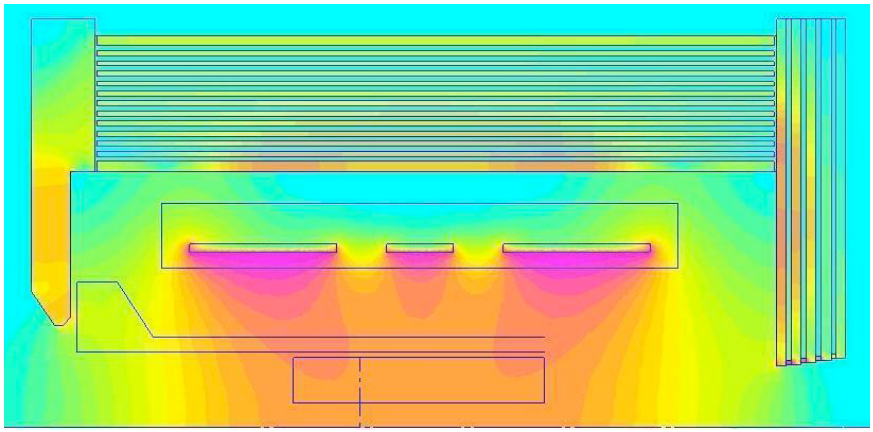

Figure 1.8: Magnetic field strength distribution in the barrel spectrometer [10] (profile shown starts at the beam axis). In the region of the central tracker, indicated by the box at the bottom of the picture, the field strength is almost constant at the design value of 2 T.

1.3.4 Electromagnetic Calorimetry

Photons and charged particles which leave the central tracker and the Cherenkov detector volumes reach the Electromagnetic Calorimeter (EMC). Electromagnetic showers are created in a huge array of fast scintillating crystals ($\Delta t < 20\,\mathrm{ns}$) with a high radiation length X_0 and the total energy deposit is measured through the scintillating light, thus measuring the kinetic energy of the particle. Each one of the 15552 crystals is made of $PbWO_4$ and has a size of about $2 \times 2 \times 20\,\mathrm{cm}^3$. The smaller front planes are facing towards the interaction region, while the slightly larger back side is connected to the avalanche photo diode (APD) readout. Barrel part, barrel end caps as well as the calorimeter wall in the forward spectrometer cover about 96% of the 4π solid angle and an energy resolution of $1.54\%/\sqrt{E/[\,\mathrm{GeV}]} + 0.3\%$ is expected.

It is foreseen to identify neutral pions, decaying into two photons in their rest frame back-to-back, directly by combination of appropriate photon candidates. Furthermore, the signal shape and the shape of the shower spreading over several crystals gives important information on the particle species thus contributing to the global particle identification.

1.3.5 Luminosity Monitor

Elastically scattered antiprotons have a well-known cross-section and angular distribution. Their counterparts, the slow protons are stopped in the beam pipe as long as they have a momentum of less than $100\,\mathrm{MeV}/c$. Silicon strip detector stations are foreseen as Luminosity Monitor [14] at a long distance ($z \approx +12\,\mathrm{m}$) from the interaction region to measure these antiprotons. They cover very shallow polar angles (from 3 to 8 mrad). Due to the symmetry of elastic scattering only a small portion of the azimuth range needs to be covered.

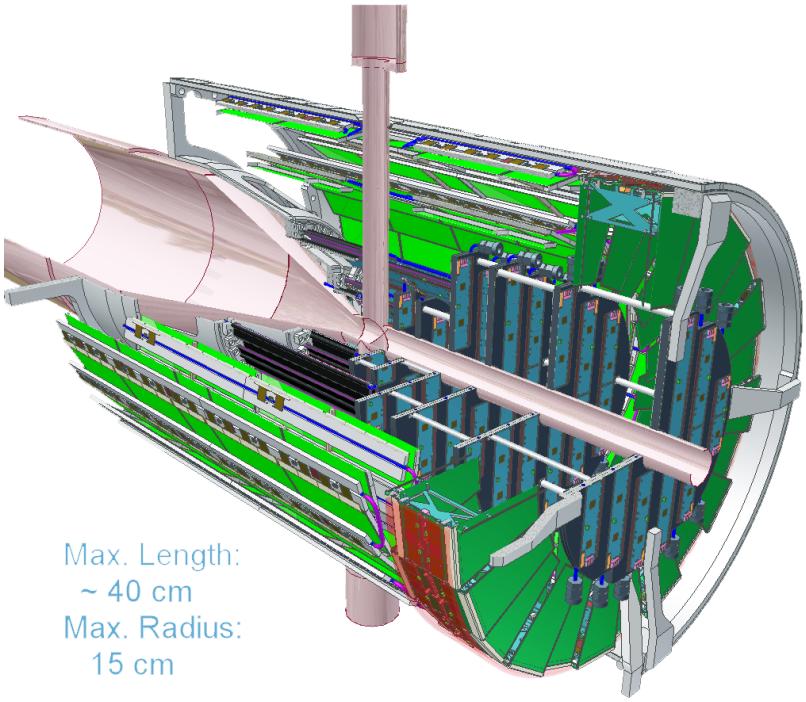

Figure 1.9: View of the full MVD CAD drawing. One quarter is removed to give a view inside. The beam comes focussed from the left cone and the target falls from the top through the target pipe. The silicon sensors are colored green (strips) and teal (pixels with flip-chip electronics).

1.3.6 Hypernuclear Experiment Extension

In a later phase of operation $\overline{\text{P}}$ANDA will run in a modified setting to measure decays of hyperons embedded in nuclei [15]. Hyperon pairs that are produced in a primary target travel through a stack made of secondary target material and silicon strip detectors. An array of scintillators in the back and the EMC measure photons from hyperon de-excitations inside the nuclei. The presence of a hyperon is then identified by its trajectory through a part of the strip detectors, the stopping inside the secondary material and the photons. The behavior of strange baryons close to nuclear matter can be studied, for example mass and width modifications as well as transitions between bound states.

1.4 The Micro Vertex Detector

The innermost sensitive detector component of the $\overline{\text{P}}$ANDA experiment is the Micro Vertex Detector (MVD). It provides charged particle track point measurements with very high precision in space and time as well as energy loss measurement. The main goal is to measure the first track point of a charged particle as close to the interaction point as possible, which is essential for the reconstruction of decay vertices. Figure 1.9 gives an impression how the MVD is shaped and fits around the beam-taget pipe cross.

1.4.1 Detector Layout

Planar silicon sensors are the sensitive components of the MVD arranged in a multi-barrel-shaped part along and disks perpendicular to the beam axis (see figures 1.10 and 1.11). Due to the fixed target most particles will travel under shallow polar angles. Six disks made of pixel sensors will measure these tracks close to the beam line starting from $z = 2\,\text{cm}$ after the interaction point to the first widening of the beam line. These sensors have to cope with the highest hit rate in the whole MVD and serve the forward tracking with high resolution close to the interaction point down to $\theta = 3°$ (9° to have at least four hits per track). Two strip sensor rings extend the last two disks outwards, where the particle rate is considerably lower. At about $\theta = 40°$ the disks end and the barrel layers start. Four sensitive layers are in the barrel part ranging up to $\theta = 150°$. The two inner shells are silicon pixel sensors to stand the high rates and give high resolution very close to the interaction point, while the outer two layers are double sided silicon strip sensors to limit the number of signal channels. Optimizing for receiving at least four points per track, small areas of overlap between the sensors are introduced, closing the gaps even for charged particles bending strongly in the magnetic field.

Silicon Sensors

A planar silicon sensor is basically a thin diode (p-n-junction) of 100 to 300 µm thickness with a readout structure on the surface. A reverse bias voltage is applied, so mobile charge carriers are drawn from the p-n-junction, creating a zone of depletion. The silicon sensors will be operated in full depletion mode, such that this depletion zone is spread over practically the whole sensor thickness.

Figure 1.12 shows how a pixel sensor and a double sided strip sensor are structured. The sensors are made of n-doped silicon as bulk material with highly n-doped (n^+) and p-doped (p^+) inlays at the surface. Two modes of readout are possible, one with the metallic conductor touching the inlays (DC-coupling) and being insulated from the bulk material with a layer of SiO_2 and the other with the insulating layer covering the whole surface and the metallic conductors are on top of it, coupling to the structures below capacitively. In table 1.1 the basic parameters of the MVD sensors are summarized.

Charged particles crossing the sensor will ionize the silicon along their path, on average one electron-hole-pair being created per 3.6 eV of deposited energy (energy band gap in silicon is about 1.1 eV, the rest goes to lattice vibrations [17]). Electrons and holes become separated in the electric field of the applied bias voltage and travel to either of the sensor sides. That current is temporarily changing the electric field, which in turn is measured at the readout structures. More figuratively speaking, the charge carriers are collected at the readout connections and the charge is measured. Furthermore, the electrons and holes scatter elastically on the silicon atoms and thus the charge carriers disperse into a cloud. In a magnetic field the charge carriers are also moving under the Lorentz force leading to deviations from the electric field's path, depending on the sensor orientation inside the magnetic field.

The pixel sensors of the MVD have a two-dimensional metallization structure

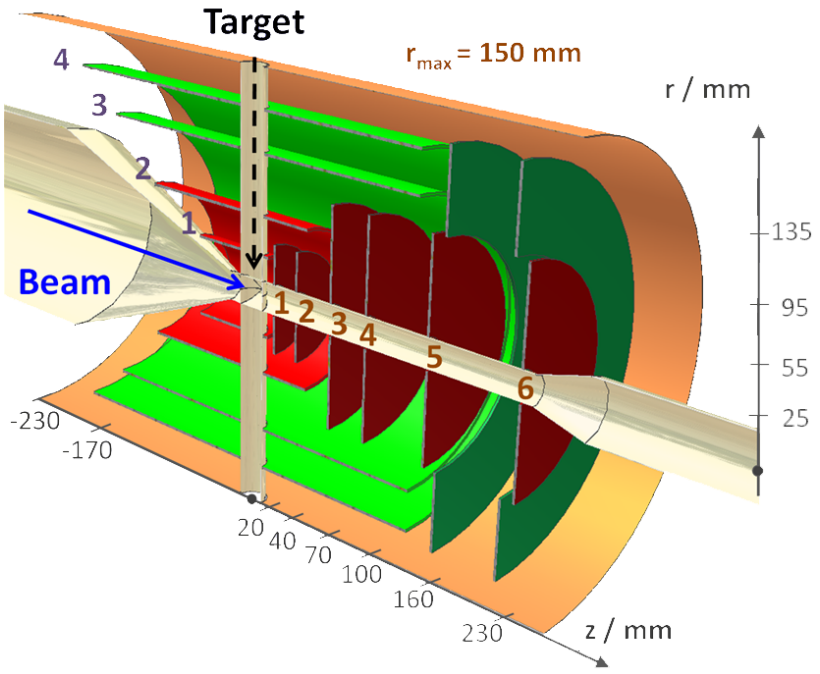

Figure 1.10: Schematic view of the MVD layer structure: Six pixel disks at 2, 4, 7, and 10 cm, and two pixel/strip disks at 16 and 23 cm. Two pixel barrels at 2.5 and 5.5 cm, and two strip barrels at 9.5 and 13.5 cm (figure from [1]).

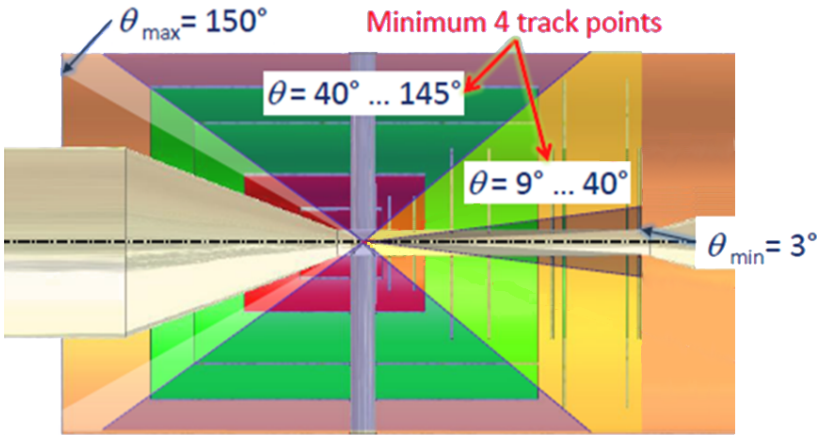

Figure 1.11: Schematic view of the MVD layout structure: Polar angle coverage. In a range of $9° < \theta < 145°$ tracks leave at least four hits in the MVD. Down to 3° and up to 150° the MVD contributes with less hits per track (figure from [1]).

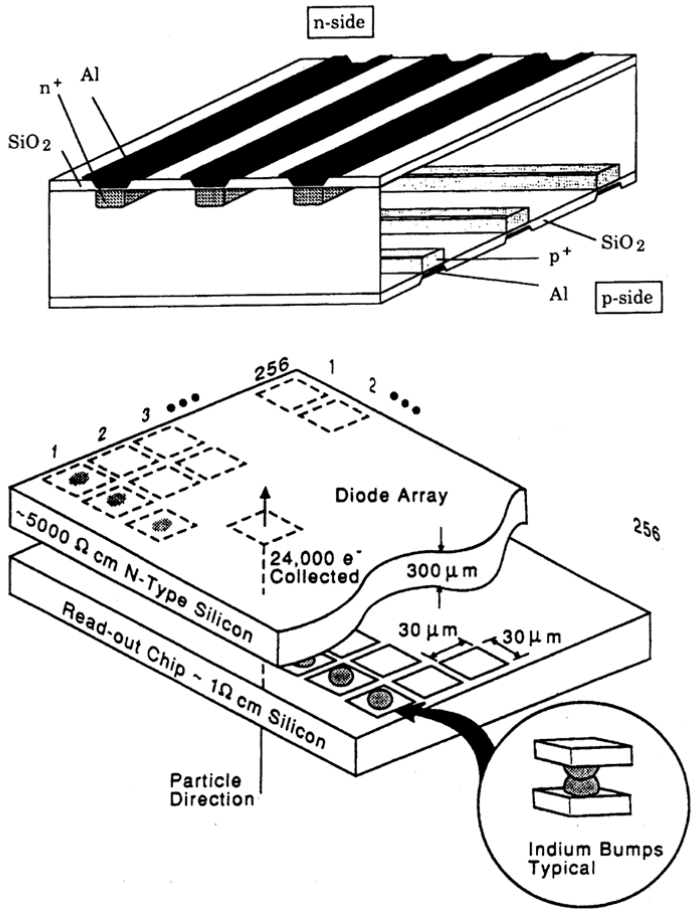

Figure 1.12: Schematic drawings of a double sided silicon strip detector (upper image) and a silicon pixel detector with the readout chip on top (lower image) (figures from [16]).

shaped as a grid of squares, $100 \times 100\,\mu m^2$ in size (see figure 1.13 and figure 1.15). Double sided strip sensors have linear readout structures. Top and bottom side differ in the orientation of the strips, offering the reconstruction of a two-dimensional hit while the number of readout channels is reduced drastically in comparison to the pixels. In the MVD there will be two different double sided strip sensor types (cf. figure 1.14 and figure 1.15), rectangular ones with a stereo angle between the top and bottom side of 90° for the barrel part and trapezoidal sensors with a stereo angle of 15° in the disk part. Production possibilities and stiffness studies will determine what final thicknesses can be achieved safely for each of the sensors. Table 1.1 summarizes the key specifications for the MVD sensors.

Readout Electronics

The phrase "readout electronics" encompasses several different functionalities and hardware pieces in the electronics chain of gathering the data from the sensors. First, the front-end chip, directly attached to the sensor, amplifies, integrates, discriminates

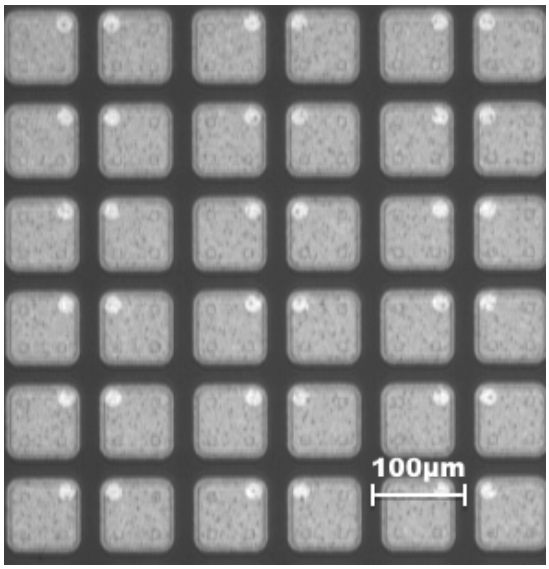

Figure 1.13: Photograph of a prototype pixel matrix for the MVD. The white circles are the connectors for the bump bonds to the front-end chip.

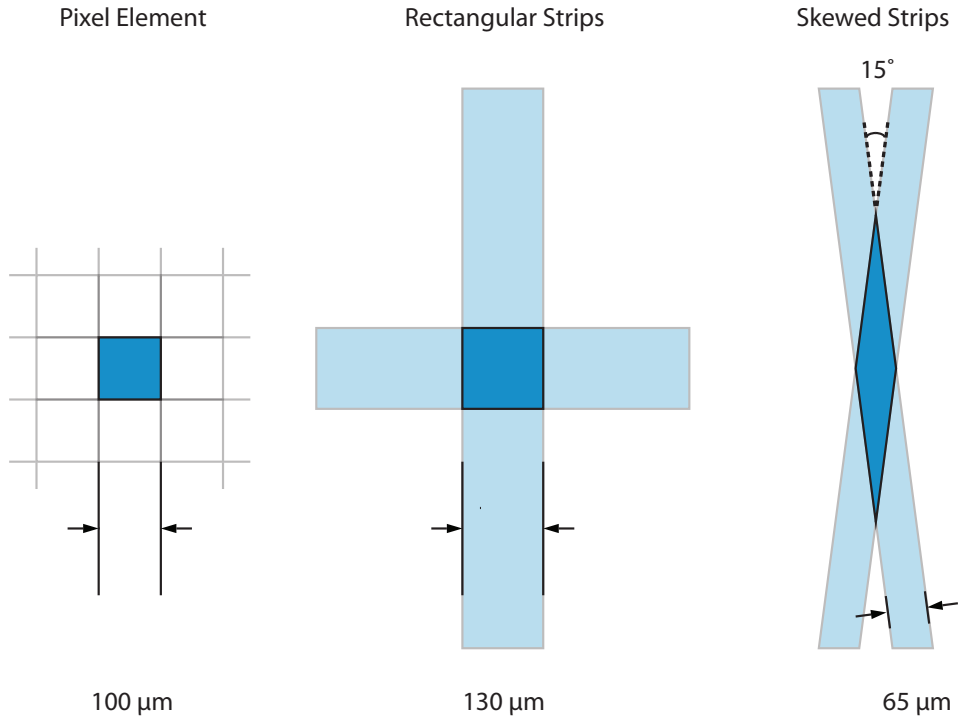

Figure 1.14: Schematic view of the MVD readout cells on the sensor plane. From left to right: Pixel cell, rectangular and by 15° skewed double sided strips (one on the top side, the other on the bottom, the overlapping area is marked in dark blue).

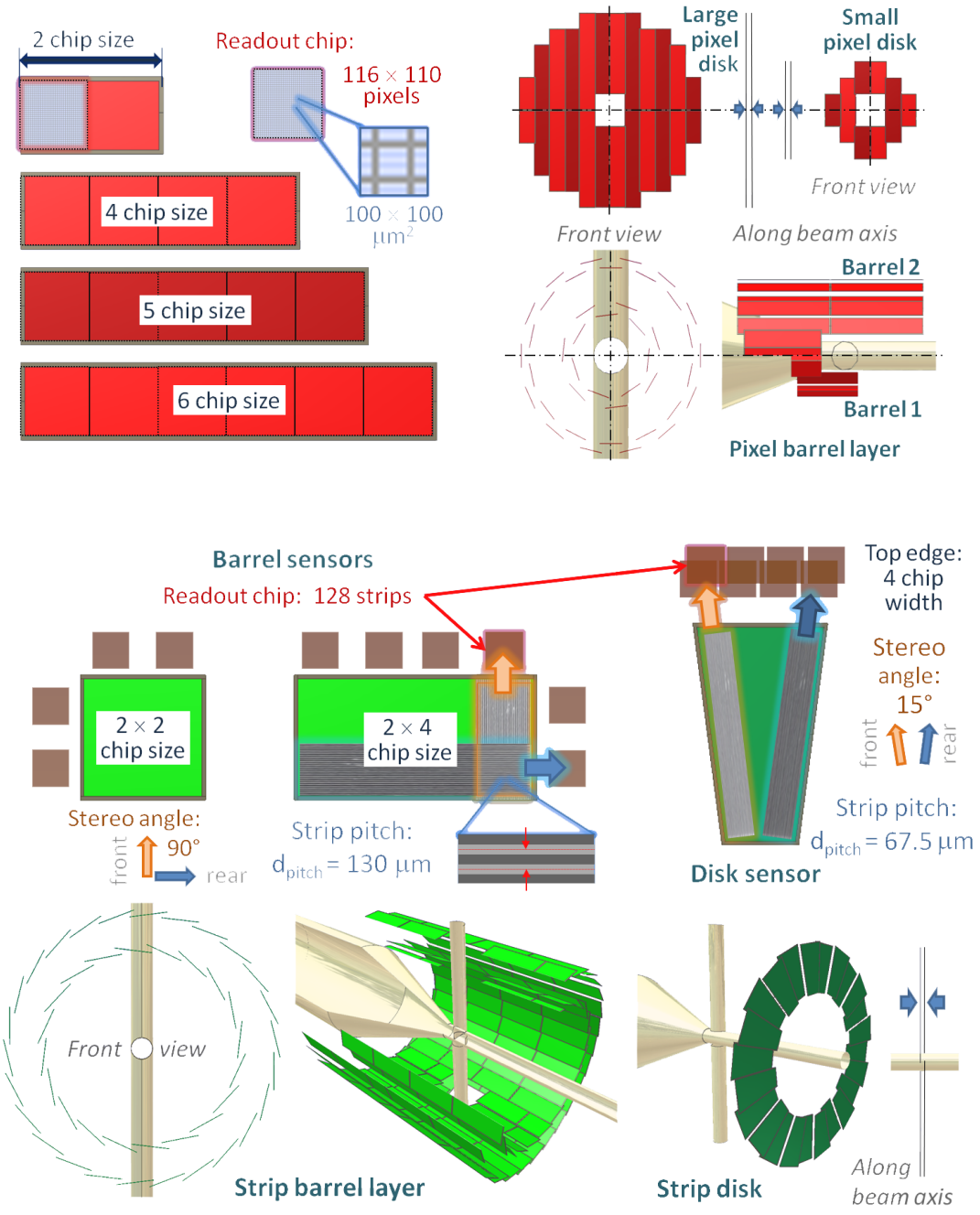

Figure 1.15: Detailed layout how pixel (top) and strip (bottom) sensors are arranged and read out (figures from [6]).

	Pixel Sensors	Rectangular Strip Sensors	Trapezoidal Strip Sensors
Feature Size	100 µm × 100 µm	130 µm	65 µm
Stereo Angle (skew)	–	90°	15°
Sensor Thickness	100 . . . 150 µm	200 . . . 300 µm	200 . . . 300 µm
Eelectronic Noise (ENC)	200 e^-	1000 e^-	1000 e^-

Table 1.1: Sensor types planned for the MVD. Innermost are pixel barrels and disks, rectangular strip sensors in the outer barrels and trapezoidal strip sensors at the outer disks.

and digitizes the signals. Controller chips gather data from several front-ends and transmit them out of the MVD volume of measurement by radiation-hard optical links [1]. That concentrated data will be processed further on hardware implemented algorithms to compress the stream of data until it is sent to the common Data Acquisition (DAQ) system of $\overline{\text{P}}$ANDA.

Most important to the MVD are the functionalities of the front-end chips as these translate the signal into a digital data stream. Basically the current at each channel of the front-end is pre-amplified and charges a capacitor. With a constant current source this capacitor is drained, which produces a signal voltage with a steep rising edge and a more flat trailing edge. A discriminating threshold voltage is applied, to suppress most of the noise created in the sensor-preamplifier combination. The time of crossing the threshold at the rising edge gives the time stamp of the signal (measured with the globally available clock), while the duration of the signal above the threshold gives a measure for the total charge content (Time Over Threshold Methond) and thus a measure for the particle's energy loss in the sensitive volume.

In the case of the pixel sensors the front-end chip (ToPix [1]) is fixed back-to-back on the sensor. Bump bonds, small indium or soldering lead balls, connect the metallic pads of the sensor with the readout pads of the front-end. In contrast to that, wire bonds connect the strip sensors at the sides to the front-end chip via a pitch adapter, a specific foil or plate with metallic connection lines matching the connector distances at each side.

1.4.2 PID with the MVD

Charged particle energy loss from ionization is measured by the charge seen at the amplifiers. The energy loss distribution depends on the particle momentum, the track length inside the sensitive material and the particle species. Usually the Bethe-Bloch formula is used to describe the mean of the distribution varying with the particle momentum. Different particle types can be distinguished at low momenta by their differing mean energy loss (see figure 1.16). At higher momenta the distributions merge into one band starting with the lowest mass, where the distinction is less powerful or even not possible. As show in the inserts I-IV in figure 1.16 at each momentum the energy loss is distributed with a Landau distribution around its mean value from the Bethe-Bloch formula. The distributions from the various particle species overlap. Measuring momentum and energy loss enables to derive a likelihood for each particle hypothesis, being very pronounced at one hypothesis at low momenta and equal like-

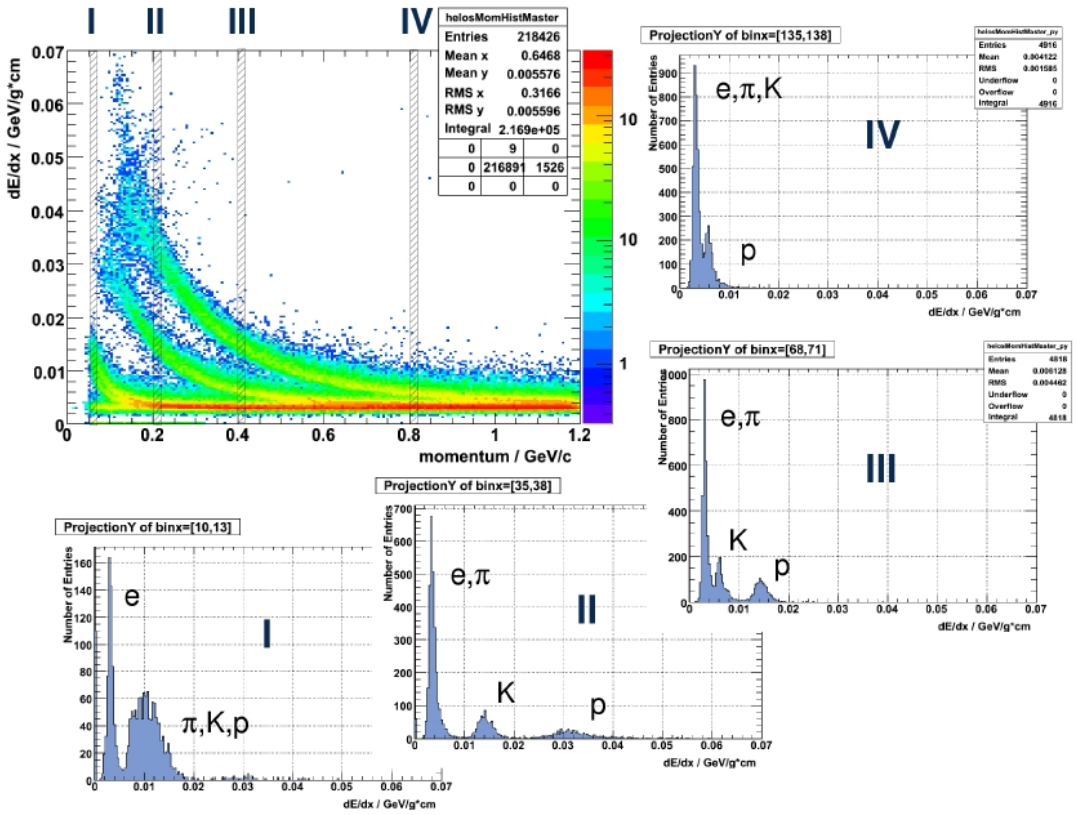

Figure 1.16: Energy loss bands ($\frac{dE}{dx}(p)$) for protons, electrons pions and kaons. With higher momenta (inserts I-IV) the separation of the particle species becomes weaker (figure from [18]).

lihoods at high momenta. These sets of likelihood values for all MVD hits contribute in the particle identification software.

1.4.3 Mechanical Design

For the MVD it is a great challenge to support the sensors, front-end chips, cables and cooling pipes mechanically while fitting into a very restricted space. Furthermore, it is envisaged to introduce as little material load as possible into the particle flight paths, to minimize distortion effects by not measurable ionization, small angle scattering and secondary photon or electron production (which are background in the electromagnetic calorimeter). At the same time the mechanical and thermal stability of the whole system has to be ensured to avoid misalignment effects. Thus the routing of cables and cooling tubes is an issue where much careful engineering is essential.

A hierarchical organization (presented in figure 1.17) is used to manage the mechanical and electronic elements together in a modular way, assuring stiffness and safety during the assembly procedures. In concurrence a volume naming convention, common to the whole system, is introduced which is used by the scientists, engineers, the simulations and in the production. The target pipe crossing the beam pipe

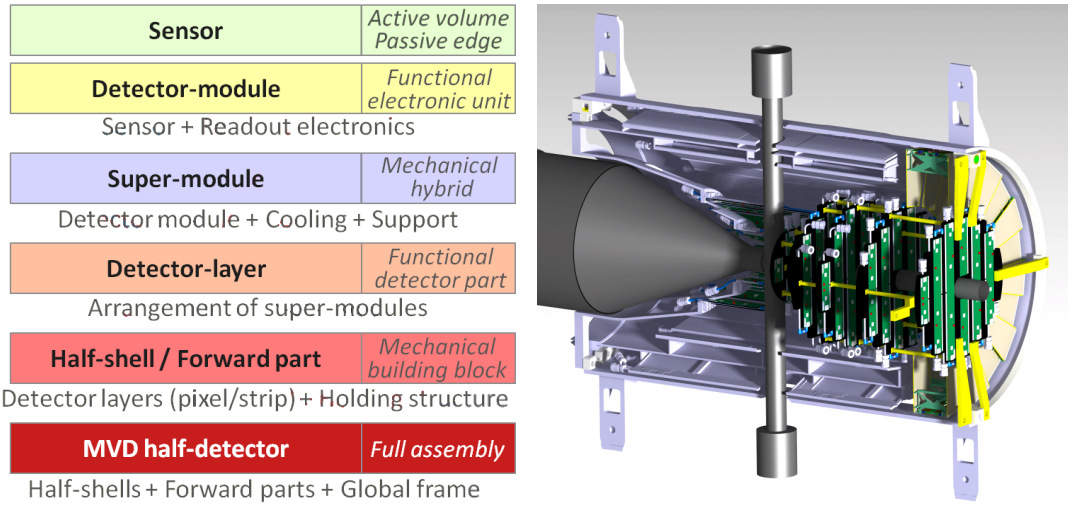

Figure 1.17: Organization hierarchy of the MVD components (left) and a CAD view of the half detector and the second half forward part (right).

defines a plane which breaks the ϕ-symmetry of the detector. Mounting the cross requires a cut in the inner detectors along that plane. Thus the MVD is mechanically divided into two halves which are segmented themselves into the forward half disks assembly and the half barrel. Each layer of one half part is a fully functional detector part, including the routing of the cooling pipes and cables. The smallest mechanical unit, the super modules (in other experiments often called staves), contains several sensors, their readout chips, module controllers as well as support structures and integrated cooling pipes. Carbon fibre, carbon foam and ROHACELL foam are the light-weighted choice of material for the holding structures, introducing as little material with as small density as possible.

1.5 The PandaRoot Software

In the $\overline{\text{P}}$ANDA experiment a very detailed computer simulation software of the detector and its response is being used and further developed. Learning from other High Energy Physics (HEP) experiments that such a detailed simulation is necessary and technically feasible, the software developments and studies are done in parallel with the hardware development even before the experiment is built. Many high-quality software programs are known to the community of particle physics. Aiming at the most benefit from these, efforts have been joined for several experiments at FAIR to develop the FairRoot framework, providing to several experiments all core functionalities for running the simulations as well as third party software tools in form of external packages. One application therein is PandaRoot, the software to simulate the $\overline{\text{P}}$ANDA detector. In the following sections the external packages, FairRoot and PandaRoot will be described.

1.5.1 External Packages

The external packages are the third-party software collection, that is necessary to run FairRoot. They are distributed together at fixed versions, to pertain compatibility. Maintenance and development lies in the responsibility of each package's developers, whereas communication with and contribution from the FairRoot community is not excluded.

ROOT Developed at CERN by the physics community, ROOT [19, 20] provides a huge amount of tools and functionalities, specifically useful for the HEP community. It is the basic package used intensively by FairRoot (hence the framework's name). The major functionalities important for the framework are:

- CINT, a macro interpreter with an interactive shell
- A graphical user interface (GUI) to browse Objects, to draw user defined Objects or interact with displayed contents and an Event Display (TEve)
- File management, data I/O, a binary file format
- Generic database access (under construction)
- Parallel processing (PROOF)
- Histograms, graphs, mathematical functions, data point fitting and Matrix algebra tools
- Geometry and material description, management and visualization
- Particle physics relevant preset data formats (e.g. Lorentz vectors)
- Multi variate analysis framework (TMVA)

Virtual Monte Carlo Virtual Monte Carlo (VMC) and Virtual Geometry Model are used to access different Monte-Carlo software packages and their geometry descriptions with one interface. The geometry has to be defined only once and the user selects which package's description and navigation is used. Currently there are GEANT3, GEANT4 and ROOT interfaced (FLUKA support has been discontinued).

GEANT3 & GEANT4 "*The GEANT program describes the passage of elementary particles through the matter. Originally designed for the High Energy Physics experiments, it has today found applications also outside this domain in the areas of medical and biological sciences, radio protection and astronautics. The principal applications of GEANT in High Energy Physics are: The tracking of particles through an experimental setup for simulation of detector response the graphical representation of the setup and of the particle trajectories.*" [21] GEANT3 [21, 22] is written in FORTRAN and its last major version 3.21 dates to 1994. The GEANT4 software [23, 24] was developed from the GEANT3 physics models but completely re-developed in C++ to make use of object oriented programming. Though updates were introduced to

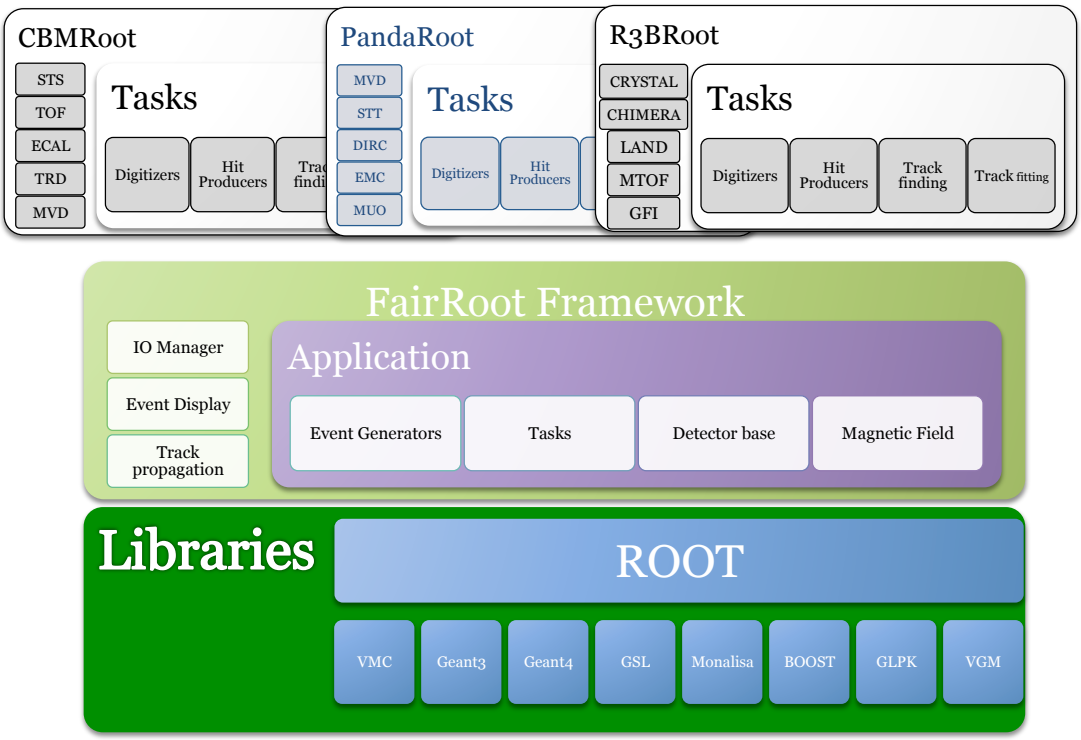

Figure 1.18: Layout scheme of FairSoft [29]. Third-party libraries at the bottom, the framework in the middle and the specific experiment implementations on top of it.

make the physics processes in the transport engine more realistic, the results of both versions are compatible. They are likely the most often used simulation engines in the HEP community.

PYTHIA The library of PYTHIA [25, 26] is a high energy particle generator and decay model. It models collisions of elementary particles, such as electrons, protons, etc. with each other. Physics reaction processes included are, amongst others, hard and soft interactions, parton distributions and parton showers, fragmentation as well as decays.

Pluto The simulation package for hadronic reactions PLUTO [27, 28] is a C++ library for event generation, experimental filters (acceptance, etc.) and particle decays. It is invoked from ROOT interactively where the output can be analyzed directly or passed to GEANT for further processing.

1.5.2 FairRoot Framework

FairRoot is the software framework for the $\overline{\text{P}}$ANDA experiment as well as for CBM, R3B and others. It provides, besides the external packages, a library of C++ classes covering the management of data streams, parameters, as well as the interfacing to the various simulation- and reconstruction-related tools of the external packages. The

schematic structure is shown in figure 1.18. FairRoot manages the communication to the various libraries and is the interface and basis for the experiment implementations.

The framework bases itself mainly on ROOT. Most importantly it makes use of the file format (`.root`), the branch structure (`TBranch`), file chains (`TChain`), data containers (`TClonesArray`, the geometry description and management (`TGeoManager` etc.) and the plug-in structure of so-called tasks (`TTask`). In the design it is foreseen to call everything from the ROOT command line or rather by processing macros in the ROOT C++ interpreter (CINT). All simulation code is compiled into dynamic libraries and `root` is the only executable file. The ROOT macros are used to set up, steer and run the event generation, the Monte-Carlo transport, detector codes, the reconstruction and analysis. In that way, changing settings or even the whole detector arrangement would neither require compiling nor the usage of another scripting language than C++ for the macro. Furthermore, the very same macros can be executed on any machine without changes (e.g. on a PC, a batch farm and even the grid).

Monte-Carlo Simulation and Detector Implementation

Running the simulations is centralized in the framework (using VMC, cf. figure 1.18). Detectors are defined as a composite of their geometry description as well as their functionality as sensitive elements. Access to the processing during the Monte-Carlo stepping in the selected engine is given by the detector base class.

Tasks

Execution of processes is organized in tasks, inheriting from ROOTs `TTask`. They allow a high modularity because tasks can be added, removed or replaced in the macros, providing a plug-in structure for the users. The framework organizes the delivery of input/output data containers, the parameter database connections as well as the task execution in the event loop. It is possible to keep temporary (transient) data between tasks in memory only, saving space on the hard disk. A sketch of how the tasks work is shown in figure 1.19. The setup connects to data and parameter container pointers. These are redirected by the framework to the actual containers during the run. Tasks can be grouped in a mother task, creating a hierarchy of execution, which is especially useful to provide default chains of tasks for production runs.

Parameters

The Runtime Parameter Database (RTDB) manages the I/O of parameters and their distribution to the tasks. The I/O to the ROOT file format enables the possibility to use more complex structures than a few numbers and strings, e.g. histograms, mathematic functions. Usually the whole geometry used during simulation is stored with the RTDB, which gives the possibility to apply changes due to alignment measurements later without reprocessing the data. The I/O to more sophisticated databases (e.g. to MySQL) is under development. Parameter sets are identified for each simulation run by a unique run ID, usually associated with one simulation file (or file set if separated).

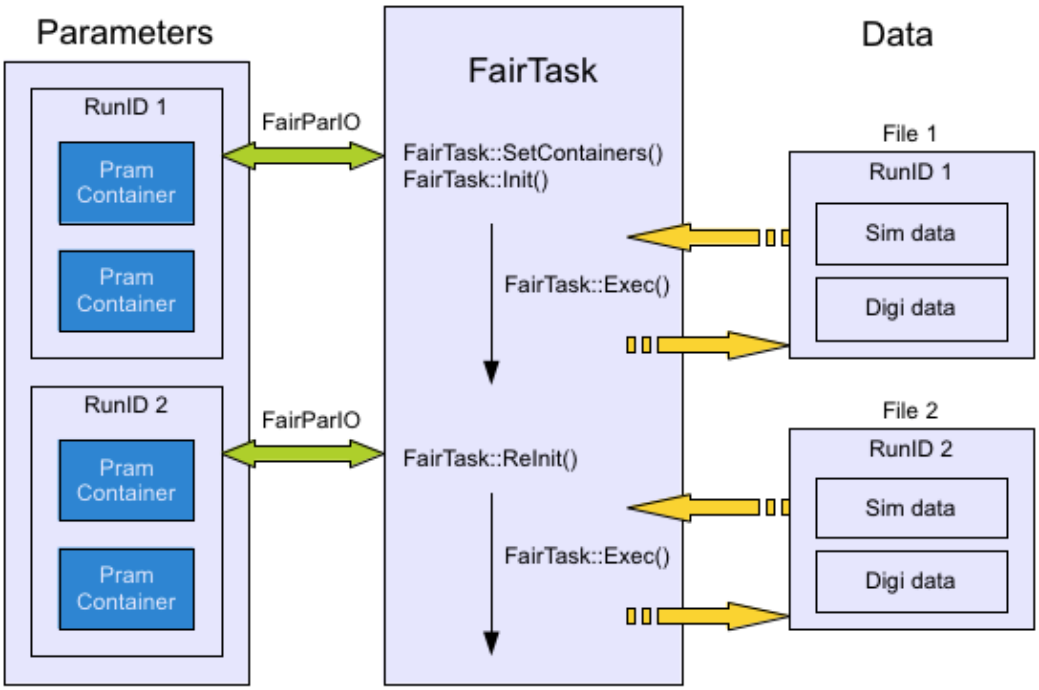

Figure 1.19: Schematic view of the process flow of `FairTask` and how data and parameters are accessed. Data and parameters are linked with a unique number.

As shown in figure 1.19 the tasks are provided in a centralized way with the matching data and parameter containers by the framework.

1.5.3 Software Workflow Scheme

In general the software has to simulate the whole experiment in order to develop the best suited detector hardware as well as the necessary algorithms for beam time data reconstruction. Measurement should then be comparable to simulated data so that the hadron physics model input can be studied thoroughly.

Such a software is a large and complex project, however it can be classified into a few main stages of processing, which occur consecutively. Figure 1.20 illustrates the chain of processing in form of such generalized stages. Simulation and real experiment data processing (starting on the left and right, respectively, in figure 1.20) merges at the point where the local detector reconstruction begins. Beforehand, in simulation the physics reaction has to be modeled with an event generator, then the particles have to be propagated through the detector environment and their relevant interactions with the sensitive elements are processed into detector specific data in the digitization. That output includes distortions and modifications typical for each detector and is similar to the measurement to be done in the actual experiment. On the other hand,

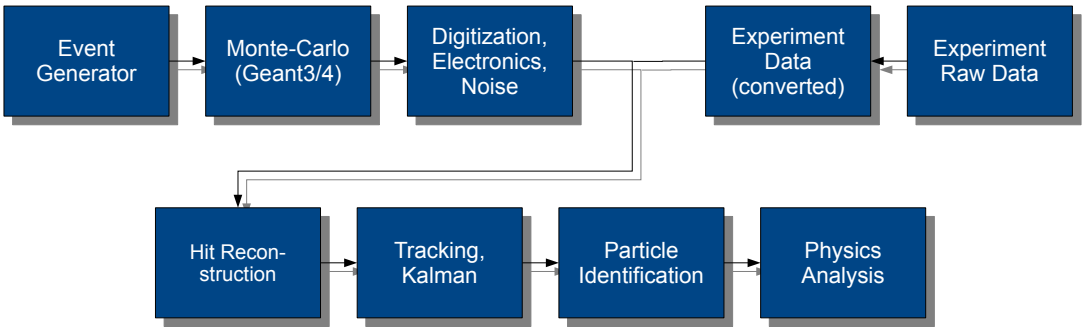

Figure 1.20: Schematic chain of major processing stages in PandaRoot.

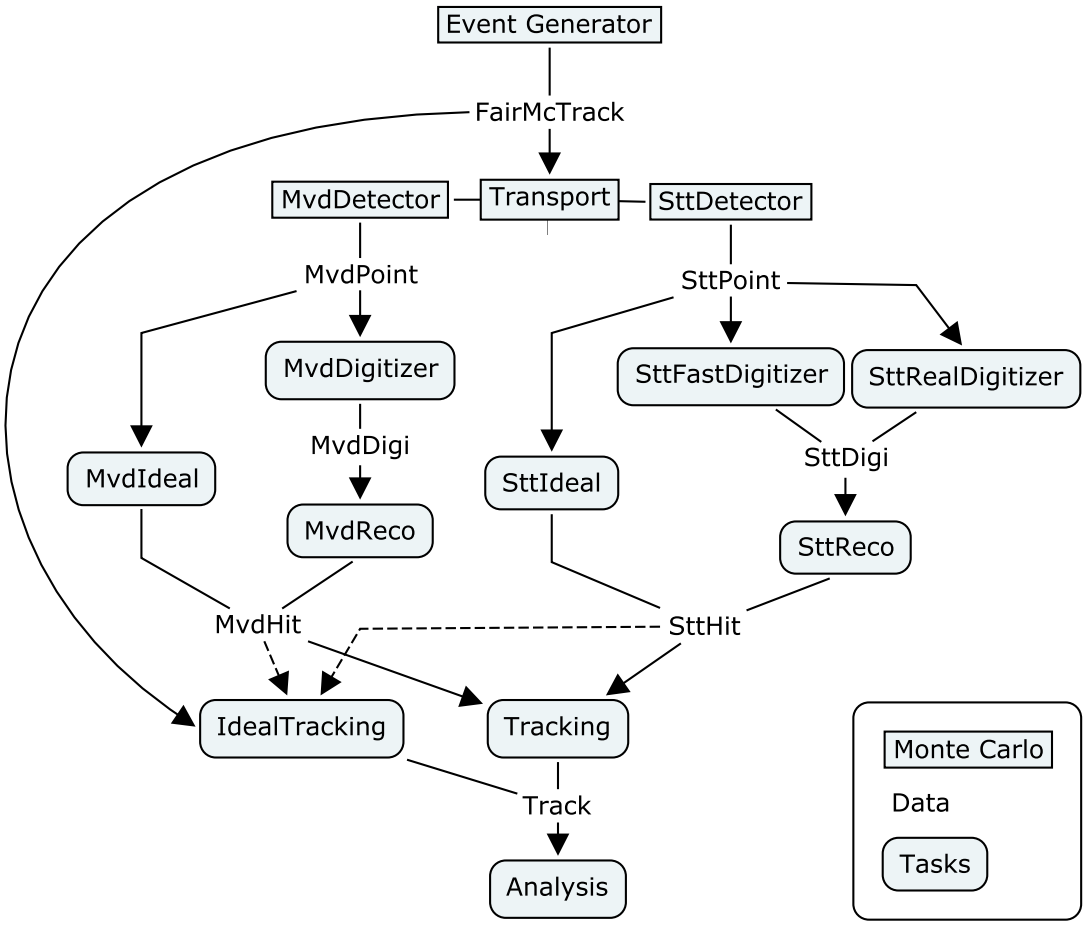

Figure 1.21: Example illustration of a task workflow in PandaRoot with the MVD and STT detector simulations. The modular design of the software allows to plug in the components necessary for each study.

real experiment data has to be prepared for processing with the reconstruction chain. Calibration and translation from the internal to the software-side description, e.g. channel number mapping, are performed. In the reconstruction chain connecting to both simulation and experiment the data are reconstructed in steps. First for each detector a local reconstruction is performed, then global actions such as the tracking pattern recognition take place, followed by fitting and particle identification (PID) algorithms. Finally, physics analysis can be performed on particle candidates, represented by production vertex and four-momentum, strongly depending on the physics case at hand. These stages will be described in more detail in this section.

In the framework the selection and the order of tasks create the structure of a simulation run. Figure 1.21 gives an example how tasks are connected to each other in the case of the MVD and STT together with the tracking. First is the Monte-Carlo processing of the generated particles is performed where each detector may be activated (and producing data) or put as passive material. To simulate the detector behavior a variety of tasks is available ranging from fast ideal tasks to detailed descriptions. Despite which path of processing is activated, the tracking has the necessary data always in the same format available. The same modular concept goes on for tracking, particle identification, etc giving the user the opportunity to select by his own criteria (e.g. detail, speed, simplicity) the optimal setup.

1.5.4 Event Generators

Gaining knowledge about hadron physics requires models describing the reactions under study. In order to evaluate the detector's efficiency and precision in a given physics case, the simulation needs the input of such models, realized in the event generators. Each particle in an event is described by its production point in space, charge and the four-momentum. According to the selected event generator these properties, and how many of which particles are produced, are distributed randomly. Several event generators are available in PandaRoot:

"Particle Gun" This event generator (`PndBoxGenerator`) emits particles of a specified kind randomly into a box in the momentum vector space: magnitude and two angles. The ranges are specified by the user as well as the number and species of the particles. Mainly this event generator is used for technical purposes and algorithm development, mostly shooting single particles.

EvtGen EvtGen [30] is a single-channel generator. This is done by specifying one decay chain. Each decay can be given an underlying decay model, the simplest of which is the phase space distribution. Many decay models for well known particles are present as presets, modifying the distributions of momenta and angles accordingly. It is possible to add user-defined models for special decays.

DPM The Dual Parton Model (DPM [31]) produces in PandaRoot particle distributions according to known cross-sections in a $\overline{p}p$ collision. Inelastic hadronic, elastic hadronic as well as Coulomb elastic scattering processes are implemented. The inelastic part produces many channels, from simple pion production to heavier resonances.

It gives a good possibility to accumulate simulated background events which are necessary to evaluate signal-to-background ratios of the detector system.

PYTHIA Developed at the Lund University, PYTHIA [25] is a background generator for $\overline{p}p$ reactions (and others) as well as a particle decayer. "*It contains theory and models for a number of physics aspects, including hard and soft interactions, parton distributions, initial- and final-state parton showers, multiple interactions, fragmentation and decay.*" [26] The focus of this package is on higher energies than present in $\overline{\text{P}}$ANDA. Both PYTHIA 6 (written in FORTRAN) and PYTHIA 8 (the successor in C++) are interfaced to PandaRoot.

UrQMD The UltraRelativistic Quantum molecular Dynamics Model (UrQMD [32, 33]) produces particle distributions for the reactions of antiprotons with heavy nuclei ($\overline{p}N$) as foreseen for the later stages of $\overline{\text{P}}$ANDA.

1.5.5 Detector Code

In PandaRoot the subsystems are represented in one package each, comprising one or a few class libraries. These packages follow the workflow described in 1.5.3 from Monte-Carlo processing via the digitization to the local reconstruction. Data classes are managed centrally by one library, making data usage independent of the detector libraries.

Monte-Carlo Processing

In each event the particles are processed with the Monte-Carlo engine. They are propagated in steps, being affected by scattering, energy loss processes, such as ionization, Bremsstrahlung, secondary particle production, and others. Each detector simulation has access to the stepping procedure inside its sensitive volumes. There, the current particle state e.g. momentum, species and its mother-daughter relation, and the current step's properties e.g. energy loss, local magnetic field strength and status flags, are available and according to the measurement principle of the detector. The necessary properties are recorded to the Monte-Carlo data structures. Tracking detectors store the position and total energy loss for each particle in a volume, whereas Cherenkov detectors keep information on position, direction and velocity of charged particles, and the electromagnetic calorimeters need information on every step's energy loss and particle of the shower. Calculations and actions in the stepping process are kept at a minimum, because of the high repetition rate of that particular code during the Monte-Carlo propagation.

Digitization

One of the simulation goals is to develop the reconstruction algorithms on simulated data and use them subsequently in the real experiment. Therefore a detailed detector description, the so-called digitization, is needed. Detector specific phenomena are emulated or simulated, such as the electron drift in each straw of the STT. Signal

shapes and electronic readout behavior are implemented as well, including the knowledge from the dedicated R&D and prototyping of $\overline{\mathsf{P}}$ANDA components. The produced data formats are close to the real experiment data, producing realistic conditions for the reconstruction algorithms.

Local Reconstruction

Raw data from a detector is rarely providing the necessary information directly. Each subsystem has to reconstruct hit points, total energies, times etc. to serve the global reconstruction algorithms. This also includes higher leveled reconstructions such as tracklet finding, cluster separation or even vertexing in order to gain fast event classification information, which can be used to filter for special event topologies. In the experiment the local reconstruction will be partially close at the detectors, to reduce the data stream efficiently. That implies algorithm integration inside the hardware e.g. on Field Programmable Gate Arrays (FPGA), to reach the necessary speed of processing.

1.5.6 Particle Reconstruction

Particles are represented by their charge, creation point, creation time and four-momentum. In $\overline{\mathsf{P}}$ANDA relatively stable charged particles (electrons, muons, pions, kaons, protons and their anti-particles) are measured as tracks, their momentum being calculated from the path curvature in the magnetic field. The fourth component of the four-momentum is obtained from the particle identification systems, fixing the particle mass.

Track Pattern Recognition

Track finding and pre-fitting is the goal of the pattern recognition. Its task is to collect all hits of the tracking detectors belonging to one trajectory into a track candidate. Particle tracks in the solenoidal field of the barrel spectrometer have the shape of helices, being straight lines in the l-z projection[5] and circles in x-y view. Therefore the hits are mapped from the x-y plane with the conformal mapping method [34], creating straight lines from the circles. Treating the tracks as helices is an approximation, neglecting distortions introduced by scattering as well as the increase of the curvature from energy loss, therefore selections have to be fairly loose in order to achieve a good hit collection efficiency. The lines in the conformal space are searched for and fitted. In combination with the straight line fit in l-z the track helix parameters are extracted as seed value for the complete track fit. An example view of a track in the STT is shown in figure 1.22 both in the x-y and ϕ-z projections[6].

The biggest issue is the huge amount of possible hit combinations, that may form a track, leading to a huge computing time. The strategy to lower the number of combinations prior to the conformal mapping is to search for tracklets in the subsystems and then matching these. In the case of the MVD, which yields only a few hits in

[5] l is the trajectory length

[6] ϕ is used instead of l for tracks with large radii (thus not doing a second turn in the detector).

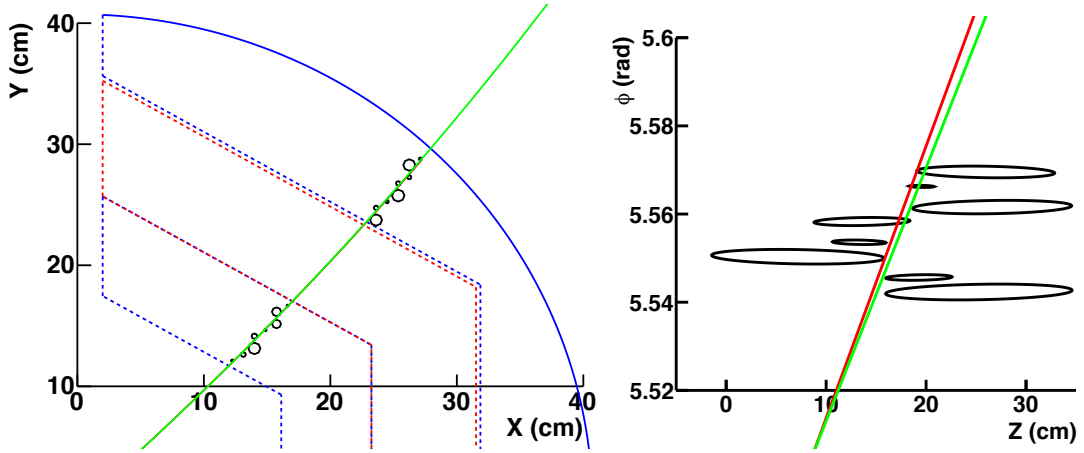

Figure 1.22: Pattern recognition stages in the STT: Circle fit to hits in straight straws in x-y projection (left) and line fit to skewed straw hits in ϕ-z projection (right). (figures from [13])

each event, the hits are projected from the x-y plane to a Riemann Sphere [35]. Hits belonging to a track are then lying on one plane, which is being fit to deduce the helix parameters in combination with the straight line fit in the l-z view. In the case of the STT, the preprocessing is reducing the number of hits to the planar straws together with the scintillating tiles as timing information. Using the same conformal mapping and track following, the helix parameters are estimated. After merging the tracklets, unassigned hits including the ones from the GEM stations are matched. Finally the algorithm runs on the remaining hits, which are now considerably less through the identification of the easy-to-find tracks.

Track Fitting

Particles traveling through matter will scatter on their path and will lose energy as well. Small angle elastic scattering is a random process with a constant expected track path and a variance growing with the amount of material crossed. The energy loss, on the other hand, is modifying the trajectory systematically in one direction, increasing the curvature ($\sim 1/p_t$) and the variances on the path. These circumstances and the inhomogenities of the magnetic field strength from the nominal 2 T in the outer tracker region require a dedicated track fitting method.

This track fitter is GENFIT [36], a general fitting package based on the Kalman Filter technique [37, 38]. It provides interfaces to different measurement types, such as 3D hit points, planar hits and wire hit information. Tracks are represented in coordinates of choice, in $\overline{\text{P}}$ANDA these are helix parameters in the barrel spectrometer and a parabola representation in the forward part. The track parameters are calculated at both ends of the measured trajectory providing optimal values close to the vertex of the track and close to the outer detection systems (e.g. DIRC and EMC). Propagating forth and back along the track, for each measured hit an extrapolation to the hit's measurement plane is made and the track parameters are updated by the measurement. For the propagation and extrapolation GEANE [39, 40, 41] is used, taking into account the scattering, energy loss and the magnetic field by modifying

the extrapolated trajectory state and its covariance accordingly. The same propagation tool can be used in later steps e.g. to see if a cluster in the EMC originated from a charged track or a photon.

PID

Almost every subsystem has a momentum range for each particle species in which it can contribute to the particle identification. Each system has its own algorithm to calculate the probability density functions (pdf) for each particle hypothesis. With the bayesian approach, assuming all variables contributing are independent to each other, all pdf's are combined into a global likelihood:

$$L_{\text{total}} = f \times p_{\text{MVD}} \times p_{\text{STT}} \times p_{\text{EMC}} \times \dots \tag{1.1}$$

and it is possible to obtain the probability for each particle ID. In order to obtain the likelihood for a particle being of a certain species, the combined pdf's p_k have to be weighted with the particle flux f of the particle type in question with the measured kinematics and in that detector region. Additionally, several multi variate analysis (MVA) classification methods are available to gain the most of the information of all detectors involved. Available are a K Nearest Neighbors Classifier (KNN), a Learning Vector Quantization Classifier (LVQ) as well as the interface to the ROOT classifiers in the TMVA package. These classifiers have to be trained with simulated data before they can be used, but promise a better separation than the bayesian approach in "difficult" regions. This includes the correct treatment of many variables and their correlations, such as suppressing hadronic background in electromagnetic channels.

1.5.7 Physics Analysis Tools

At the end of the chain of processing stands the analysis of physics events on the level of particle candidates formed from charged tracks and neutral measurements. There are certain standard operations such as creating composite particles, applying cuts and applying fits. In order to provide an efficient way of working with these particle candidates the RHO package [42] is introduced, selected parts ported to PandaRoot from the BETA [43] analysis package of the BaBar experiment and extended by the necessary functionalities.

Rho

Particle candidates are created from tracks and neutral clusters in the calorimeters. The management of these is governed by the Rho package. It comprises a mechanism to combine particle candidate lists, enabling the reconstruction of whole decay trees. Notably the package takes care of combinatoric double counting by indexing the candidates. Selectors are used to apply criteria (e.g., mass or PID cuts) to whole candidate lists. The access to the PID classifier outputs, the measured tracks as well as the Monte-Carlo truth is provided, too. Such mechanisms considerably lower the threshold of programming expertise that is necessary to actually perform a physics analysis.

Fitting

A few fitting algorithms are implemented in the analysis tools. Fitted candidates are produced in addition to the original ones, giving the possibility to use differently treated candidates for different purposes.

Mass Fitter By constraining the four-momentum of a candidate with a mass hypothesis, the other variables are adjusted accordingly. For example all two-gamma candidates suiting the mass window of neutral pions are given the known π^0 mass value.

4C Kinematic Fitter A kinematic fitter is fitting the four-momenta of a decay chain to match best with the interaction point. Introducing the initial state, i.e. the knowledge of the beam properties, four constrains (the initial state's four-momentum) are used to improve the result accordingly.

Vertex Fitter Vertex fitters improve the four-momenta of one delayed decay under the hypothesis that all daughter tracks originate from the same creation point, their vertex. A detailed description of vertex fitting and the implementations in PandaRoot are given in chapter 3.

1.5.8 Radiation Length Information

FairRoot provides the possibility to store properties of materials seen by the particles during the Monte-Carlo stepping procedure. For each volume that particle passes, entry and exit point are stored, as well as the real path length inside the volume and the properties of the materials encountered. Especially the radiation length X_0 is of great interest. This allows to easily create material budget maps with the very same geometry used in the simulations together with the particles used in the simulations. It is to be noted that such procedure consumes a lot of calculation time as well as storage space, because there are much more passive volumes than active ones. Especially the EMC needs such information to estimate how strong the measured particles have been distorted and how much secondary particles are created in the layers before to separate signals from background efficiently.

1.5.9 Fast Simulations

Executing the full chain of processing requires much computing time and resources, as especially resource-consuming calculations are performed in the Monte-Carlo engine, the track finding and track fitting. For many applications, such as the first studies on a physics case or developing physics analysis algorithms, it is not vital to have the full detail of the simulations and approximations can be applied.

Ideal Algorithms To circumvent heavy calculations in the detector parts, the tracking and particle identification, each package has an "Ideal" task which passes

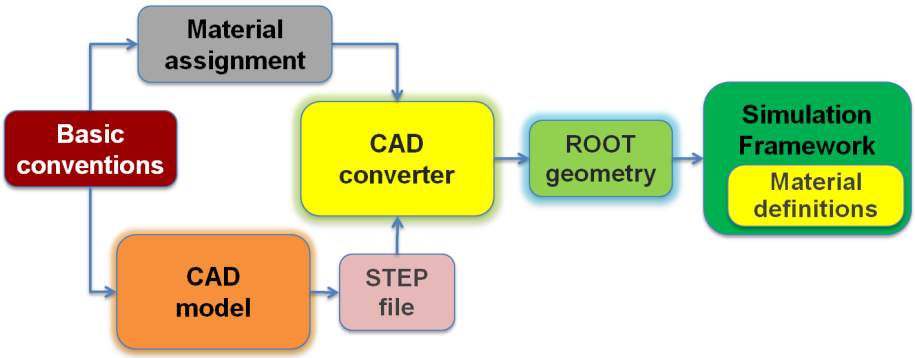

Figure 1.23: Structure of the CAD to ROOT conversion. Volumes are converted from the STEP file, whereas material types are assigned separately. Material definition is performed in the simulations.

the Monte-Carlo information on directly or redistributes the data by Gaussian smearing. This approach is very helpful when developing one detail of the system and does not need the heavy calculations and distortions of the other parts.

FastSim For the case when a more or less realistic detector answer is needed, but processing speed is important the fast simulation has been developed. It emulates (class `PndFsmCombiDet`) only the main features of the detector answer, by applying acceptance and efficiency cuts and redistributing (Gaussian smearing) the track momenta and vertices with parametrized resolutions and covariances.

1.5.10 CAD to ROOT Converter

Complex systems in a tight environment such as the MVD are designed with the aid of CAD programs. These drawings are used directly by the engineers to manufacture the components of the system. Because these drawings contain the whole and detailed geometry it is favorable to utilize them in the simulations as well. Therefore a converter from the CAD output (STEP format [44]) to the geometry description format of ROOT was developed in the MVD group [45]. Figure 1.23 shows the converter layout, especially how material types are handled. Because it is necessary to study different material setups with the same geometry, the assignment of the material types to the STEP volumes is performed separately. The definition of the materials is performed in the simulation run and allows to study e.g. different cabling materials etc. A detailed an unambiguous naming convention was introduced for the MVD [46] to create conformity amongst CAD drawing and simulated geometry.

Chapter 2

Silicon Detector Software

$\overline{\text{P}}$ANDA is one of the modern large scale experiments where the simulation software studies the detector behavior before the actual detector is built and commissioned. Because of the high demands on the detector performance in terms of resolution, particle transparency (low material budget) and data loads as well as because of the idea of having the analysis tools and methods ready for the first data taking, the simulations have to be as realistic as reasonably possible.

In the simulations silicon strip and pixel sensors of $\overline{\text{P}}$ANDA have to be modeled in their behavior and realistic reconstruction code is needed. Not only the MVD features silicon sensors but also the Luminosity Monitor and the Hypernuclear experiment extension. Therefore, a dedicated software package, called Silicon Detector Software (SDS), has been developed. It conceptually foresees one generalized package for all silicon detectors in $\overline{\text{P}}$ANDA. Each detector implementation is then light-weighted and done by the C++ inheritance mechanism. Currently available implementations are the MVD and the Luminosity Monitor and the SDS has been used in simulation-data comparisons for the silicon tracking station in Bonn [47].

2.1 SDS Layout

The SDS package is embedded within the PandaRoot framework, using its interfaces and mechanisms. Each major part of processing is done within a `FairTask` which is by its conception reading event by event one stage of data, processing it and writing the next stage of data to be accessed by another task. This modularity allows a step-by-step production of simulation data and to run different settings on the same set of data.

Following the sequential chain of processing, as illustrated in section 1.5.3, the SDS package can be separated into the following stages, represented by a task each (task class name are given in brackets):

- Monte-Carlo Particle Transport (`PndSdsDetector`)
- Digitization (`PndSdsHybridHitProducer`, `PndSdsStripHitProducer`)
- Reconstruction (`PndSdsPixelClusterTask`, `PndSdsStripClusterTask`)

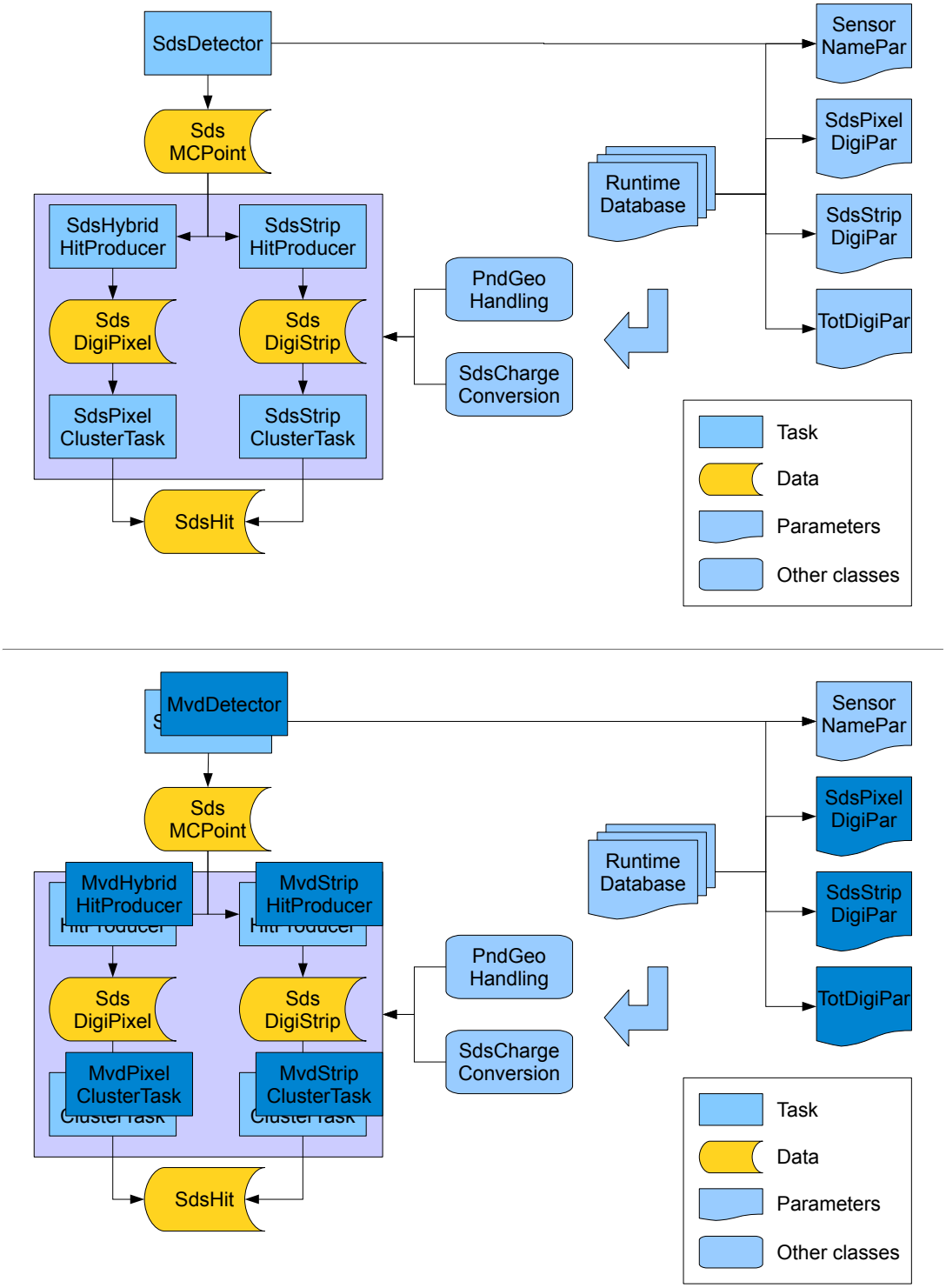

Figure 2.1: Schematic layout of the SDS package (above) and the implementation of the MVD specialization (below in dark blue). Tasks are inherited and specify only parameter names and setups. Matching parameter sets are loaded from the RTDB atomically.

Each step produces dedicated data structures, each employing as little data load as possible. Interpretation, especially the identification of the sensors, is done together with the geometry definition and its mapping parameters. The layout is sketched in the upper part of figure 2.1.

During the Monte-Carlo stepping the Detector class creates Monte-Carlo points which are processed by the digitizers (HitProducers) according to the sensor parameters to digis, the fired channels. "ClusterTasks" reconstruct then hits which are made available for tracking and PID later on.

There are only a few things in the SDS package which are not generalized for all silicon detectors in $\overline{\mathsf{P}}$ANDA. Each detector implementation is done in a "light-weighted" manner by C++ inheritance. As depicted in the lower part of figure 2.1 the task classes for Monte-Carlo simulation, digitization and reconstruction are specified. However, only a few virtual functions are implemented in the specification which define the data branches as well as what parameter sets and algorithm classes are to be used.

2.2 Monte-Carlo Particle Transport

Particles produced in the event generator are transported by the selected Monte-Carlo engine through the geometry setup and magnetic field, while undergoing material effects such as ionizing energy loss and delta electron production. When a particle crosses an active volume associated with a `PndSdsDetector` class, a Monte-Carlo point (`PndSdsMCPoint`) is created. It contains the entry and exit coordinates and momenta, the total energy loss inside the volume, as well as the exact time of the particle's flight before entering the volume. Charged particles create electron-hole-pairs on their path. The charge carriers produced in the sensor's depletion zone are measured at the contacts. For the creation of one electron-hole-pair 3.6 eV of energy loss are necessary [48]. For a minimum ionizing particle (MIP, $\mathrm{d}E/\mathrm{d}x \approx 1.2\,\mathrm{MeV}\cdot\mathrm{cm}^2/\mathrm{g}$) in silicon ($\rho = 2.33\,\mathrm{g/cm}^3$) this translates to 78 electrons/µm worth of signal. The MVD sensor's active thickness will be in the order of 100 µm to 250 µm, thus yielding signals of about 7500 to 20000 electrons per minimum ionizing particle. Energy loss calculated by the Monte-Carlo engine is directly transformed into a number of electrons and stored in the Monte-Carlo points.

Because this part of the software is called very often during the particle propagation stepping of the Monte-Carlo engine, high performance is necessary. Calculations are kept at a minimum and only those elements are calling the stepping and storing of the points which are marked active (i.e. the sensor volumes). Whether a volume is active is defined in SDS through its geometry name, e.g. "StripActive" identifies all strip sensors in the MVD. A thorough volume naming convention is essential for such a scheme (see figure 1.17 for the coarse heirarchy). A view of the active elements of the MVD (geometry version 1.0) in the simulations is shown in figure 2.2 together with five proton tracks and the Monte-Carlo points they created.

Passive detector components, such as holding structures, cooling, readout chips and cabling, contribute with their material budget to scattering, energy loss, secondary particle production, etc. Although no data are stored, a good description of the passive components is essential for realistic detector simulations, as scattering will limit the

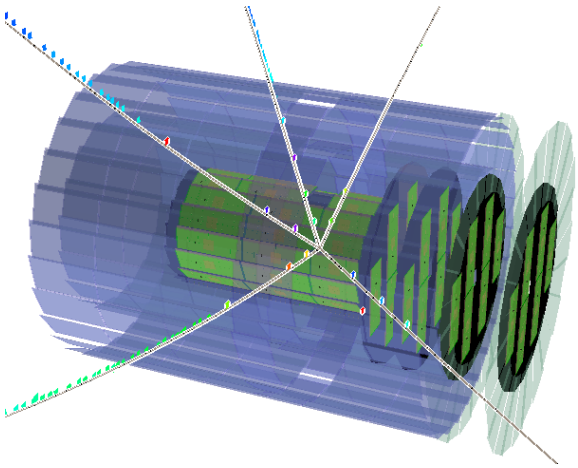

Figure 2.2: MVD sensitive volumes: Pixel sensors in green and transparent blue strip sensors drawn with the event display of PandaRoot. The five lines are proton tracks with 1 GeV/c and the colored squares are Monte-Carlo points in the MVD (version 1.0) and STT (not drawn).

achievable resolution, secondary particles will introduce background signals (e.g. to the electromagnetic calorimeter), and anisotropic material distributions (especially hotspots) will introduce anisotropic resolutions and efficiencies.

2.3 Digitization

Digitization is the emulation of the detector answer, similar to what a data acquisition system would receive from the readout electronics. Silicon detectors in high energy physics usually have a planar shape and either pixel or strip readout structures, with an integrated amplification, digitization and first-level data processing system connected, the front-end chip. Both the structuring and the electronics have to be modeled by the software.

Monte-Carlo points from the transport engine are digitized into the data formats `PndSdsDigiPixel` and `PndSdsDigiStrip`, resembling each single fired strip or pixel, respectively. These so-called digis identify the strip or pixel itself as well as the involved front-end chip and the sensor volume. Additionally the measured charge is stored and the time stamp of the measurement.

2.3.1 Geometric Digitization

The entry and exit coordinates of the particle as well as the ionizing charge information from the energy loss are used to calculate which pixels or strips fired. For double sided strip detectors this is done for both readout sides independently.

By definition each sensor volume's local coordinate system originates in the volume center (see figure 2.3). Each volume is present in the global ROOT based geometry. It is organized hierarchically with nested so-called assemblies, each being basically a translation and a rotation operation to a group of lower level assemblies. Physical volumes are the lowest level in the hierarchy. The tree of assemblies and volumes

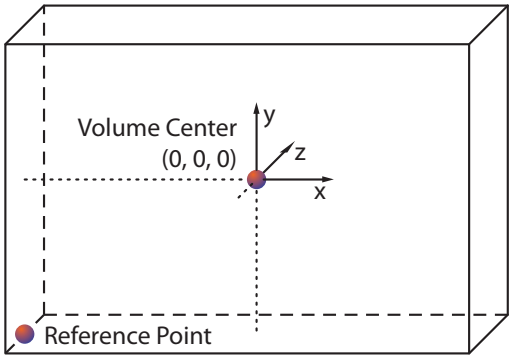

Figure 2.3: Schematic view of the reference point and local coordinate system definition.

is accessed by a directory structure created from the assembly and volume names. Identifying one silicon sensor requires the full path of assemblies. Because that information is necessary in the data objects it is convenient to index the sensitive volumes by an integer number, the sensor id. The class `PndGeoHandling` manages that indexing and stores the mapping in the runtime database. Furthermore that class provides the transformation between the local sensor frame and the laboratory system by the assembly path or the sensor id's. The gain of a drastically reduced data object size is bought with the comparably small computing time necessary to access the mapping.

It is convenient to count pixel and strip numbers on the sensor surface with positive integers, hence the reference starting point for that is the lower left corner (see figure 2.3) in the local sensor system. Pixel column numbers are defined to run along the x-axis and the row numbers along the y-axis.

Linear Model

Inside thin silicon detectors the particle trajectories can be approximated to straight lines. To calculate which readout channel measures what charge, the trajectory is projected to the sensor surface. The charge is then distributed relative to the lengths of the trajectory pieces in the readout channels (see figure 2.4). For strip and pixel structures, respectively, this is expressed as:

$$Q_i = Q \cdot \frac{|x_{i,\mathrm{out}} - x_{i,\mathrm{in}}|}{|x_{\mathrm{out}} - x_{\mathrm{in}}|} \qquad \text{(strips)} \tag{2.1}$$

$$Q_{i,j} = Q \cdot \frac{|x_{i,\mathrm{out}} - x_{i,\mathrm{in}}|}{|x_{\mathrm{out}} - x_{\mathrm{in}}|} \cdot \frac{|y_{j,\mathrm{out}} - y_{j,\mathrm{in}}|}{|y_{\mathrm{out}} - y_{\mathrm{in}}|} \qquad \text{(pixels).} \tag{2.2}$$

These charge entries are then processed by the electronic digitization.

Static Charge Cloud Model

Assuming, as in the linear model, that the trajectories inside the sensor volumes can be approximated by straight lines, one can project to one and two dimensions for strip sensors and pixel sensors, respectively. The created charge carriers then move

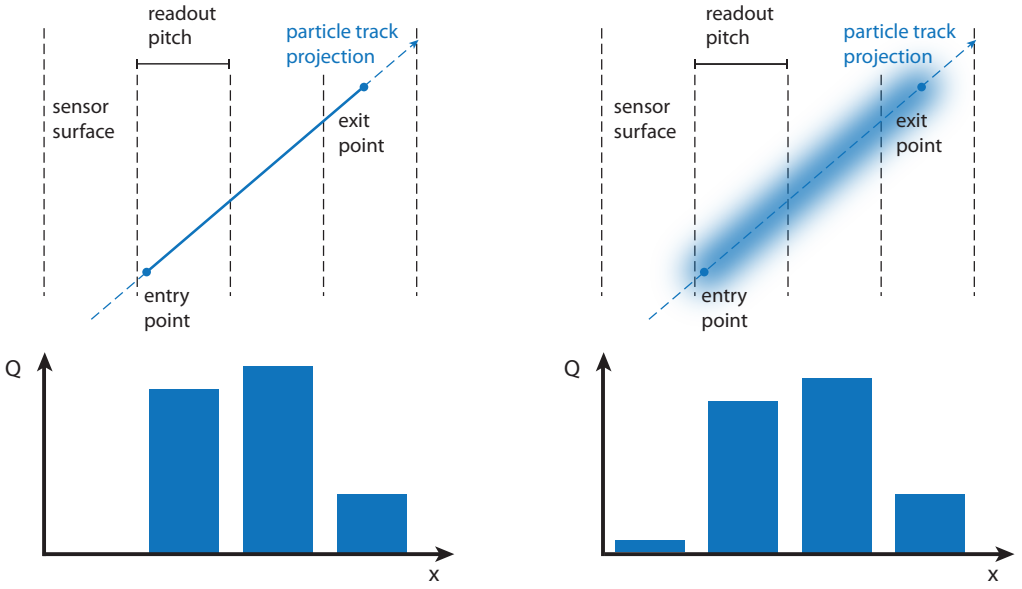

Figure 2.4: Schematic sensor surface view (projection) of the track piece inside the sensor volume between the entry and exit point. The linear digitization model (left) and the one with a charge cloud (right) produce the charge distribution on the illustrated charge distributions at the readout cells.

in the electric field to the readout pads. Due to scattering, the path is not linear but distorted. This is modeled by a Gaussian probability density function around the charge carrier creation point's projection onto the readout surface. The charge is measured via the induced current originating from the electric field of all charge carries along the particle path. The differential charge, depending on the coordinate of measurement x and the point on the path projection x', is then expressed as

$$\frac{\mathrm{d}\tilde{Q}(x', x)}{\mathrm{d}x'\mathrm{d}x} = \frac{Q}{p \cdot |x_{\text{out}} - x_{\text{in}}|} \cdot \frac{1}{\sqrt{2\pi}} \cdot e^{\frac{(x'-x)^2}{2\sigma^2}}, \tag{2.3}$$

where Q is the total charge, $p = |x_i - x_{i+1}|$ the readout structure size (pitch) and $|x_{\text{out}} - x_{\text{in}}|$ the path length. The width σ of this cloud of charge carriers is a parameter which is calculated for 300 µm thick silicon [48] to be

$$\sigma = \sqrt{\frac{kT}{q} \cdot \frac{2\epsilon\epsilon_0}{qN_0}} = 5.81\,\mu\text{m}. \tag{2.4}$$

Integrating over the whole particle path and over the considered channel number i, spanning from x_i to x_{i+1}, that channel measures a charge:

$$\begin{aligned} Q_i &= \frac{Q}{p \cdot |x_{\text{out}} - x_{\text{in}}|} \cdot \int_{x_{\text{in}}}^{x_{\text{out}}} \mathrm{d}x \int_{x_i}^{x_{i+1}} \mathrm{d}x' \, \frac{1}{\sqrt{2\pi}} \cdot e^{\frac{(x'-x)^2}{2\sigma^2}} && (2.5) \\ &= \frac{Q}{p \cdot |x_{\text{out}} - x_{\text{in}}|} \cdot \int_{x_{\text{in}}}^{x_{\text{out}}} \mathrm{d}x \, \frac{1}{2} \left(\operatorname{erf}\left(\frac{x_i - x}{\sqrt{2}\,\sigma} \right) - \operatorname{erf}\left(\frac{x_{i+1} - x}{\sqrt{2}\,\sigma} \right) \right) && (2.6) \\ &= \frac{Q}{p \cdot |x_{\text{out}} - x_{\text{in}}|} \cdot \frac{1}{2} \left(F_i(x_{\text{out}}) - F_i(x_{\text{in}}) - F_{i+1}(x_{\text{out}}) + F_{i+1}(x_{\text{in}}) \right). && (2.7) \end{aligned}$$

With $F_k(t)$ representing the primitives of the error function ($\operatorname{erf}(x)$) for each strip k:

$$F_k(x) = (x_k - x) \cdot \operatorname{erf}\left(\frac{x_k - x}{\sqrt{2}\,\sigma} \right) + \sqrt{\frac{2\sigma^2}{\pi}} \cdot e^{-\frac{(x_k - x)^2}{2\sigma^2}}. \tag{2.8}$$

For small path projections ($|x_{\text{out}} - x_{\text{in}}| \approx 0$) the problem reduces to one point-like source spreading the charge by the Gaussian. Because of the substantial amount of tracks passing, by design, nearly perpendicular through the sensors, saving on computing-expensive functions such as the error function and the Gaussian distribution is possible. The integral over x in equation 2.5 collapses and the measured charge in strip i is then

$$\begin{aligned} Q'_i &= \frac{Q}{p \cdot \epsilon} \cdot \int_{-\epsilon/2}^{\epsilon/2} \mathrm{d}\epsilon' \, \frac{1}{2} \left(\operatorname{erf}\left(\frac{x_i - x - \epsilon'}{\sqrt{2}\,\sigma} \right) - \operatorname{erf}\left(\frac{x_{i+1} - x - \epsilon'}{\sqrt{2}\,\sigma} \right) \right) && (2.9) \\ Q'_i &= \frac{Q}{p} \cdot \frac{1}{2} \left(\operatorname{erf}\left(\frac{x_i - x}{\sqrt{2}\,\sigma} \right) - \operatorname{erf}\left(\frac{x_{i+1} - x}{\sqrt{2}\,\sigma} \right) \right). && (2.10) \end{aligned}$$

For the pixel sensors it is necessary to take the second readout dimension into account. Using the same idea as before we express the charge density by a Gaussian distribution in two dimensions:

$$\frac{\mathrm{d}\tilde{Q}(x', y', x, y)}{\mathrm{d}x'\mathrm{d}y'\mathrm{d}x\mathrm{d}y} = \frac{Q}{p_x p_y |x_{\text{out}} - x_{\text{in}}| \cdot |y_{\text{out}} - y_{\text{in}}|} \cdot \frac{1}{2\pi} \cdot e^{\frac{(x'-x)^2}{2\sigma_x^2}} \cdot e^{\frac{(y'-y)^2}{2\sigma_y^2}}. \tag{2.11}$$

Performing the calculations, similar to the ones above, the charge $Q_{i,j}$ in one square pixel ($p_x = p_y$) is

$$\begin{aligned} Q_{i,j} = \frac{Q}{4p \cdot |x_{out} - x_{in}| \cdot |y_{out} - y_{in}|} \\ \cdot \left(F_i(x_{out}) - F_i(x_{in}) - F_{i+1}(x_{out}) + F_{i+1}(x_{in}) \right) \\ \cdot \left(F_j(y_{out}) - F_j(y_{in}) - F_{j+1}(y_{out}) + F_{j+1}(y_{in}) \right). \end{aligned} \tag{2.12}$$

These charges are then subject to the electronic digitization.

2.3.2 Electronic Digitization

The answer of the preamplifiers to an induced charge at a readout channel can be modeled in various ways. These models describe how the charge information itself

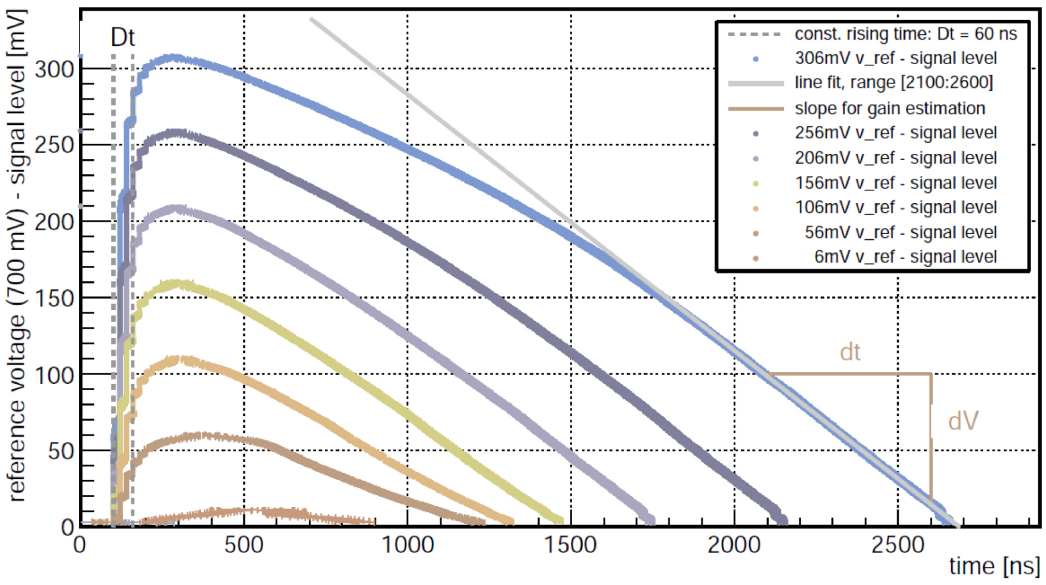

Figure 2.5: Signals from reference pulses measured on the ToPix 2 prototype chip [1]. It features the constant peaking time as well as the constant slope on the falling edge.

is digitized, its associated electronic noise is handled and how the time information is digitized. The organization of the code is such that one of several models can be chosen through the digitization parameters. Apart from the ideal case (passing on the Monte-Carlo charge and time values), a Time Over Threshold (ToT) model and an Analog-to-Digital Converter (ADC) are implemented. Further models are easy to implement in accordance with future hardware developments.

Analog to Digital Converter

An ADC sorts a continuos measurement Q into integer bins.

$$\mathrm{ADC} = \mathrm{ceil}\left(\frac{Q - Q_{\mathrm{Thr}}}{Q_{\mathrm{Bin}}}\right) \tag{2.13}$$

The settings comprise the bin size Q_{Bin} as well as the resolution bit number, which translates here to the number of available bins. The time stamp is generated by simply rounding off to the next full nanosecond.

Time Over Threshold

In the hardware design of TOPIX, the pixel front-end chip of the MVD [1], the charge measurement is done with the time-over-threshold method (ToT). In principle, the charge arriving at the input capacitor is integrated by a charge sensitive amplifier (CSA). With a constant current source the capacitor is then discharged, constantly

lowering the amplifier's output. The time the amplifier output is above a given threshold is proportional to the deposited charge.

A series of signal curve measurements for the TOPIX 2 prototype front-end chip is shown in figure 2.5. The rising edge of the signal is steep and reaches its peak in a constant time and the falling edge is at a constant slope. Only at high and very low charge entires deviations from the ideal behavior become important, which will result in a nonlinear calibration.

Triangular Signal Shape At the amplifier output the signal is approximated with a triangular shape [49]. The signal's rising edge is linearly charging the capacitor within a constant peaking time t_{peak} and the capacitor discharges with the constant current source I_{dis}, thus lowers the output linearly over time. Both crossing times of the signal with the threshold are calculated, the difference being the time over threshold (ToT value).

$$t_{\text{ToT}} = \left(\frac{t_{\text{peak}}}{Q} - \frac{1}{I_{\text{dis}}} \right) (Q - Q_{\text{Thr}}) \tag{2.14}$$

Digitized in numbers of clock cycles the time at the rising edge becomes the time stamp of that digi (see 2.3.2). The implementation is done in the `PndSdsTotChargeConversion` class, which is steered with a dedicated parameter set, where the necessary values are specified (see table 2.1).

Parameter	Type	Unit	Description
charge_time	`Double_t`	[ns]	Constant time of the rising edge
const_current	`Double_t`	[e^-/ns]	Constant discharge current
clock_frequency	`Double_t`	[MHz]	Time measuring clock frequency

Table 2.1: Time-over-threshold digitization parameters

Detailed Signal Shape A more realistic signal shape can be introduced by a user defined model, a one-dimensional function $Q_{\text{FE}}(t)$ which in particular can be obtained by measurement at the actual hardware. The ToT value and time walk are calculated directly from the inverse function which is more accurate, however that level of detail is not necessary for common simulations with the whole $\overline{\text{P}}$ANDA setup. Studies of the effect of different front-end chips and their settings will benefit from the generalized concept. The implementation is in the `PndSdsFe` class and classes derived from that which are separated from the charge conversion structures.

Noise emulation

Electronic noise has the character of a Gaussian distributed charge, centered around the baseline with the width of σ_{Noise}. It is sensible to define the noise baseline level as the nominal zero in the simulations. Baseline (or pedestal) corrections will be done at hardware level, also capturing baseline drifts. The noise has two effects, the distortion of measured signals and the creation of fake hits, mostly at low energies.

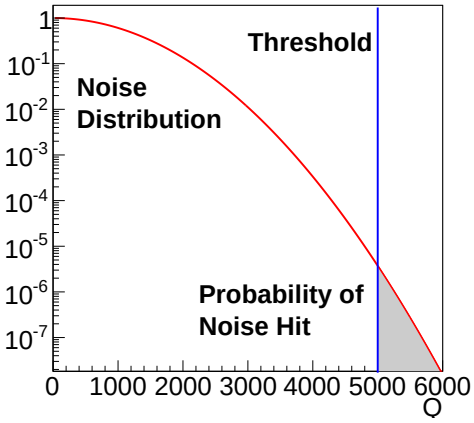

Figure 2.6: Illustration of the probability for a readout channel to produce a noise hit (grey area).

Each charge measurement in a strip or pixel is redistributed by the noise Gaussian, centered around the initial charge value and its width σ_{Noise}. From measurements on test sensors we find the noise values to be in the order of $\sigma_{\text{Noise}} = 200$ electrons for pixel sensors and $\sigma_{\text{Noise}} = 1000$ electrons for the strip sensors [1]. A discriminating threshold cut is applied to suppress low-charge entries as the readout electronics with zero suppression will do. Usually the threshold is set to a level of $5\,\sigma_{\text{Noise}}$. That threshold is the same as introduced with the ToT method.

The Gaussian tail of the noise distribution reaching over the threshold will produce hits by the noise statistics (see figure 2.6). This is taken into account by adding noise hits above the threshold. The number of those noise hits is distributed by a Poissonian random distribution with its mean value being dependent on the threshold and noise settings as well as the number of readout cycles done in a time window identifying an event. It is

$$< N_{\text{Noise}} >= N_{\text{channels}} \cdot t_{\text{evt}} \cdot f_{\text{clock}} \cdot \frac{1}{2} \operatorname{erfc}\left(\frac{Q_{\text{Thr}}}{\sqrt{2}\,\sigma_{\text{Noise}}}\right) \tag{2.15}$$

while t_{evt} is the time interval from the previous event and f_{clock} the bus readout frequency. N_{channels} is the total number of channels and $\operatorname{erfc}(x)$ is the complementary error function expressing the fraction of noise above the threshold. The noise hits are then randomly distributed amongst the sensors and their readout channels.

Time Stamp Generation

Each measurement will be marked by the electronics with a time stamp. This will enable the collection of all the information belonging to the same physics event. The time stamp is defined by the time when the signal crosses the threshold at the rising edge (which could be in figure 2.5 e.g. 50 mV). Because the rise time is not negligible (in the order of 50 ns) this introduces a systematically shifted time, compared to the

actual time of the physical hit. This is called time walk

$$t_{\mathrm{W}} = t_{\mathrm{rise}} \cdot Q_{\mathrm{Thr}}/Q. \tag{2.16}$$

The time stamp is then calculated from the event time (t_{evt}) and the time the particle took to fly towards the sensor (t_{tof}):

$$t_{\mathrm{stamp}} = t_{\mathrm{event}} + t_{\mathrm{tof}} + t_{\mathrm{W}}(+\Delta t_{\mathrm{digi}}) \tag{2.17}$$

Time stamps can only be measured as multiples of one clock cycle which limits the precision. This is indicated with the time difference Δt_{digi} from the actual time to the next digital value. For a timing clock speed of 50 MHz the bin size is 20 ns.

2.4 Local Reconstruction

Interpreting the measurement from a sensor or the data stream from a simulation are, by design of the software, one and the same problem. Fired channels have to be combined to clusters, hit positions have to be reconstructed, as well as the deposited charge and the correct time of passage. Only the link to the Monte-Carlo truth information distinguishes simulation from experiment data.

2.4.1 Cluster Finding

A cluster is a collection of signaling strips or pixels, which are expected to originate from the same hit of a particle. To belong to a cluster a digi must be in the vicinity of others, defined by a radius parameter. By default this parameter is set to include the next neighbors. For the rejection of ghost clusters, usually containing only one noise digi, a threshold for the sum of all charges must be reached.

2.4.2 Hit Reconstruction

To retrieve the hit information the cluster centroids have to be calculated. Each centroid provides information in the local x-y frame, parallel to the sensor plane (see figure 2.3) while the local z coordinate is always zero, i.e. on the central plane in the sensor. In the case of the Strip sensors, the centroids give one-dimensional information on both sensor sides. Translation and rotation operations, managed by the geometry handling, transform the local hit to the laboratory frame for further processing.

Centroid Calculation

There are several centroid calculation approaches known, i.e. the binary algorithm, the charge weighted mean, the eta algorithm as well as the head-tail algorithm (cf. [50]).

Binary Center: The binary centroid lies exactly in the center of the digi with the highest charge entry. In the case of only one digi in a cluster that is of course the only information available. The uncertainty is a fixed number and known to be [50]

$$\Delta x^2 = \frac{1}{p}\int_{-p/2}^{p/2} x'^2 dx' = \frac{p^2}{12} \tag{2.18}$$

with p being the feature size (pixel or strip pitch).

Center of Gravity: Clusters of two or more digis hold position information in the distribution of the charge measurements q_i. Using them as weights for the central positions of the firing channels x_i, a charge-weighted average position is obtained by

$$\bar{x} = \frac{\sum_i q_i x_i}{\sum_i q_i}. \tag{2.19}$$

Two components enter the estimate of the uncertainty: The noise in each signaling channel and the potential miss of charge in either end of the cluster due to the charge threshold. Each channel contributes with an uncertainty of

$$\Delta x_i^2 = \left(\frac{\partial \bar{x}}{\partial q_i}\right)^2 \Delta q_i^2 \tag{2.20}$$

with the derivative

$$\frac{\partial \bar{x}}{\partial q_i} = \frac{(x_i - \bar{x})}{Q}. \tag{2.21}$$

What charge uncertainty is to be taken into account depends on the channel position. Under the assumption of equal noise and a flat distribution of the not detected charge we get

$$\Delta q_i = \begin{cases} \sigma_{\text{Noise}} & \text{for } 1 \le i \le n, \\ Q_{\text{Thr}}/\sqrt{12} & \text{for } i = 0 \text{ and } i = n+1. \end{cases} \tag{2.22}$$

The uncertainty of the center of gravity is then the sum of all contributions:

$$\Delta \bar{x}^2 = \frac{\sigma_{\text{Noise}}^2}{Q^2} \cdot \sum_{i=1}^{n} (x_i - \bar{x})^2 + \frac{Q_{\text{Thr}}^2}{12 \cdot Q^2} \cdot \left[(x_0 - \bar{x})^2 + (x_{n+1} - \bar{x})^2\right]. \tag{2.23}$$

Common numbers in the MVD case yield small cluster sizes ($n \approx 1 \ldots 2$) and a threshold of $5\,\sigma_{\text{Noise}}$, so typically the contribution by the threshold is dominant.

Median: Traveling through the sensor the track produces statistically a flat charge carrier density along its path. A good approximation for the middle of the path is the median of the fired channels (ranging from channel position x_h to x_t)

$$x = \frac{x_h + x_t}{2}. \tag{2.24}$$

Its uncertainty is estimated well with $\Delta x \approx /\sqrt{12}$ as with the binary centeroid.

Head-Tail Algorithm: For clusters with a large number ($n > 3$) of signaling channels in any coordinate, the central channels have more or less the same charge entry. Thus, they do not yield information on the centroid, but add due to the noise to its uncertainty. The reconstructed position in one dimension is calculated from the first and last digi in the cluster. Basically it is the center between the cluster edge positions x_h and x_t, modified by the difference of the edge charges Q_h and Q_t normalized with Q_0:

$$x = \frac{x_h + x_t}{2} + p \cdot \frac{Q_h - Q_t}{2Q_0} \tag{2.25}$$

Ideally Q_0 is the charge the particle leaves in one readout channel determined by the most probable value of the Landau distributed energy loss. However the angle of the particle as well as its momentum are not known, so Q_0 is approximated by the mean charge deposited in the channels between the head and the tail ($n = t - h$):

$$Q_0 = \frac{1}{n-2} \sum_{i=h+1}^{t-1} Q_i \tag{2.26}$$

Uncertainties are sufficiently taken into account by the noise in both edge channels, σ_{Noise}, with the derivatives to the charges:

$$\frac{\partial x}{\partial Q_h} = \frac{-\partial x}{\partial Q_t} = \frac{p}{2Q_0} \tag{2.27}$$

$$\Delta x^2 = 2 \cdot \sigma_{\text{Noise}}^2 \cdot \frac{p^2}{4Q_0^2} \tag{2.28}$$

A valid estimate on Q_0 is required for the Head-Tail algorithm. Thus, it can only be applied to clusters with at least three digis and clusters with two digis have to be reconstructed either with the Center of Gravity or the η-Distribution algorithm. High numbers of digis in a cluster occur rarely in the MVD as it is designed to have almost all particle incident angles smaller than 45°.

η-Distribution: When a cluster is split around its highest charge entry into two halves, called left and right, the centroid can be deduced by the distribution $f(\eta)$ with $\eta = Q_R/(Q_R + Q_L)$. This distribution is characteristic for the sensor structuring, e.g. if each readout channel is connected, if insulating layers are between the metallization features and so forth. It can be measured via the distribution $\frac{\mathrm{d}N}{\mathrm{d}\eta}$ (called "η distribution") of a homogeneously illuminated detector. By integration the distribution $f(\eta)$ is calculated

$$f(\eta) = \frac{1}{N_{\text{tot}}} \int_0^{\eta} \frac{\mathrm{d}N}{\mathrm{d}\eta'} \mathrm{d}\eta' \tag{2.29}$$

and the reconstructed position is then

$$x = x_L + p \cdot f(\eta) \tag{2.30}$$

This algorithm is expected to work best with hits almost perpendicular to the measuring plane, where the clusters are composed of two digis, only.

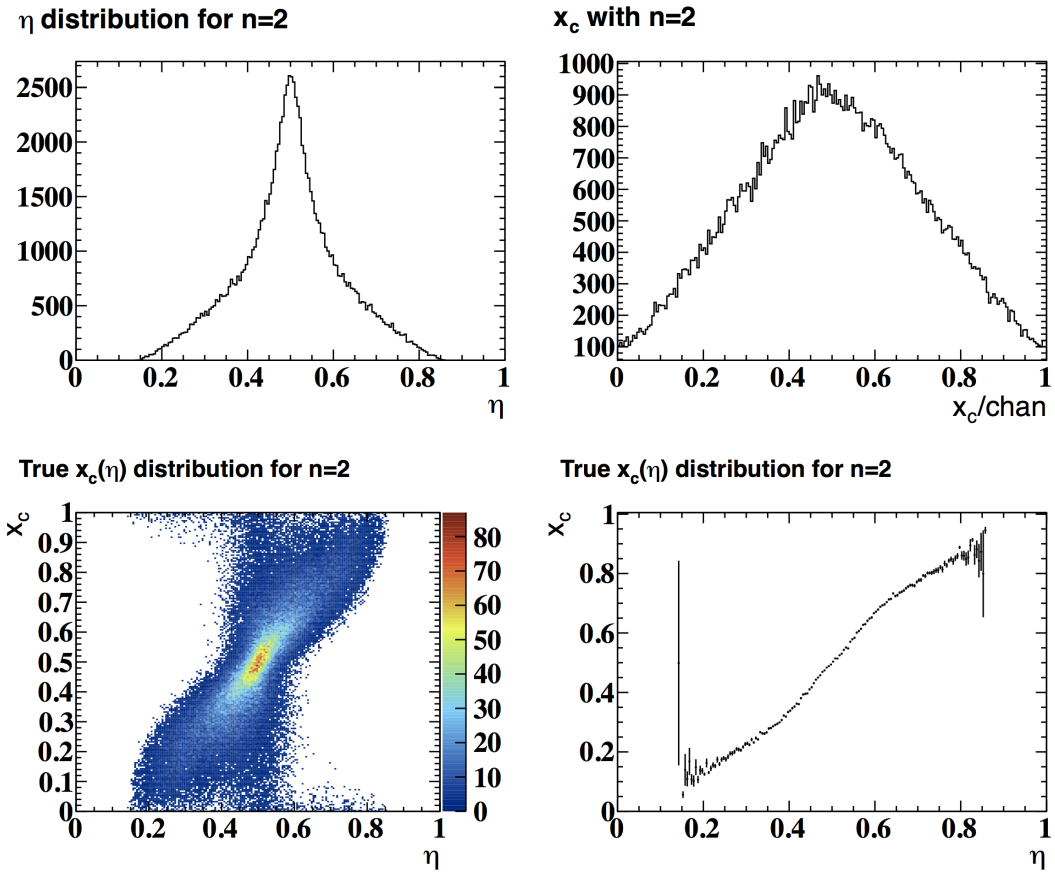

Figure 2.7: Center position (x_c) and η distributions for two-digi clusters and their correlation. (simulation as described in 4.4.1).

One difficulty within this approach is that the full η distribution has to be obtained for each sensor design. However due to the discriminator thresholds suppressing noise hits small charge entries from real hits s are not measured, too. Figure 2.7 shows that parts of the η-distribution are not populated and the distribution of the central coordinate where two-digi clusters are created is not flat for the same reason. Integration of the η-distribution is not trivial under these conditions and the directly by simulations obtained $x_c(\eta)$ dependence is used. Because of the electronic noise each value of η is produced by different center coordinates, the uncertainty is estimated by the width of the x_c distribution in an η bin. The largest width was found to be about 0.1 of the readout feature size.

Strip Charge Correlation

Each strip sensor side delivers a one-dimensional position measurement. With both sides combined, the two-dimensional hit location on the sensor surface can be reconstructed. The centroids define straight lines parallel to the readout strips, so that the

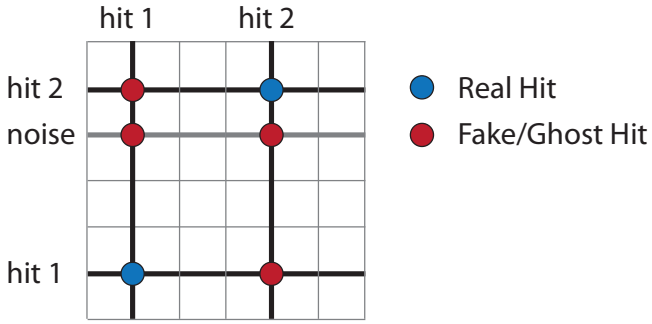

Figure 2.8: Illustration how ghost hits are created in a double sided strip detector by multiple particles as well as by noisy channels.

intersections are the reconstructed hits. More challenging is the case of more than one cluster per sensor side, e.g., when two particles passed the sensor at the same time or a channel gives a fake signal by noise. Simply combining each cluster from the top side with one from the bottom side, as illustrated in figure 2.8, will create ambiguities, called ghost or fake hits.

Reducing the amount of ghost hits while keeping all the true hits is of large importance to the tracklet finding. Each ghost hit imposes the possibility to combine with other hits to spurious track candidates which then would have to be processed by the much slower tracking algorithms. To reduce the number of these ghost hits, the charge measurement in the MVD can be taken into account. With the double-sided readout, one side collects the electrons and the other side the charge holes, leading to a correlation of both signals.

Simple Strip Correlation By requiring the top side and bottom side clusters to yield a similar total charge content ($|Q_{\text{top}} - Q_{\text{bot}}| < Q_{\text{cut}}$), ghost hits can be rejected easily. One exemplary ambiguous cases is when two particles hit a sensor with a similar energy loss (e.g. minimum ionizing particles of the same species), where that method will produce two not distinguishable hit pairs.

Figure 2.9 shows the true and fake hit reconstruction efficiencies as well as the purity in dependence of the charge correlation cut for such a case. The events comprise two electrons of 4 GeV/c each, which both hit one sensor (data from the test station, cf. 4.1). Depending on the rate of such double-hit events Q_{cut} can be chosen by how much fake signal can be tolerated on the overall setup. A common choice for the maximum charge difference is $Q_{\text{cut}} = 5 \cdot \sigma_{\text{Noise}}$. It is to be noted that all combinations are considered and thinned by the cut. This will lead to events with many fake hits, events with rejected true hits, and even with less hits than originally created. In the MVD mostly the strip disks will have double hits.

Likelihood Based Strip Correlation Another approach is to use the knowledge of the hit multiplicity from the number of clusters on one side and making a decision which set of top-bottom cluster combinations matches best. For that a likelihood based method is utilized.

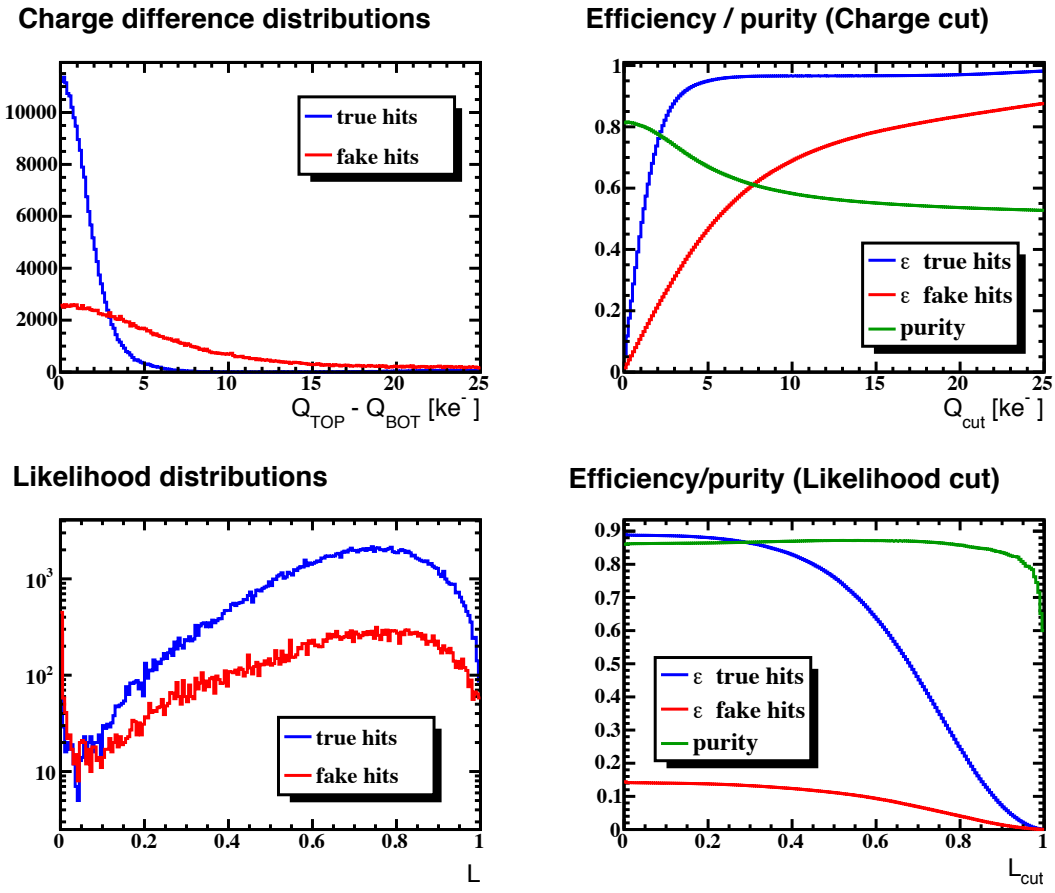

Figure 2.9: Efficiency to reconstruct true and fake hits from double hits of particles with the same energy loss MPV. Both dependence on the top-bottom charge cut Q_{cut} (upper row) and the correlation algorithm likelihood value (lower row) are studied. The left-hand plots show the distributions of the cut variable amongst truly found and fake hits. On the right-hand side the efficiencies and purities are shown depending on the cut value using $\epsilon = N_{\text{i}}/N_{\text{sim}}$ and $P = N_{\text{true}}/(N_{\text{true}} + N_{\text{fake}})$.

Each combination of a top side cluster with a bottom side one is associated with a likelihood based on the charge difference $|Q_{\text{top},i} - Q_{\text{bot},j}|$ and its measurement uncertainty $\Delta Q_{i,j}$. Assuming a Gaussian behavior the probability of the charge difference being compatible with zero is given by the complementary error function:

$$p_{i,j} = \text{erfc}\left(\frac{|Q_{\text{top},i} - Q_{\text{bot},j}|}{\sqrt{2}\cdot\Delta Q_{i,j}}\right). \tag{2.31}$$

The measurement uncertainty of the charge difference is estimated by the top and bottom measurement errors

$$\Delta Q_{i,j} = \sqrt{\Delta Q^2_{\text{top},i} + \Delta Q^2_{\text{bot},j}}. \tag{2.32}$$

Each clusters charge uncertainty is determined as the Gaussian noise in the n_k channels of the cluster and the possibility to loose up to Q_{Thr} in each side of the cluster due to

the discriminator threshold:

$$\Delta Q_{\mathrm{top/bot},k} = \sqrt{n_k \cdot \sigma^2_{\mathrm{Noise}} + 2 \cdot Q^2_{\mathrm{Thr}}} \tag{2.33}$$

with $n_{\mathrm{Thr}} = Q_{\mathrm{Thr}}/\sigma_{\mathrm{Noise}}$ we get

$$\Delta Q_{i,j} = \sqrt{n_i + n_j + 4 \cdot n^2_{\mathrm{Thr}}} \cdot \sigma_{\mathrm{Noise}}. \tag{2.34}$$

Common values for n_{Thr} are three to five and for n_k one to three. It is just to approximate the uncertainty by

$$\Delta Q_{i,j} \approx 2 \cdot Q_{\mathrm{Thr}}, \tag{2.35}$$

which is now equal for all combinations. Correlating top and bottom side clusters in a way that each top cluster is assigned to an unassigned bottom cluster an exclusive set of combinations is formed. The likelihood for a combination set K is calculated as the product of the combination probabilities

$$L_K = \prod_{(i,j)\in K} p_{i,j}. \tag{2.36}$$

The set with the highest likelihood is selected and its combinations form the reconstructed hits.

In the case of an unequal amount of top and bottom clusters there are two hypotheses. First, one strip can be triggered by two particle hits and second electronic noise may have produced a fake signal without a particle hit. These cases are handled at the last stage of the iterative building of the combination sets, when either the top or the bottom side has only one available cluster while the other side has more. Noise hits should be omitted, hence all combinations are produced by ignoring one of the clusters each. The case of degenerate hits is handled by artificially creating r clusters to combine with the r remaining clusters on the other sensor side (denoted by $\tilde{Q}$, δ_{kl} is the Kronecker symbol)

$$Q_1 \to Q'_k = Q_1 - \sum_{l=1}^{r} \tilde{Q}_l(1 - \delta_{kl}) \qquad (k = 1 \ldots r). \tag{2.37}$$

These new charges enter the probability calculation in equation 2.31, that the charge difference becomes for all r remaining combinations

$$|Q_{\mathrm{top},i} - Q_{\mathrm{bot},j}| \to |Q_1 - \sum_{l=1}^{r} \tilde{Q}_l|. \tag{2.38}$$

It is obvious that the amount of combinations grows drastically with the number of clusters involved in the procedure (e.g. 18 combinations for 3+3, 288 for 4+4 and 7200 for 5+5 clusters). In $\overline{\mathsf{P}}\mathsf{ANDA}$ the most prominent cases which will require that algorithm for disambiguation will be "one hit with a noise cluster", "two hits" and "two hits degenerated on one side", thus the number of combinations will be small.

In figure 2.9 it becomes clear that the likelihood value for a certain hit combination has no influence on the achievable purity. Because the algorithm does a decision by assigning all clusters to a whole set of hits, cutting will only decrease the reconstruction efficiency. A true hit reconstruction efficiency of about 0.9 can be achieved with a purity of about 0.85. Because of the considerably large calculation time and the fact that 10 % of the true hits are not reconstructed it might be favorable to use the simplistic charge difference cut and select later on, e.g. during the tracking.

2.4.3 Time Walk Correction

It is possible to correct for the time walk introduced by the time measurement of the ToT method using the measured charge and equation 2.16 from the triangular model. The time walk then is subtracted from the measured time stamp and the resolution is limited by the accuracy of the time stamp measurement as well as the validity of the signal model (see also [49]). To give a few numbers, the time walk t_{W} is for the most probable charge from a minimum ionizing particle in the order of $1/4 \cdot t_{\mathrm{rise}} = 25\,\mathrm{ns}$ and the digitization bin width for the 150 MHz $\overline{\mathsf{P}}$ANDA clock is 6.7 ns.

2.4.4 Tracklet Reconstruction

The MVD is designed to provide four hit points per particle trajectory in most of its angular coverage. This enables a standalone tracklet finding which can start immediately after the hit reconstruction without waiting for other detectors to finish their reconstruction. Fast information on the event shape, such as the multiplicity of charged particles, as well as vital seeding information, measured sharply in time, for the global tracking are provided. It is even possible to get early vertex estimates enabling a fast vertex selection for delayed (e.g. D meson) decays.

One approach is to project the x-y part of the hit coordinates on a Riemann surface (here a paraboloid [51]) and fit a plane to them (cf. 1.5.6). From each set of three hits tracklets are created and extended with other suitable hits and the best matching combinations are chosen. In the l-z view (l is the arc length) a straight line fit verifies then if the hit combinations belong to one track. Due to the magnetic field strength and the involved energies, trajectory radii are large in comparison to the size of the MVD. It is expected that the momentum resolution is fairly poor, compared to the full tracking, as well as the vertex estimates taken with these tracklets. However, the time measurement and the track finding will aid the event deconvolution, which is the biggest issue with the slower detector components.

2.5 Parameter Handling

One feature of the framework is its centrally managed runtime parameter database (RTDB, see 1.5.2) which can connect to several database formats (ASCII or ROOT files, later also `TSql` type databases etc.). Switching the parameter source does not require recompilation of the code. In the SDS package the parameter classes read and store the geometry, the volume name mapping and the detector specific parameters

Parameter	Type	Unit	Description
dimX	`Double_t`	[cm]	Size of pixel cell
dimY	`Double_t`	[cm]	Size of pixel cell
threshold	`Double_t`	$[e^-]$	Minimum charge threshold
noise	`Double_t`	$[e^-]$	Electronic noise σ_{Noise}
QCloudSigma	`Double_t`	[cm]	Charge cloud σ_{cloud}
FECols	`Int_t`		Number of pixel columns per front-end
FERows	`Int_t`		Number of pixel rows per front-end
ClustRad	`Double_t`	[pixels]	Cluster finding radius
fe_BusClock	`Double_t`	[MHz]	Bus clock frequency
chargeconv_method	`Int_t`		Charge conversion model selection

Table 2.2: Pixel Sensor Parameters

Parameter	Type	Unit	Description
top_pitch	`Double_t`	[cm]	Top side strip readout pitch
bot_pitch	`Double_t`	[cm]	Bottom side strip readout pitch
orient	`Double_t`	[rad]	Top side strip orientation angle
skew	`Double_t`	[rad]	Skew angle (top vs. bottom side)
top_anchor_x	`Double_t`	[cm]	Top side reference point (x)
top_anchor_y	`Double_t`	[cm]	Top side reference point (y)
bot_anchor_x	`Double_t`	[cm]	Bottom side reference point (x)
bot_anchor_y	`Double_t`	[cm]	Bottom side reference point (y)
nr_fe_channels	`Int_t`		Number of channels per front-end
nr_fe_top	`Int_t`		Number of front-ends on top side
nr_fe_bottom	`Int_t`		Number of front-ends on bottom side
charge_threshold	`Double_t`	$[e^-]$	Minimum charge threshold
charge_noise	`Double_t`	$[e^-]$	Electronic noise σ_{Noise}
QCloudSigma	`Double_t`	[cm]	Charge cloud σ_{cloud}
sens_Type	`Text_t`		Sensor type identification string
fe_Type	`Text_t`		Front-end type name
fe_BusClock	`Double_t`	[MHz]	Bus clock frequency (noise rate)
cluster_mod	`Int_t`		Cluster finding mode selection
cluster_mean	`Int_t`		Centroid calculation method selection
cluster_radchan	`Int_t`	[strips]	Cluster finding radius
cluster_radtime	`Int_t`	[ns]	Cluster finding time window (not used)
cluster_corrchargecut	`Double_t`	$[e^-]$	Charge top-bottom correlation cut
cluster_singlechargecut	`Double_t`	$[e^-]$	Threshold for single hit clusters
chargeconv_method	`Int_t`		Charge conversion model selection

Table 2.3: Strip Sensor Parameters

(see tables 2.2 and 2.3) through the common RTDB interfaces. Geometry alignment corrections will be applied directly to the geometry stored with the parameters.

Volume identification is done with string identifiers, showing the assembly hierarchy of the volumes. Storing the whole string in each data entry would introduce a high demand on data load. Therefore a mapping between each string identifier and a unique integer number is introduced with the `PndGeoHandling` class. The mapping table is stored in the RTDB, while the class also provides an easy way of accessing the volumes with that id. Additionally the direct transformation of 3D points between the laboratory frame and the sensor's local frame is provided for easy access.

Chapter 3

Vertex Reconstruction

Finding vertices in the $\overline{\mathsf{P}}$ANDA experiment is the central goal of the MVD, especially from short-lived decays close to the interaction point. A particle decay at one point in space, the decay vertex, produces two or more particles traveling further through the detector. Measuring these trajectories yields deviations from the original track paths due to the measurement uncertainties and material effects. Furthermore, the starting points of the measured trajectories cannot be defined and are situated somewhere along the trajectory back-extrapolation from the first hit. Using two or more measured trajectories it is possible to find a common point, under the assumption that these tracks originate from the same point in space, i.e., from the same decaying particle. Figure 3.1 illustrates the situation with the measured track properties $\mathbf{q}_i$ and the extrapolation to a common vertex $\vec{V}$. At this point, tangent to the trajectories, the momentum three-vectors $\vec{p}_i$ of the emerging particles are defined, especially their direction.

This chapter describes the two vertex reconstruction tools implemented within this work and as well sketches shortly the preliminary vertex constrained kinematic fitter, which is also available in the PandaRoot software.

3.1 Point of Closest Approach Finder

Finding a vertex by pure geometrical considerations is the search for the point of closest approach (POCA) of the particle trajectories. In the case of helical trajectories, such as the ones measured in a solenoidal magnetic field, this has to be done either by iteration going along the trajectories and searching the minimal distance or one has to introduce simplifications to the trajectory description. Iterative approaches are usually computing-intensive, hence this approach favors a simplified analytical approach. For tracks coming from the same vertex the POCA will result in a minimum distance between the tracks in all three coordinates. This is not true when the tracks do not originate from the same point. To find the POCA it is enough to find it in a 2D projection and the third coordinate, restricted by the trajectories, will be very close to the POCA in three dimensions.

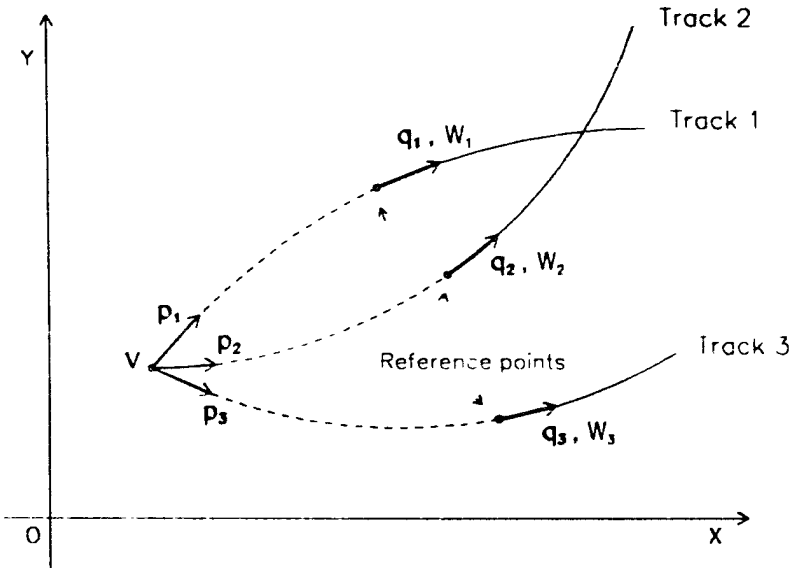

Figure 3.1: Illustration of the trajectory measurements $\mathbf{q}_i$ in any representation (with the covariance $\hat{\mathbf{C}}_i = \mathbf{W}_i$) defined at their reference points and the extrapolation to the vertex $\vec{V}$ and the particle momenta $\vec{p}_i$ (picture taken from [52]).

3.1.1 Two Tracks

Considering two charged particles in a homogeneous field along the z axis, the natural choice of the projection is in the x-y-plane where the trajectories form two circles. These circles' POCA can be calculated analytically. A reduced coordinate system is used, originating in the first circle center, its t-axis pointing to the second circle center at $t_{c_2} = d$ while the s-axis is perpendicular (see figure 3.2). The circles are then expressed as

$$r_1^2 = t^2 + s^2 \qquad\qquad r_2^2 = (t-d)^2 + s^2. \tag{3.1}$$

As shown in figure 3.2 two cases can be distinguished, intersecting and not intersecting circles. The solution to the intersecting circles is

$$t = \frac{d}{2} + \frac{r_1^2 - r_2^2}{2d} \qquad\qquad s^2 = r_1^2 - t^2. \tag{3.2}$$

To choose one of the two solutions for s, the track distances in the z coordinate are taken into account:

$$z = \left(x^2 + y^2\right) \cdot \cos(\theta) \tag{3.3}$$

The solution with the smaller distance in the z coordinate is favored.

For not intersecting circles we use the center between the circle trajectories along the segment connecting the two circle centers

$$t = r_1 + \frac{1}{2}\left(d - r_1 - r_2\right) = \frac{1}{2}\left(d + r_1 - r_2\right) \qquad\qquad s = 0 \tag{3.4}$$

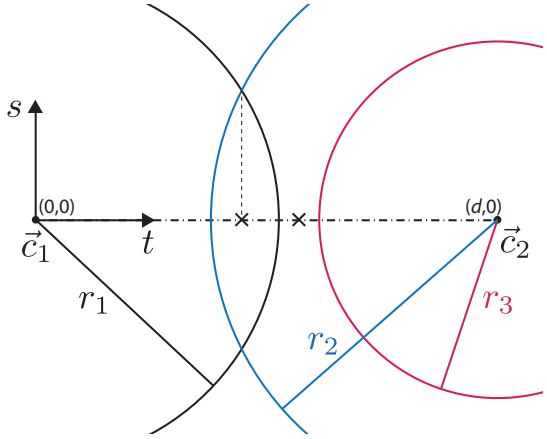

Figure 3.2: Illustration of the POCA finding method and its two cases. The solution for the t coordinate of the black circle with the red and blue circles, respectively, is indicated by the crosses.

A measure of the POCA's quality and thus for the validity of the assumption that the two tracks originate form the same vertex is the distance

$$D = \sqrt{(d - r_1 - r_2)^2 + (z_1 - z_2)^2} \tag{3.5}$$

between the points of closest approach on the two trajectories.

3.1.2 Multiple Tracks

For decayed particles with more than two outgoing tracks, it is beneficial to take all available information into account. Simplifying the problem of finding one common point at once, the POCAs of each pair of tracks are calculated, and then averaged with the inverse minimum distances $D_{i,j}^{-1}$ (see equation 3.5) as weight factors. For n tracks the vertex $\vec{V}$ is determined as:

$$\vec{V} = \frac{\sum_{i=0,j=i+1}^{n} D_{i,j}^{-1} \vec{V_{i,j}}}{\sum_{i=0,j=i+1}^{n} D_{i,j}^{-1}} \tag{3.6}$$

Qualifying how good the tracks match to one vertex is important to reject outliers or false combinations. The track distance is a good measure for two tracks. However, in the case of more than two tracks such a quality value is calculated by inverting the sum of the averaging weights

$$\tilde{D} = \left(\sum_{i=0,j=i+1}^{n} D_{i,j}^{-1} \right)^{-1} . \tag{3.7}$$

Note that $\tilde{D}$ becomes the tracks geometric distance from equation 3.5 in the case of two tracks.

Although this treatment is done in the two-dimensional projection and does not take the measurement uncertainties into account, it produces a surprisingly good vertex estimate (cf. section 4.5). Because this approach is analytical and requires only the measurements without the covariances, it is a promising candidate for an online vertex selection algorithm implemented in a hardware setup.

3.2 Vertex Fitting

Estimating the vertex position by fitting to measurements is usually done with the χ^2 method. In general this also comprises the update of the track momentum measurements at the estimated vertex. Measurement covariances are taken into account and the estimator's covariances are returned. A comprehensive literature on practical fitting can be found in the Paul Avery write-ups pt. 1-4 [53, 54, 55, 56], which cover examples from particle physics.

3.2.1 χ^2 Method

To get the best values for a set of variables $\eta = (\eta_1 \dots \eta_m)^\mathsf{T}$ with a measurement of the observables $\xi = (\xi_1 \dots \xi_n)^\mathsf{T}$, with $(n \geq m)$, one can use the χ^2 fitting method. Knowing the measurement covariance matrix $\hat{\mathbf{C}}_\xi = \mathtt{cov}(\xi, \xi)$ and the functional dependence $\xi = \mathcal{F}(\eta)$, the χ^2 value is calculated by

$$\chi^2 = (\xi - \mathcal{F}(\eta))^\mathsf{T} \hat{\mathbf{C}}_\xi^{-1} (\xi - \mathcal{F}(\eta)) \,. \tag{3.8}$$

This value is a measure for how well measurement and fitted value suit each other. The best value is found by the minimum of χ^2, satisfied by the requirements (m equations)

$$\frac{\partial \chi^2}{\partial \eta} = 0. \tag{3.9}$$

Usually these equations have to be linearized because of the complicated shape of the functions $\mathcal{F}(\eta)$. When these functions are linear within the measurement errors around the initial guess (seed value) η^0, one can write

$$\begin{aligned} \mathcal{F}(\eta) \approx \mathcal{F}(\eta^0) \quad &+ \left.\frac{\partial \mathcal{F}(\eta)}{\partial \eta}\right|_{\eta^0} \cdot (\eta - \eta^0) \\ \equiv \xi^0 \qquad &+ \hat{\mathbf{J}} \cdot (\eta - \eta^0). \end{aligned} \tag{3.10}$$

Here $\hat{\mathbf{J}}$ is the Jacobian at the initial guess. Inserting the linearized functions into the χ^2 expression one obtains

$$\chi^2 = \left(\xi - \xi^0 - \hat{\mathbf{J}} \cdot (\eta - \eta^0)\right)^\mathsf{T} \hat{\mathbf{C}}_\xi^{-1} \left(\xi - \xi^0 - \hat{\mathbf{J}} \cdot (\eta - \eta^0)\right) \tag{3.11}$$

which yields for the partial derivatives (equation 3.9):

$$0 = 2 \cdot \hat{\mathbf{J}}^\mathsf{T} \hat{\mathbf{C}}_\xi^{-1} \left(\xi - \xi^0 - \hat{\mathbf{J}} \cdot (\eta - \eta^0)\right). \tag{3.12}$$

Then the solution and its covariance matrix are

$$\eta = \eta^0 + \hat{\mathbf{C}}_\eta^{-1}\hat{\mathbf{J}}^\mathsf{T}\hat{\mathbf{C}}_\xi^{-1}(\xi - \xi^0) \tag{3.13}$$

$$\hat{\mathbf{C}}_\eta = \hat{\mathbf{J}}^\mathsf{T}\hat{\mathbf{C}}_\xi^{-1}\hat{\mathbf{J}} \tag{3.14}$$

Knowing the matrix of derivatives $\hat{\mathbf{J}}$ and having the measurement ξ and $\hat{\mathbf{C}}_\xi$, the fit result only depends on the seed value η^0. By updating the seed value to the fit's outcome $\eta^0_{(2)} = \eta_{(1)}$, the fit can iteratively converge to an optimal result with a minimal χ^2. Provided that the initial guess of the seed value was not too far away from the optimal fit only a few iterations are necessary to drop the fit's updates below the measurement uncertainties.

3.2.2 χ^2 Vertex Fit

The initial situation is a set of n particle tracks, with the hypothesis to come from one common space point $\vec{V}$, e.g., from a heavier particle's decay. In a magnetic field tracks are not straight lines. The momentum three-vector $\vec{p}_i$ orientation, being tangent to the trajectory of particle i, depends on the position where it is defined. In a solenoidal field the trajectory i is described as a helix, usually defined by five track parameters $\mathbf{q}_i$, which can be expressed as functions of the vertex and momentum to be fit. For a system of n tracks the vectors η and $\xi = \mathcal{F}(\eta)$ are defined:

$$\xi = \begin{pmatrix} \mathbf{q}_1 \\ \mathbf{q}_2 \\ \vdots \\ \mathbf{q}_n \end{pmatrix} = \begin{pmatrix} \mathbf{F}_1(\vec{V}, \vec{p}_1) \\ \mathbf{F}_2(\vec{V}, \vec{p}_2) \\ \vdots \\ \mathbf{F}_n(\vec{V}, \vec{p}_n) \end{pmatrix} = \mathcal{F}(\eta), \quad \eta = \begin{pmatrix} \vec{V} \\ \vec{p}_1 \\ \vec{p}_2 \\ \vdots \\ \vec{p}_n \end{pmatrix} \tag{3.15}$$

The matrix of $\hat{\mathbf{J}}$, present in the linearization (equation 3.10), is then expressed as derivatives of the n parameter functions $\mathbf{F}_i(\vec{V}, \vec{p}_i)$:

$$\hat{\mathbf{J}} = \begin{pmatrix} \frac{\partial \mathbf{F}_1(\vec{V},\vec{p}_1)}{\partial \vec{V}} & \frac{\partial \mathbf{F}_1(\vec{V},\vec{p}_1)}{\partial \vec{p}_1} & 0 & \cdots & 0 \\ \frac{\partial \mathbf{F}_2(\vec{V},\vec{p}_2)}{\partial \vec{V}} & 0 & \frac{\partial \mathbf{F}_2(\vec{V},\vec{p}_2)}{\partial \vec{p}_2} & \cdots & 0 \\ \vdots & \vdots & \vdots & \ddots & \vdots \\ \frac{\partial \mathbf{F}_n(\vec{V},\vec{p}_n)}{\partial \vec{V}} & 0 & 0 & \cdots & \frac{\partial \mathbf{F}_n(\vec{V},\vec{p}_n)}{\partial \vec{p}_n} \end{pmatrix}_{(\vec{V}^0, \vec{p}_1^{\,0}, \ldots, \vec{p}_n^{\,0})} . \tag{3.16}$$

It is to be noted that the vector ξ is of the dimension $5n$ while η is the size of $(3 + 3n)$. Hence, the matrix $\hat{\mathbf{J}}$ has the dimension of $(3 + 3n) \times 5n$. Solving the problem without further optimizations, the inversion of one $5n \times 5n$-matrix and one $(3 + 3n) \times (3 + 3n)$-matrix is required, as well as multiplications of large matrices, scaling with n, the number of tracks. Scaling matrix sizes with the number of tracks is quite costly in terms of computing time.

Such a description does a priori neglect energy loss and multiple scattering. The starting values of the particle momenta and vertex are assumed to be close enough to the solution to minimize these effects. For example, fitting to the primary vertex

is done inside the beam pipe vacuum, as many secondary decays will be, too. For other cases it might be beneficial, before performing the vertex fit, to use the track propagation engine, used during the track fitting (e.g. GEANE), to recalculate the helix properties close to a vertex seed value, which can be obtained from another algorithm, e.g. by the POCA finder (cf. section 3.1).

3.3 Fast Vertex Fitter

This fitter is an implementation of Billoir's method [52], used in several experiments. Simplifications are introduced in the formation of χ^2, in the number of varying observables and in the track propagation. Its goal is to provide a fast running algorithm which compromises on accuracy. A full fit of vertex and track momenta as well as a fast fit algorithm on the vertex position only are implemented in PandaRoot.

3.3.1 Fast Linearization

Under the assumption of independent track measurements and with one track parametrization $\mathbf{F}(\vec{V},\vec{p})$, the χ^2 can be expressed as a sum over the n tracks:

$$\chi^2 = \sum_i \left(\mathbf{q}_i - \mathbf{F}(\vec{V},\vec{p}_i)\right)^{\mathsf{T}} \hat{\mathbf{C}}_i^{-1} \left(\mathbf{q}_i - \mathbf{F}(\vec{V},\vec{p}_i)\right), \tag{3.17}$$

with the track parameters $\mathbf{q}_i$ and covariance matrices $\hat{\mathbf{C}}_i$ of the individual track measurements. The dimension of the matrix multiplications is reduced from $5n$ to 5. Linearizing each element $\mathbf{F}(\vec{V},\vec{p}_i)$ in the sum,

$$\mathbf{F}(\vec{V}^0 + \delta\vec{V}, \vec{p}_i^{\,0} + \delta\vec{p}_i) \approx \vec{q}_i^{\,0} + \hat{\mathbf{D}}_i\delta\vec{V} + \hat{\mathbf{E}}_i\delta\vec{p}_i, \tag{3.18}$$

a set of (3×5)-matrices of derivatives is obtained.

$$\hat{\mathbf{D}}_i = \left.\frac{\partial\mathbf{F}(\vec{V},\vec{p}_i)}{\partial\vec{V}}\right|_{\vec{V}^0,\vec{p}_1^{\,0},\ldots,\vec{p}_n^{\,0}}, \qquad \hat{\mathbf{E}}_i = \left.\frac{\partial\mathbf{F}(\vec{V},\vec{p}_i)}{\partial\vec{p}_i}\right|_{\vec{V}^0,\vec{p}_1^{\,0},\ldots,\vec{p}_n^{\,0}} \tag{3.19}$$

Minimizing χ^2 with respect to each variable $\vec{V}$ and $\vec{p}_i$ a set of $n+1$ equations is derived in the form of:

$$\hat{\mathbf{A}}\delta\vec{V} + \sum_i \hat{\mathbf{B}}_i\delta\vec{p}_i = \hat{\mathbf{T}} \tag{3.20}$$

$$\hat{\mathbf{B}}_i^{\mathsf{T}}\delta\vec{V} + \hat{\mathbf{G}}_i\delta\vec{p}_i = \hat{\mathbf{U}}_i \tag{3.21}$$

by introducing some auxiliary matrices

$$\begin{aligned} \hat{\mathbf{A}} &= \sum_i \hat{\mathbf{D}}_i^{\mathsf{T}}\hat{\mathbf{C}}_i^{-1}\hat{\mathbf{D}}_i\,, \quad \hat{\mathbf{B}}_i = \hat{\mathbf{D}}_i^{\mathsf{T}}\hat{\mathbf{C}}_i^{-1}\hat{\mathbf{E}}_i\,, \quad \hat{\mathbf{G}}_i = \hat{\mathbf{E}}_i^{\mathsf{T}}\hat{\mathbf{C}}_i^{-1}\hat{\mathbf{E}}_i\,, \\ \hat{\mathbf{T}} &= \sum_i \hat{\mathbf{D}}_i^{\mathsf{T}}\hat{\mathbf{C}}_i^{-1}\delta\mathbf{q}_i\,, \quad \hat{\mathbf{U}}_i = \hat{\mathbf{E}}_i^{\mathsf{T}}\hat{\mathbf{C}}_i^{-1}\delta\mathbf{q}_i \end{aligned} \tag{3.22}$$

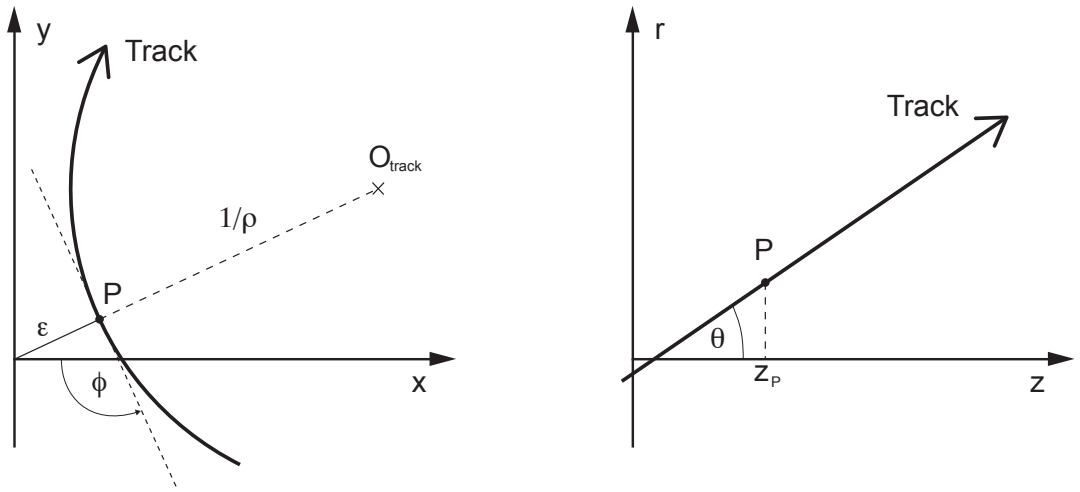

Figure 3.3: Perigee parametrization $(\epsilon, z_{\mathrm{p}}, \theta, \phi_{\mathrm{p}}, \rho)$: P is the track's point of closest approach to the z axis, ρ the track curvature, ϵ the distance to the z axis and ϕ the tangent's angle of the trajectory in P.

the solution for the vertex fit can be derived from equations 3.20 and 3.21 (see also [52]) is then expressed as

$$\delta\vec{V} = \left(\hat{\mathbf{A}} - \sum_i \hat{\mathbf{B}}_i \hat{\mathbf{G}}_i^{-1} \hat{\mathbf{B}}_i^{\mathsf{T}}\right)^{-1} \left(\hat{\mathbf{T}} - \sum_i \hat{\mathbf{B}}_i \hat{\mathbf{G}}_i^{-1} \hat{\mathbf{U}}_i\right) \tag{3.23}$$

$$\delta\vec{p}_i = \hat{\mathbf{G}}_i^{-1} \left(\hat{\mathbf{U}}_i - \hat{\mathbf{B}}_i^{\mathsf{T}} \delta\vec{V}\right). \tag{3.24}$$

The covariances are obtained from the same auxiliary matrices and the solution:

$$\hat{\mathbf{C}}_{\vec{V},\vec{V}} = \hat{\mathbf{A}} - \sum_i \hat{\mathbf{B}}_i \hat{\mathbf{G}}_i^{-1} \hat{\mathbf{B}}_i^{\mathsf{T}} \tag{3.25}$$

$$\hat{\mathbf{C}}_{\vec{V},\vec{p}_i} = -\hat{\mathbf{C}}_{\vec{V},\vec{V}} \hat{\mathbf{B}}_i \hat{\mathbf{G}}_i \tag{3.26}$$

$$\hat{\mathbf{C}}_{\vec{p}_i,\vec{V}} = \hat{\mathbf{C}}_{\vec{V},\vec{p}_i}^{\mathsf{T}} \tag{3.27}$$

$$\hat{\mathbf{C}}_{\vec{p}_i,\vec{p}_j} = \hat{\mathbf{G}}_i^{-1} \left(\delta_{ij} - \hat{\mathbf{B}}_i^{\mathsf{T}} \hat{\mathbf{C}}_{\vec{V},\vec{p}_j}\right). \tag{3.28}$$

Inserting the n solutions $\mathbf{F}(\vec{V}^0 + \delta\vec{V}, \vec{p}_i^{\,0} + \delta\vec{p}_i)$ back into equations 3.18 and 3.17 the χ^2 value is obtained. It is a measure of the fit result's quality and how well the tracks match the common vertex hypothesis.

3.3.2 Fast Propagation

So far the fast fit procedure is laid down. However the choice of the coordinate system is needed, i.e. the form of $\mathbf{F}(\vec{V}, \vec{p})$ and thus the matrices of derivatives $\hat{\mathbf{D}}$ and $\hat{\mathbf{E}}$

As track parametrization the "perigee" description for helices is chosen. The perigee point P on the trajectory is identified being the closest to the z axis. There a

helix can be fully described by a vector of five parameters $\mathbf{q}_i = (\epsilon, z_\mathrm{p}, \theta, \phi_\mathrm{p}, \rho)$. These are defined as (see also figure 3.3):

ϵ	–	signed distance of the perigee point to the z axis
z_p	–	z position of the perigee point
θ	–	polar angle of the particle momentum
ϕ_p	–	azimutal angle of the particle momentum at the perigee point
ρ	–	circular curvature in the x–y plane, radius $R_\mathrm{c} = 1/\lvert\rho\rvert$

The sign of ϵ is positive if the origin is on the left-hand side of the trajectory, while ρ is positive for anti-clockwise trajectories in the x–y projection. When going along the trajectory the helix is still described with the same kind of parameters. It is notable that ρ and θ remain constant, while ϵ', ϕ' and z' change their values together with the anchor point of the helix' definition. Approximating the helix around the perigee point P with a running parameter $L \ll 1/|\rho|$, one obtains

$$\begin{aligned} x &\approx L\cos\phi_\mathrm{p} &&+\left(\epsilon - \frac{L^2\rho}{2}\right)\sin\phi_\mathrm{p} \\ y &\approx L\sin\phi_\mathrm{p} &&-\left(\epsilon - \frac{L^2\rho}{2}\right)\cos\phi_\mathrm{p} \\ z &\approx L\cot\theta &&+ z_\mathrm{p}. \end{aligned} \tag{3.29}$$

Going from the vertex to the perigee point one can express the perigee parameters with the vertex coordinates (in first order of ρ).

$$\begin{aligned} \epsilon &= -R - Q^2\rho/2 \\ z_\mathrm{p} &= z_\mathrm{v} - Q(1 - R\rho)\cot\theta \\ \phi_\mathrm{p} &= \phi_\mathrm{v} - Q\rho \end{aligned} \tag{3.30}$$

with

$$\begin{aligned} s = \sin\phi_\mathrm{v},\ c = \cos\phi_\mathrm{v},\ t = \cot\theta \\ Q = x_\mathrm{v}c + y_\mathrm{v}s,\ R = y_\mathrm{v}c - x_\mathrm{v}s \end{aligned} \tag{3.31}$$

With two of the track parameters being unaffected by the vertex fit, the whole problem is now reduced to three dimensional matrices, the derivatives as well. These, to be pasted in the fit solution (equations 3.22–3.28), read explicitly:

$$\begin{aligned} \hat{\mathbf{D}} &= \begin{pmatrix} \partial\epsilon/\partial x_\mathrm{v} & \partial\epsilon/\partial y_\mathrm{v} & \partial\epsilon/\partial z_\mathrm{v} \\ \partial z_\mathrm{p}/\partial x_\mathrm{v} & \partial z_\mathrm{p}/\partial y_\mathrm{v} & \partial z_\mathrm{p}/\partial z_\mathrm{v} \\ \partial\phi_\mathrm{p}/\partial x_\mathrm{v} & \partial\phi_\mathrm{p}/\partial y_\mathrm{v} & \partial\phi_\mathrm{p}/\partial z_\mathrm{v} \end{pmatrix} = \begin{pmatrix} s & -c & 0 \\ -tc & -ts & 1 \\ -\rho c & -\rho s & 0 \end{pmatrix} \\ \hat{\mathbf{E}} &= \begin{pmatrix} \partial\epsilon/\partial\theta & \partial\epsilon/\partial\phi_\mathrm{v} & \partial\epsilon/\partial\rho \\ \partial z_\mathrm{p}/\partial\theta & \partial z_\mathrm{p}/\partial\phi_\mathrm{v} & \partial z_\mathrm{p}/\partial\rho \\ \partial\phi_\mathrm{p}/\partial\theta & \partial\phi_\mathrm{p}/\partial\phi_\mathrm{v} & \partial\phi_\mathrm{p}/\partial\rho \end{pmatrix} = \begin{pmatrix} 0 & Q & -Q^2/2 \\ Q(1+t^2) & -Rt & QRt \\ 0 & 1 & -Q \end{pmatrix} \end{aligned} \tag{3.32}$$

The separation of the χ^2 into a sum over the tracks, the reduction to the three trying track parameters and the approximation of the propagation are introduced to gain in computing speed, especially for sets of many tracks. The matrix dimensions are reduced from $5n \times 5n$ to 3×3 matrices.

$\overline{\text{P}}$ANDA Application

In the equations above each particle momentum was represented by the polar and azimutal angles (θ,ϕ) as well as the signed curvature ρ. However, particles in the PandaRoot analysis stage are described with the cartesian components of the momentum together with the associated covariance matrix. Transforming the particle description from $(x_\mathrm{p}, y_\mathrm{p}, z_\mathrm{p}, p_x, p_y, p_z)$ to the perigee description $(\epsilon, z_0, \theta, \phi_0, \rho)$, the covariance matrix has to be transformed accordingly which is done by

$$\hat{\mathbf{C}}_\mathrm{PRG} = \hat{\mathbf{J}}\hat{\mathbf{C}}_{\vec{x},\vec{p}}\hat{\mathbf{J}}^\mathrm{T} \tag{3.33}$$

with the Jacobian for that transformation

$$\hat{\mathbf{J}} = \begin{pmatrix} \frac{q\cdot x_\mathrm{c}}{R_\mathrm{c}} & \frac{q\cdot y_\mathrm{c}}{R_\mathrm{c}} & 0 & \frac{q\cdot y_\mathrm{c}}{R_\mathrm{c}\cdot qBc} - \frac{\rho}{|\rho|}\frac{q\cdot p_x}{p_t\cdot qBc} & \frac{-q\cdot x_\mathrm{c}}{R_\mathrm{c}\cdot qBc} - \frac{\rho}{|\rho|}\frac{q\cdot p_y}{p_t\cdot qBc} & 0 \\ \frac{-y_\mathrm{c}\cdot p_z}{R_\mathrm{c}^2\cdot qBc} & \frac{x_\mathrm{c}\cdot p_z}{R_\mathrm{c}^2\cdot qBc} & 1 & \frac{p_z}{qBc}\left(\frac{p_y}{p_t^2} + \frac{x_\mathrm{c}}{R_\mathrm{c}^2\cdot qBc}\right) & \frac{-p_z}{qBc}\left(\frac{p_x}{p_t^2} - \frac{y_\mathrm{c}}{R_\mathrm{c}^2\cdot qBc}\right) & \frac{\phi_0-\phi_\mathrm{p}}{qBc} \\ 0 & 0 & 0 & \frac{p_x\cdot p_z}{p_t^3} & \frac{p_y\cdot p_z}{p_t^3} & \frac{-1}{p_t^3} \\ \frac{-y_\mathrm{c}}{R_\mathrm{c}^2} & \frac{x_\mathrm{c}}{R_\mathrm{c}^2} & 0 & \frac{x_\mathrm{c}}{R_\mathrm{c}^2\cdot qBc} & \frac{y_\mathrm{c}}{R_\mathrm{c}^2\cdot qBc} & 0 \\ 0 & 0 & 0 & \frac{-\rho\cdot p_x}{p_t^2} & \frac{-\rho\cdot p_y}{p_t^2} & 0 \end{pmatrix} \tag{3.34}$$

$$x_\mathrm{c} = x_\mathrm{p} - p_y/qBc \quad y_\mathrm{c} = y_\mathrm{p} + p_x/qBc$$

$$R_\mathrm{c} = \sqrt{x_\mathrm{c}^2 = y_\mathrm{c}^2} \qquad p_t = \sqrt{p_x^2 + p_y^2}$$

(q: Charge, B: Magnetic field, c: speed of light, ϕ_p: momentum azimutal angle) Because that transformation of the covariance matrix has to be performed the matrices of derivatives $\hat{\mathbf{D}}_i$ and $\hat{\mathbf{E}}_i$ are available right away by that Jacobian. It is now only a small step to extend the dimensions used in the fit to the full set of five helix parameters with $\hat{\mathbf{J}}_i = (\hat{\mathbf{D}}_i, \hat{\mathbf{E}}_i)$. Although one of the original arguments was to reduce the parameter dimensions in order to gain speed, the track multiplicities in $\overline{\text{P}}$ANDA events are comparably low with two to four tracks per vertex fit that more precision is preferable in this case.

3.3.3 Fast Vertex Position Fit

Often it is enough to estimate the vertex position without optimizing other variables. Especially for vertex position based selection criteria, such as the distance to the primary interaction point or the distance between two decays, a fast calculation of the vertex, omitting heavier calculations, should be favored. In order to simplify the expression in equation 3.17, the set of parameters $\mathbf{q}_i$ is reduced to (ϵ, z_p), while the measurement uncertainty on the tracks momenta, i.e. to (θ, ϕ, ρ), is neglected in the vicinity of the perigee point.

The linearization (equation 3.18) then yields only $\hat{\mathbf{D}}'$, the 3×2 submatrix of $\hat{\mathbf{D}}$. It is then found that the perigee point can be expressed as $\vec{x}_{\mathrm{p}i} = \hat{\mathbf{D}}_i'^{-1}\mathbf{q}_i'$,which enables us to rewrite χ^2 in the laboratory frame:

$$\chi^2 = \sum_i \left(\left(\vec{x}_{\mathrm{p}i} - \vec{V}\right)^\mathsf{T} \hat{\mathbf{D}}_i'^\mathsf{T} \hat{\mathbf{C}}_i^{-1} \hat{\mathbf{D}}_i' \left(\vec{x}_{\mathrm{p}i} - \vec{V}\right)\right) \tag{3.35}$$

under the assumption that the vertex seed is the origin ($\vec{V}^0 = \vec{0}$). This condition is convenient and can be always achieved by moving the origin to $\vec{V}^0$ before calculating the track parameters $\mathbf{q}_i$. Now, abbreviating with $\hat{\mathbf{w}}_i = \hat{\mathbf{D}}_i'^{\mathsf{T}} \hat{\mathbf{C}}_i^{-1} \hat{\mathbf{D}}_i'$, the solution for the vertex position and its covariance are:

$$\vec{V} = \left(\sum_i \hat{\mathbf{w}}_i \right)^{-1} \left(\sum_i \hat{\mathbf{w}}_i \vec{x}_{\mathrm{p}i} \right) \tag{3.36}$$

$$\hat{\mathbf{C}}_{\vec{V},\vec{V}} = \left(\sum_i \hat{\mathbf{w}}_i \right)^{-1} . \tag{3.37}$$

Here, the low dimensions of the matrices and the small number of matrix operations are expected to result in an efficient algorithm to be utilized in an online selection chain.

In contrast to the POCA finding (section 3.1), which is also a fast method, this fitter takes the measurement covariances into account and returns the covariance of the newly found vertex. As fit quality the χ^2 is available as well as each track's contribution to it. That allows for a fast rejection of not matching tracks, without being too stringent on tracks with a relatively large measurement error (e.g. forward track's z coordinates). Its outcome is used in the full fit described earlier as initial guess and helps to reduce the number of iterations with heavier calculations.

3.4 Vertex Constrained Kinematic Fit

In the fitting procedure above, the vertex was incorporated into the vector of the variables to be fitted (cf. equation 3.15). However, the vertex may be introduced as a set of constraints to the fit, using the method of Lagrangian multipliers. A detailed description can be found in the Paul Avery fitting write-ups (i.e. [53, 56]).

Such a fit is under development in PandaRoot. For the n tracks in the fit the full matrices are used, their size scaling with n. This fitter is aimed at calculating the vertex to a high precision in the offline analysis. Although the development is not completed yet, the vertex position and track momentum results obtained with that fitter are reasonable and precise.

In order to have a relation how well the other vertexing tools can estimate the vertex position the vertex constrained kinematic fitter is being used for comparision.

3.5 Software Implementation

Each of the three vertexing methods is implemented as a class in PandaRoot and linked inside the `libAnalysisTools` library. They are usually used in an analysis macro with `PndAnalysis`, working on the particle candidates (comprising tracks and the PID probabilities). The constructors are given the composite `TCandidate` (the mother particle) with charged particle candidates as daughters (i.e. the measured tracks). In table 3.1 a summary of the classes and their usage is given.

	POCA Finder	Fast Vertex Fit	Vertex Constrained Kinematic Fit
Class Name	`PndVtxPoca`	`PndVtxPRG`	`PndKinVtxFitter`
Calculation	`GetPocaVtx()`	`FitVertexFast()` `FitVertexFull()`	`Fit()`
Vertex Result	written to argument	written to argument & in fitted candidate	in fitted candidate
Quality	return value: $\tilde{D}$	return value: χ^2	`GlobalChi2()`
Options	`GetPoca()`	`SetExpansionPoint()`	(under construction)

Table 3.1: Summary on the available vertexing tools and their usage in PandaRoot.

3.6 Possibilities

In $\overline{\mathsf{P}}$ANDA one of the strong challenges is the event building and the event selection from the trigger-less detector readout. The approach is to evaluate the fast detectors' output and choose whether to analyze the slower components and the higher level information. This has to happen as close as possible to the detector elements, in the data processing line. High performance is expected from algorithms implemented in hardware, i.e. on a Field Programmable Gate Arrays (FPGA) or using graphics chip technologies. In order to exploit the full speed performance from hardware processing the algorithms have to be processed in a parallel manner. The fast vertex fitter as well as the POCA finder inherently feature concurrency with the sum over the tracks and track pairs, respectively. With a fast estimate on the tracklets in the MVD, the primary interaction point can be built up by combining all tracks. Tracks with a high contribution to χ^2, thus originating not from the interaction point, can be sorted out and combined to secondary vertices. From there, depending on the desired event structure, selection criteria can be applied.

Chapter 4

MVD Performance Studies

Designing a detector is a process gradually increasing the detail of its description. Geometry and electronic definitions become more refined, which adds more demands on the simulation's detector representation. In the case of the MVD all the way has been gone from a coarse description of sensitive layers with hit smearing to a thoroughly refined geometry including all passive components with a detailed sensor digitization and reconstruction. Efficiency and resolutions had to be balanced against material budget, data rates, available space and other constrains. In this chapter simulations illuminate the standalone capabilities of the MVD as well as its performance in the whole $\overline{\text{P}}$ANDA setup.

4.1 Silicon Tracking Station

Comparing with data from a real life experiment is an essential step in verifying the simulation results. Developing the MVD sensors, readout electronics and the experiment supplies have had to be designed, built and tested. The Silicon Tracking Station (TS) [57, 47] is one result along these processes and a valuable detection system in its own right.

TS Setup Four boxes equipped with silicon strip detectors surround a rotatable table, two in the front and two in the back. The boxes are aligned in one line (the beam axis) with scintillator triggers at the very front and the very back, each. Precise stepping motors allow to remotely adjust the boxes during operation along the beam axis. In figure 4.1 a CAD drawing and a photograph of the setup are shown.

Each box houses either one fully connected double sided strip sensor or two identical single-sided sensors placed at a small distance perpendicular to each other. All sensors have a strip pitch of 50 µm and are read with the APV25 [58] front-end chip which is triggered by a coincidence signal form the scintillators. All auxiliary electronics and services are integrated with the table setup to be efficiently and compactly installed at different experimentation sites. The rotatable table in the middle of the lineup can be used for any kind of tabletop sized absorber or detector, e.g. other prototype sensors or holding structure prototypes.

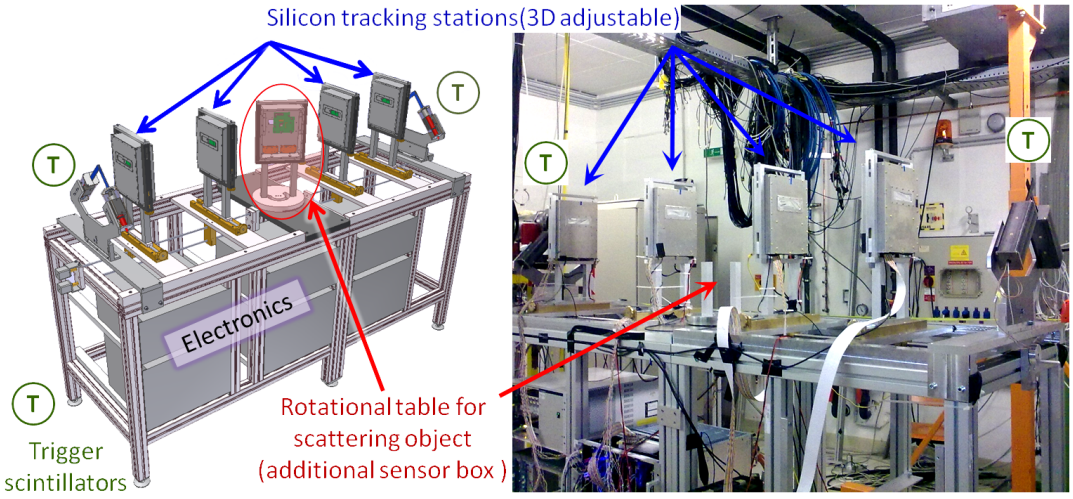

Figure 4.1: CAD drawing and photograph of the Silicon Tracking Station setup. Scintillating triggers (T) toggle the readout of the sensor boxes. On the rotatable stand in the center there is space for a small detector, scatterer or absorber (here, another sensor box in the CAD drawing, empty on the photograph).

Beam Data Analysis Strategy In general this setup follows the strategy of $\overline{\text{P}}$ANDA to use the reconstruction software for both simulations and data. The front-end chips are read out at the trigger signal and their raw data is written to ASCII or ROOT files. A converter passes that data into a PandaRoot compatible structure. Then the reconstruction of the SDS package (see chapter 2) does the cluster finding and hit reconstruction. Straight line tracks without any absorber on the rotatable table are used to perform the sensor alignment [59]. The reconstruction uses then the updated geometry.

Comparison Data Using data from beam tests the simulation results can be compared with the real experiment. For this study data from a beam test at DESY (Hamburg, May/June 2010) have been used. An electron beam of 4 GeV/c momentum was delivered by the accelerator to the tracking station. In contrast to the usual setup one of the boxes was placed at the rotatable table containing a fully connected double sided strip sensor. Different angles to the beam axis have been chosen between 0° and 45°. In table 4.1 the selected angles as well as the corresponding data file names are summarized. These data are referred to in the upcoming sections.

4.2 Default Simulation Settings

$\overline{\text{P}}$ANDA is still in the R&D and prototyping phase, thus the geometry, detector properties and the corresponding software are under change. For comparable results from simulations it is favorable to select one component setup and one stable revision of PandaRoot to perform the simulations, namely the "trunk" version number 12727

Angle	Raw Data File	First Converted File (sequential numbering)
0.0°	data141.hit	data632.root
2.5°	data142.hit	data639.root
5.0°	data143.hit	data646.root
10.0°	data144.hit	data654.root
15.0°	data146.hit	data663.root
24.6°	data147.hit & data148.hit	data671.root
33.6°	data149.hit	data678.root
39.7°	data150.hit	data687.root
44.4°	data151.hit	data696.root

Table 4.1: Data files from the test station. Raw data are the digital information on channel and ADC channel (charge). Converted data are in form of digis with the correct association to the geometry description. Converted data are split into several files, numbered sequentially.

Geometry Version	MVD_2.1			Tracking Station
	Pixel	Strip Barrel	Strip Disks	Strip Squares
Sensor Thickness	200 µm	300 µm	300 µm	300 µm
Readout size	$100 \times 100\,\mu m^2$	130 µm	65 µm	50 µm
Stereo Angle	–	90°	15°	90°
Noise σ_n	$200\,e^-$	$1000\,e^-$	$1000\,e^-$	$1000\,e^-$
Threshold	$1000\,e^-$	$5000\,e^-$	$5000\,e^-$	$5000\,e^-$
Charge Cloud σ_c	8 µm	8 µm	8 µm	0 . . . 50 µm
Charge Measurement	Time Over Threshold			ADC
Centroid	Center of Gravity			

Table 4.2: Default simulation properties of the MVD and tracking station sensors as they have been used in these studies.

from July, 18 2011. The external packages, used are the "may11" distribution from Mar., 3rd 2011.

4.2.1 Detectors

MVD and Tracking Station For the MVD geometry version 2.1 is used, featuring the full detector converted from the CAD drawings. Pixel and strip sensors are 200 µm and 300 µm thick, respectively. The tracking station is simulated with its sensors only, omitting the housing and electronic components because they are not within the beam profile. Digitization and local reconstruction are used as described in chapter 2. Table 4.2 gives the overview of the parameters used here.

Other Trackers In the barrel part the STT in its 1.5 m long version is used including skewed layers. Three GEM disk stations cover the forward barrel part and in the

forward spectrometer, six straw tube plates are used, positioned inside and around the dipole magnet.

Passive Parts A number of components are present in the simulations contributing to the material each track has to pass through. This includes detectors which have been switched off in the simulations, because their information is not necessary in these studies and their processing is time consuming. In the geometry the beam-target pipe cross is present, importantly adding its material before any sensitive element, and the solenoid and dipole magnets and their iron flux return yokes with the muon chambers inside them. Both barrel and disk DIRC parts are there as well as the electromagnetic calorimeter in the barrel forward and the barrel end cap.

4.2.2 Tracking & PID

Barrel Tracking Tracking in the barrel is realized in five steps. Tracklets are searched for in the MVD with the Riemann track finding and in the STT with conformal mapping plus hough transforms. Using these tracklets as first guesses the combined pattern recognition, based on the techniques used in the STT, is performed on MVD and STT hits and then again including the GEM stations as well. Track candidates are fitted with a Kalman filter, employing GENFIT with GEANE. It is noteworthy that the pattern recognition uses the hypothesis that tracks originate from the interaction point, which lead to inefficiencies for trajectories starting 0.5 cm off or more.

Forward Tracking Due to the lack of a realistic tracking implementation (i.e. the track finding and the interface to the kalman filter) for the forward spectrometer part, one has to use information from the Monte-Carlo truth. For each track, producing hits in the FTS stations, all hits in MVD, GEM and FTS from that Monte-Carlo track are collected into the track candidate. The track properties are calculated by a Gaussian smearing of the Monte-Carlo track's values. In the vertex coordinate the smaering Gaussian width is chosen to be $\sigma_V = 200\,\mu\text{m}$ (which is rather optimistic) and for the momentum $\sigma_p/p = 3\%$. Emulating a tracking algorithm's efficiency, 5% of the tracks are not stored.

PID To be independent of the incomplete algorithms, which are currently under development, the whole PID reconstruction is using directly the Monte-Carlo truth information. Therefore DIRC and EMC processing was deactivated.

4.3 MVD Layout Studies

During the process of designing the MVD and its software, the layout properties have been studied [1, 6] using the SDS package in PandaRoot. These encompass a coverage map of the MVD data rates as well as a detailed material budget study.

4.3.1 Detector coverage

Covering the most of the angular region with the MVD is necessary to achieve the design goal of at least four hits recorded per track. Meeting that condition enables the standalone tracking by the MVD without waiting for slower components. This can be exploited for the necessary data reduction by applying filters based on fast detector analyses.

In figure 4.2 the number of hits created per track (1 GeV/c pions) is plotted in a detector map, showing the dependence on the polar and azimutal angles with the interaction point as point of view. Most notable are the two gaps in the barrel part where the target pipe (around $\theta = 90°$ and $\phi = \pm 90°$) fits through. Because the first pixel layer is very close to the interaction point this acceptance hole is for that layer relatively big reducing the number of hits per track in the MVD in that region. In the forward region, where the highest particle flux is expected (cf. figure 1.5), several barrel and disk layers will produce at least four and up to seven hits per track.

For vertex reconstruction it is preferred to have a precisely measured hit as close as possible to the decay point. Deviations due to the track direction or curvature measurement will be less important with the precise anchor point. As most particles decay very close to their creation point the distance of the first hit to the interaction zone governs the overall vertex resolution. Figure 4.3 shows the distance from the interaction point to the first hit in the MVD for slow pions. The first layer of pixel sensors is at 2 to 3 cm distance, featuring the prominent holes for the target pipe as well as gaps in the transition region between the barrel part and the disks which are covered by the second layer of pixel sensors (about 6 cm distance). In the very forward part one can see how the acceptance of the disks ends until only the strip disks can contribute with a precise first hit. This will make vertexing with shallow angled tracks going to the forward spectrometer of $\overline{\mathsf{P}}\mathsf{ANDA}$ more challenging, especially the reconstruction of the z coordinate.

4.3.2 Material Budget

Each piece of material in a particle flight path introduces deviations in form of scattering and absorption. Usually a material's effect is quantized by the radiation length X_0, defined as the distance where an electron would loose a fraction of $(1 - 1/e)$ of its energy by bremsstrahlung. For elements usually a density-independent form

$$\tilde{X_0} = \rho \cdot X_0 \tag{4.1}$$

is used. Composite materials are described by the mass fraction w_i of each element:

$$\frac{1}{X_0} = \sum \frac{w_i}{X_{0,i}}. \tag{4.2}$$

Table 4.3 summarizes selected radiation length values for the MVD. To compare different subsequent detector components a common practice is to give the fraction of traversed radiation length X/X_0. This number should be high for detectors measuring the total particle energy (the EMC) and it should be as low as possible on other systems (basically all inner components).

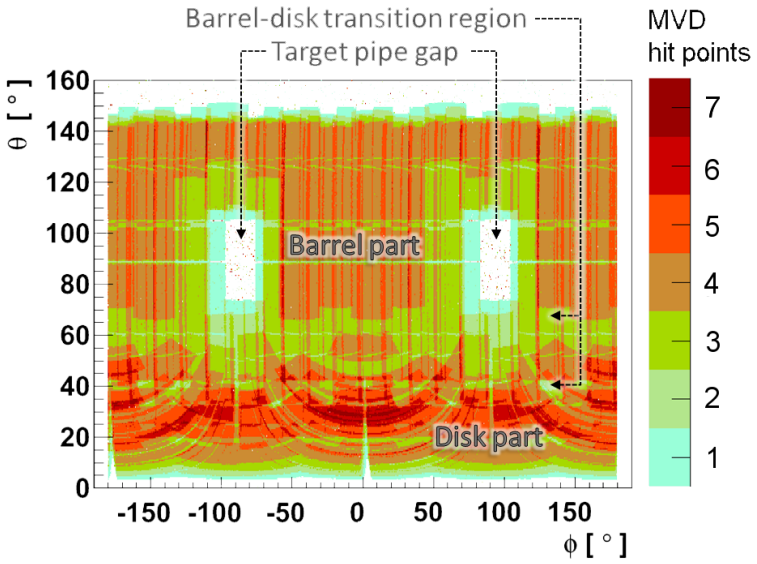

Figure 4.2: Detector coverage: Number of hits per track in different angular regions (pions with 1 GeV/c from the interaction point) [1].

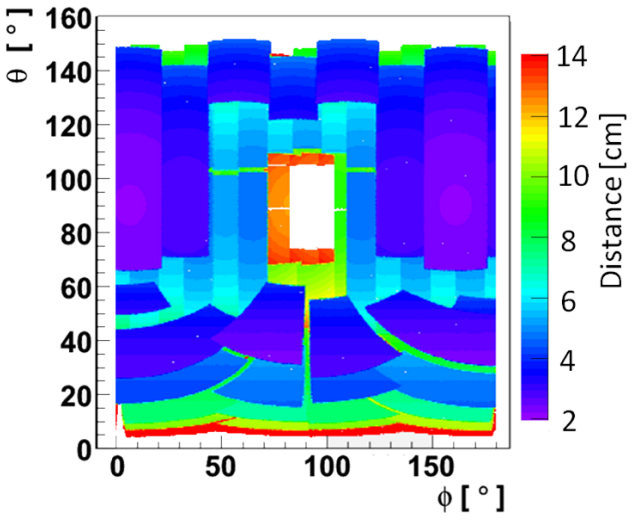

Figure 4.3: First hit distance to the interaction point. (pions with 100 MeV/c from the interaction point) [1].

Material	$\tilde{X}_0$ [g/cm^2]	ρ [g/cm^3]	X_0 [cm]
C	42.7	2.21	19.3
Al	24.0	2.70	8.89
Si	21.8	2.33	9.36
Cu	12.9	8.96	1.44
In	8.85	7.31	1.21
Water	83.3	1.00	83.3
C (foam filling)	42.7	0.227	188
C (fibre structures)	42.7	2.27	18.8
PVC	25.5	1.30	19.6

Table 4.3: Radiation length values for the most common materials in the sensitive region of the MVD.

There is the demand of as few material inside the measuring region as possible, however, front-end chips, support structure and cooling add their material to the sensors themselves. To gain insight which components introduce most influence on particle tracks a study was performed with PandaRoot and the detailed geometry description [6]. Virtual particles ("geantinos"[1]) are ejected randomly from the interaction point with a flat angular distribution. Each trajectory piece in a volume contributes with its radiation length to the accumulated value X. The angular radiation length distribution viewed from the interaction point, shown in the left-hand part of figure 4.4, is not flat but varies strongly with the polar angle region as well as with the azimutal angle.

Most of the barrel and disk part are covered with a relatively small amount of material with two dense regions in the transition between the two parts. Data cables and cooling pipes are routed there ($25° < \Theta < 45°$) to the inner disks. A striped structure is visible in the barrel part. Data cables with metallic signal lines, cooling pipes and the support frames of all components are routed along that way. In the backward part at $\Theta > 145°$ very dense hot-spots are present in form of the converging cable and pipe routing as well as connectors for the MVD services. This unavoidable load of material, together with the services of the STT, will be the biggest challenge for the backward calorimeter cap.

Classifying the radiation length values by the corresponding component in the MVD produces an overview of which parts are benefitting most from optimization (figure 4.4, right-hand side). The largest contribution to the sensitive region is actually given by the cables and the support structures. As a consequence the development of low-X_0 (i.e. thin) cables or local data concentration chips (which reduce the required signal lines) will have a large beneficial impact, whereas thinning the sensors will not contribute much to reduce the material budget.

[1] Internal particle definition in GEANT which is not processed with the transport model's physics processes, thus speeding up the simulations significantly.

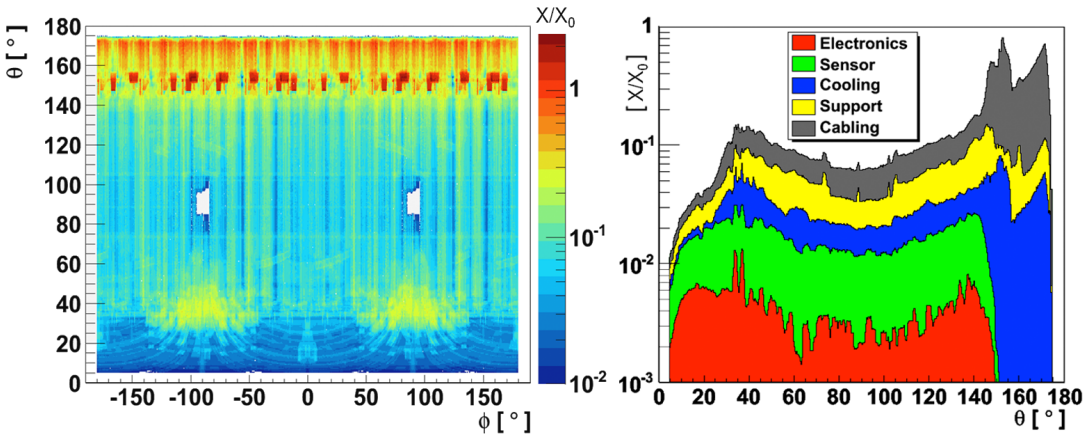

Figure 4.4: Material budget distributions in units of the radiation length X_0. Angular view from the interaction point (left) and contributions of different components along the polar angle. [1]

4.3.3 Rate Studies

Data rates are one of the fundamental challenges in the design process of the $\overline{\text{P}}$ANDA apparatus and the MVD is no exception. As the sensitive element closest to the interaction point the particle flux is highest. Data reduction, compression and transport have to be optimized according to the expected data rates in the different regions and building blocks of the MVD. Such rate studies have accompanied the MVD design process and software development ([60, 61]), the latest results being reported in the TDR [1].

The maximum rates are found at the long strips of the strip modules and at the large-area pixels on the pixel sensor rims, their data rates resulting from their large solid angle covered per channel and the position in the setup (cf. angular distribution of particles figure 1.5). In figure 4.5 data rate distributions on the sensors with the highest load are shown, obtained from antiproton-proton collisions simulated by the DPM event generator. The average rate per channel peaks in the order of 8 kHz for the strip sensors and at 2 kHz for the pixels.

4.4 Sensor Performance

One of the core properties of the MVD is its good spatial hit resolution which will strongly influence the momentum and vertex resolution of the particle tracks. A high number of hits in a long section of a track as well as their resolution aid the momentum reconstruction whereas the resolution and distance of the hit closest to the vertex have the biggest influence on the vertex's resolution.

Spatial resolution on the silicon sensors is in first order determined by the readout feature size, the strip pitch and pixel cell size. Reducing the feature size will increase the resolution as the uncertainty of single-digi hits decreases. Furthermore, a bigger fraction of the tracks create multi-digi hits which can be reconstructed much more pre-

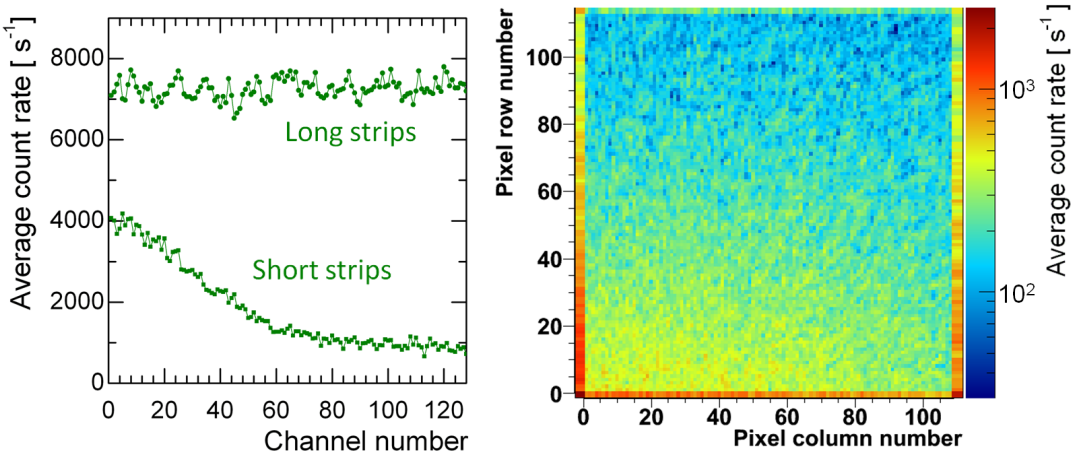

Figure 4.5: Average count rates in the channels of the most loaded strip and pixel front-ends ($\bar{p}p$ events from DPM with an interaction rate of $2 \cdot 10^7\,\mathrm{s}^{-1}$). [1]

cise in connection with the charge measurement. Increasing the sensor thickness would also lead to a higher fraction of multi-digi hits as well, as a sensor design foreseeing a increased charge sharing (e.g. by additional capacitive coupling [62]), however the introduced material contributes to the overall material budget and scattering, increasing the uncertainties for the measurements further on along the track. Additionally, electronics have to be capable of dealing with the data rates. The more channels respond, the more effort has to go into transmitting circuits and cabling. That leads to a higher material load, to a higher power load and in turn to a higher demand on the cooling system. A reasonable compromise between possible resolution and technical demands was found for the MVD in $\overline{\mathrm{P}}$ANDA.

Resolution Requirement Low angle scattering causes the track to deviate from the ideal trajectory for each layer of the MVD which can be described by the Gaussian width of the angular deviation distribution. After the first two layers of the MVD barrel, depending on the incident angle, approximately 800 µm of silicon have been passed (two sensor layers with flip-chip). On the next barrel layer (the first strip sensors), 4 cm away, the scattering causes already deviations of 40 µm to 100 µm for particles with high momentum (cf. figure 4.6) and much more at lower momenta. The MVD contributes with four to six hit points very close to the interaction point to each trajectory measurement. The global trajectory fit (Kalman Filter with realistic propagation) weights these hit's contributions according to their measurement uncertainty, the uncertainty introduced by the scattering and the sensor alignment. Consequently it is not necessary to measure with a much better precision than the scattering distorts the trajectory.

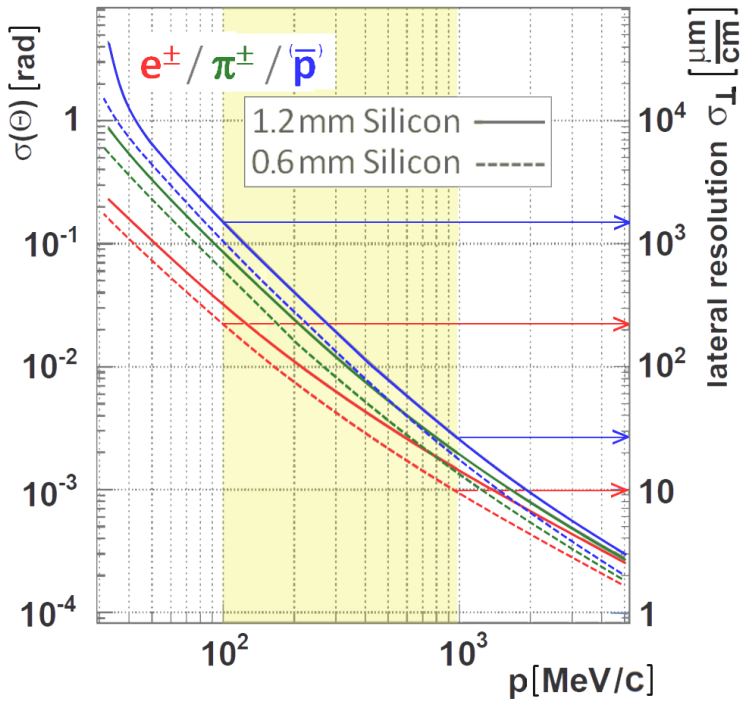

Figure 4.6: Gaussian width $\sigma(\Theta)$ of the scattering angle distribution for different particle species. The dependence on the particle momentum is very strong as well as the amount of scattering material. Typical particle momenta in $\overline{\text{P}}$ANDA are highlighted in yellow.

4.4.1 Centroid Finder Performance

Activating two or more sensitive cells along a coordinate the charge measurement in each cell can be used to reconstruct the position more precisely than the readout structure size on its own would allow. As introduced in section 2.4.2 several approaches are available in the SDS software to find the centroid of a cluster. Here, for convenience, the readout feature size (i.e. the strip pitch) is normalized to 1, so positions are measured in units of strip numbers. An artificial signal charge Q and positions x_{in} and x_{out} were used, calculated from random numbers $r_i \in [0, 1]$:

$$x_{\text{in}} = r_1 - 0.5 \cdot n_{\text{max}} \cdot r_2 \tag{4.3}$$

$$x_{\text{out}} = r_1 + 0.5 \cdot n_{\text{max}} \cdot r_2 \tag{4.4}$$

$$Q = 50 \cdot r_3 \cdot \sigma_{\text{noise}} \cdot n_{\text{max}} \cdot r_2 \tag{4.5}$$

In other words center and a-priori cluster size (up to n_{max}) are randomly chosen as well as the signal charge per path length. Electronic noise (σ_{noise}) and discriminating threshold were set to 1000 and 5000 electrons respectively. The charge cloud width was set to 0.058 which would correspond to 5.8 µm at a readout pitch of 100 µm. Figure 4.7 shows how precise centroids of differently sized clusters are reconstructed using different reconstruction algorithms. To each residual distribution for the different cluster multiplicities a Gaussian was fitted and its width is plotted. Additionally the Gaus-

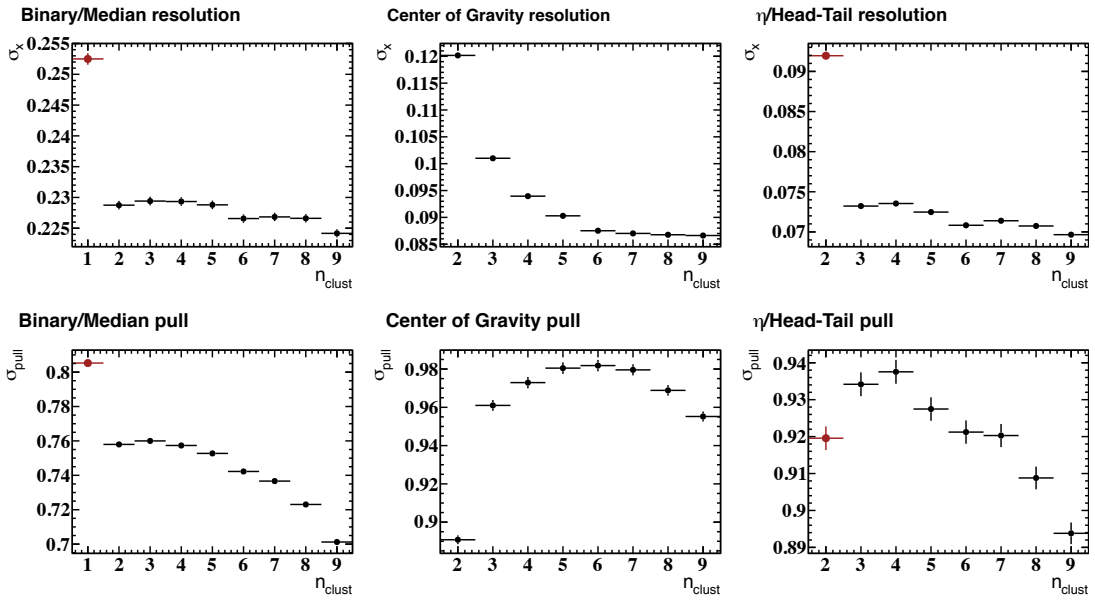

Figure 4.7: Resolutions and the pull distribution widths with the different centeroid finders. Centeroid positions are measured in units of the readout feature size (pitch). Red markers indicate the results of the η- and binary algorithms (only for $n_{\text{clust}} = 2$ and $n_{\text{clust}} = 1$, respectively), presented in the plots for the head-tail and median algorithms, respectively.

sian widths of the pull ($(x_{\text{truth}} - x_{\text{reco}})/\Delta x$) distributions are shown to evaluate the quality of the error estimate.

Clusters with one single channel achieve the worst resolution just below 0.255, which is less than the theoretical resolution ($1/\sqrt{12} \approx 0.289$) of the binary centeroid. Path projections with their center far from the middle of the channel are more likely hitting a second one, thus increasing the quality of the middle-of-channel hypothesis in the binary case of single-hit clusters. The other multiplicities would be reconstructed badly with the binary algorithm because it features n equally displaced residual distribution components, because each channel in a cluster can produce the highest signal (cf. 2.4.2). In other detection setups this method might be a good estimator for the center of a widely dispersed charge cloud, however in the case of the MVD the readout feature size is considerably larger than the cloud dispersion. High multiplicities are produced by angled tracks which leave a flat distribution of charge along the path projection in the readout cells. A better way is the median centeroid, producing residuals just below 0.23. Additionally the charge information is not needed, which makes it an efficient candidate for high-speed hardware implementations. The center of gravity algorithm becomes more precise with rising multiplicity. Clusters with two and three digis, the most prominent cases, achieve a resolution of 0.12 and just above 0.10 respectively. Having extensive knowledge on the sensors and their inner structure, one can at best achieve a resolution of 0.09 with the η- algorithm for $n_{\text{clust}} = 2$. That is a fairly optimistic number because the dependence $x_c(\eta)$ was obtained directly from the simulations truth information (cf. figure 2.7). Any approach in obtaining $x_c(\eta)$ from

measurement, e.g. by integrating the η-distribution, will introduce more uncertainty. For the large clusters ($n_{\text{clust}} > 2$) the head-tail algorithm achieves resolutions better than 0.075, which is about one third of what was obtained in the binary case.

All error estimates are slightly larger than the resolutions (smaller pull width than 1) which means that in a fit these hits have a slightly smaller weight than necessary. The other cases deviate only up to 10 % which is good enough. Because the resolution is measured here in units of the readout feature size, in the worst selection of algorithms on a 100 µm large pixel cell the resolution will be not worse than 25.5 µm.

Algorithm Choice Which algorithm will be used in the MVD lies with what the post-processing hardware will be capable of. When it is favorable not to access the charge information because of a too high data rate, the median will provide a decent resolution. Using the charge information with the center of gravity ($n_{\text{clust}} = 2$) and the head-tail algorithm ($n_{\text{clust}} > 2$) the resolution improves at least by a factor of two. Choosing the η-algorithm over the center of gravity requires the in-depth knowledge of the η distribution without the threshold for each sensor at a small gain in resolution.

4.4.2 Cluster Multiplicities

An important figure of merit for the overall MVD hit resolution is the number of firing digis per track crossing the sensor, the cluster multiplicity. Geometrically, the readout feature size p as well as the sensor thickness d define the angle where a track, approximated by a straight line inside the sensor, hits at least two (or n) readout zones:

$$\alpha_n = \arctan\left((n-1) \cdot p/d\right). \tag{4.6}$$

In the case of the sensors equipped in the tracking station, with a pitch $p = 50\,\mu\text{m}$ and a thickness of $d = 300\,\mu\text{m}$, these angles are $\alpha_2 = 9.5°$, $\alpha_3 = 18.4°$, $\alpha_4 = 26.6°$, $\alpha_5 = 33.7°$, $\alpha_6 = 39.9°$ and $\alpha_7 = 45°$. In figure 4.8 the measured cluster multiplicities for different incident angles are shown. Above the 10° mark the most probable cluster size moves up from one to two which is a bit off from the calculated angle. Several effects influence the cluster sizes. Most importantly the beam is not infinitely precise, so the incident angles are distributed around the nominal value. The trigger acceptance limits the effective beam deviations to a maximum of about 1°. Additionally, the sensor might be not depleted in its full depth which would reduce d in equation 4.6. Channels next to each other will pick up parts of each others signal capacitively, leading to crosstalk and effectively to an increased cluster size.

The MVD will see a mixture of incident angles from different particle species at different momenta and thus bending radii. Figure 4.9 shows the cluster size distribution of simulated events obtained with the DPM event generator and without the charge cloud. Most notable is the high fraction of hits with one digi only. In reality, with the charge cloud and crosstalk, higher multiplicities and thus a better resolution will be achieved.

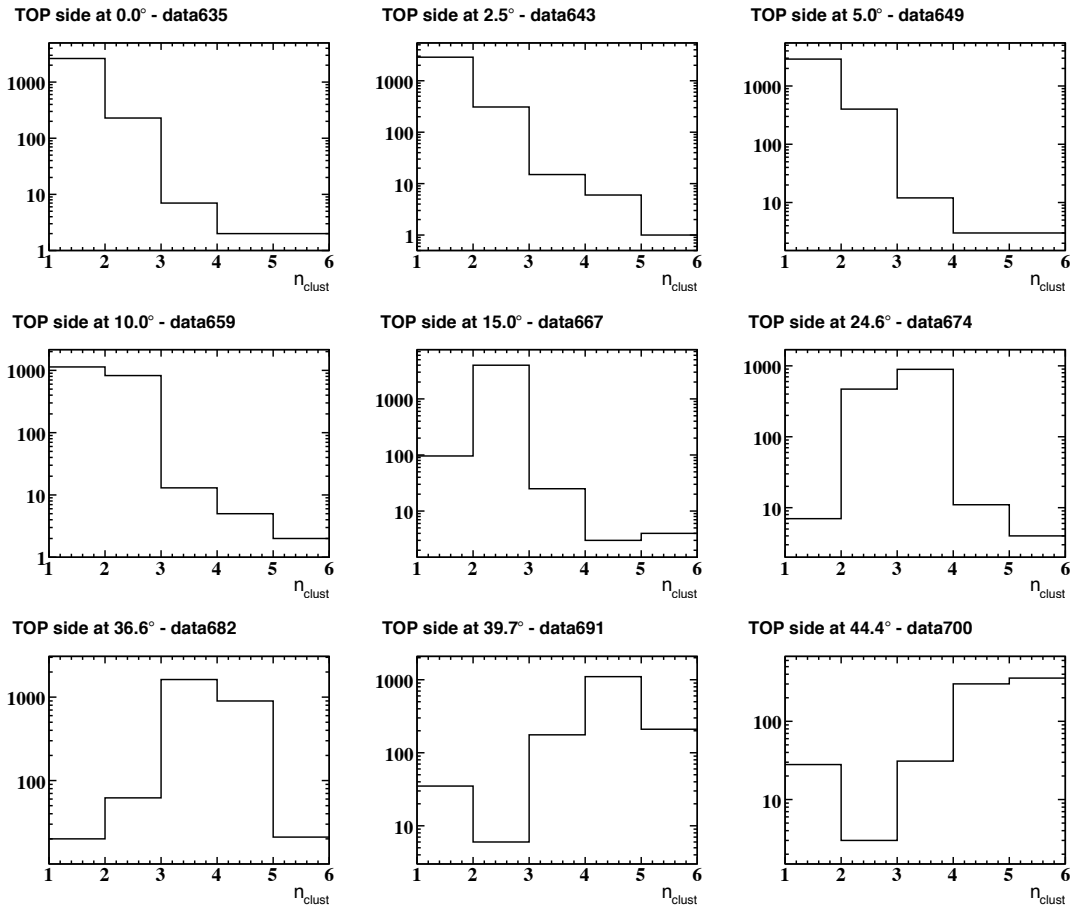

Figure 4.8: Cluster multiplicity distribution in the tracking station (data) for different angles between the beam axis and the sensor surface.

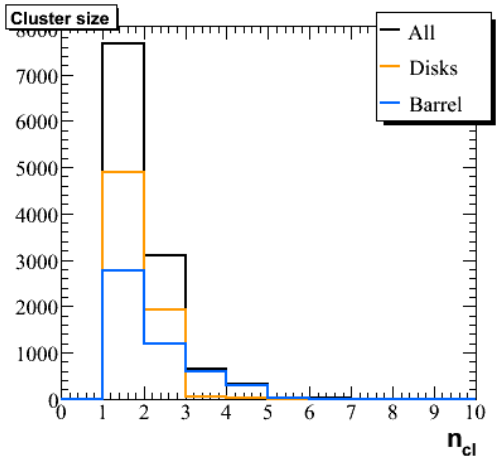

Figure 4.9: Cluster multiplicity distribution in the MVD for simulated inelastic DPM events. Contributions from barrel and disk part are shown additionally. The digitization was performed without the charge cloud.

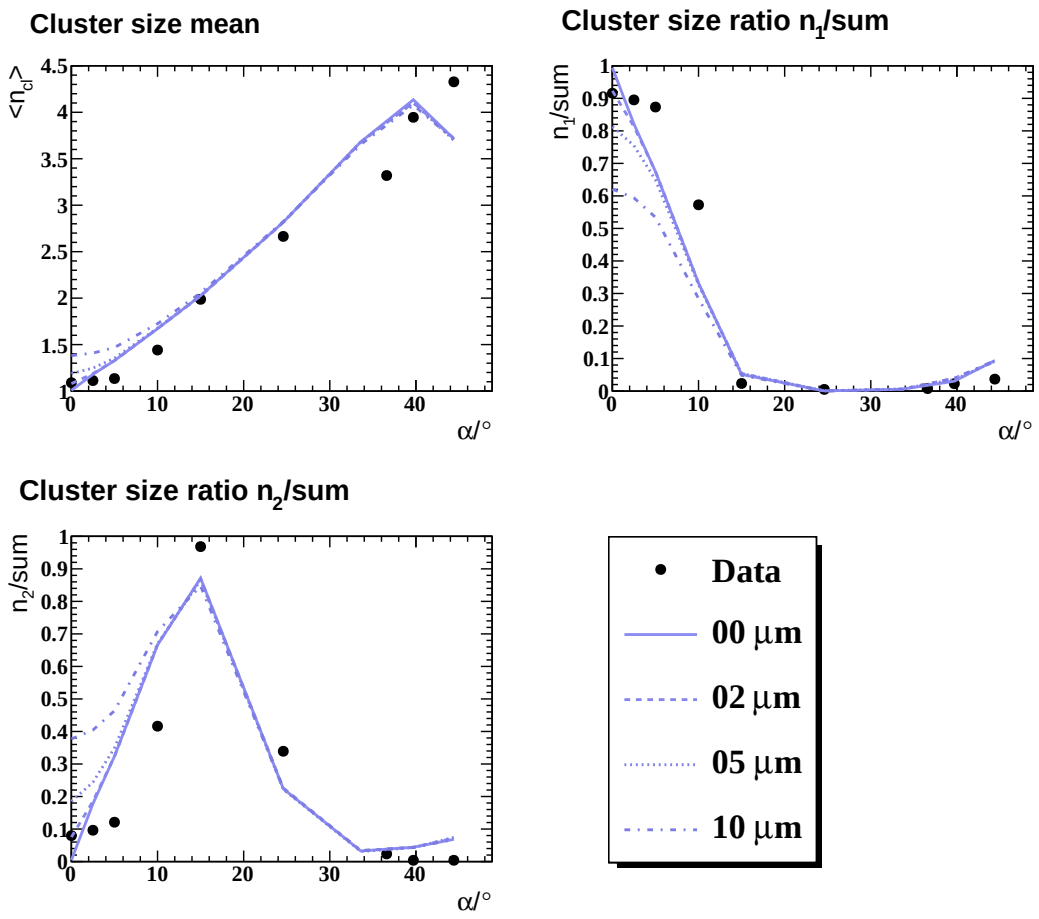

Figure 4.10: Mean strip cluster sizes (upper left) and the fraction of clusters comprising only one (upper right) strip and two (lower left) strips for different charge cloud sizes σ_{cloud} at different track incident angles. The black dots represent data from the Tracking Station (see 4.1). An electron beam with 4 GeV/c was used both in simulation and experiment.

4.4.3 Charge Cloud Width

In the literature the dispersion width of the charge cloud is given with $\sigma_{\text{cloud}} = 5.81\,\mu\text{m}$ [48] for 300 µm thick silicon sensors. To compare the simulation description with experimental data form the tracking station, different charge cloud widths have been simulated. The sensors in the tracking station are 300 µm thick and assumed to be fully depleted. Looking at the mean cluster multiplicity in figure 4.10 in dependence on the incident angle, no charge cloud at all would match the data best in general. With the charge cloud activated the curvature at low angles (i.e. almost perpendicular to the sensor surface) is reproduced better but with an offset. More important to the mean cluster multiplicity is the fraction of single-digi clusters as these can only be reconstructed with a resolution of $1/\sqrt{12}$. As shown in figure 4.10, the charge cloud produces at low angles more two-digi clusters than the data show and

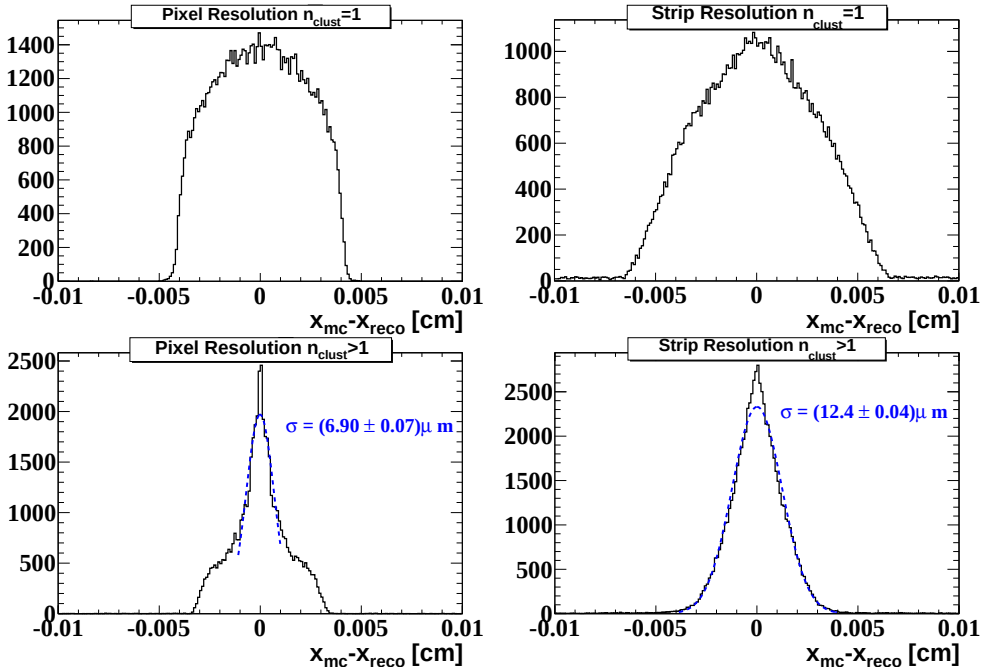

Figure 4.11: Resolution on pixel and strip sensors of the whole MVD for 1 GeV/c pions, sent isotropically in θ and ϕ. Shown are the residuals of the reconstructed hits to the generated Monte-Carlo points. The upper row shows the residuals for clusters with only one readout channel firing, the lower row clusters with at least two channels reconstructed with the center of gravity method.

even the transition region around the angle where a track hits geometrically always two readout cells is not matched perfectly. The simulations produce too many two-digi hits and too few one-digi hits. One hypothesis to explain this is that in the real sensor a fraction of the charge is not detected. Especially capacitive losses to the bulk material and neighboring readout cells the received signal is reduced. Low signals in neighboring channels, which would be more abundant, are cut by the threshold thus effectively reducing the multiplicity.

4.4.4 Hit Resolution With Pions

In order to get a comprehensive and realistic view of the reconstruction performance in the whole MVD ($7° < \theta < 140°$) a simulation with four charged pions (two π^+ and two π^-) with a momentum of 1 GeV/c was performed. Because of the mixture of sensor types in the MVD, 100 µm large pixels as well as 130 µm and 65 µm large strips, the resolution is a composite of these contributions. In figure 4.11 the residual distributions are separated by pixel and strip detectors as well as by cluster multiplicity $n_{\text{clust}} = 1$ and $n_{\text{clust}} > 1$. Residuals for single-hit clusters range up to half the readout feature size, as expected. Larger clusters achieve resolutions of 6.9 µm and 12.4 µm for pixels and strips, respectively. An interesting feature can be seen with the pixel residuals. Clusters with several digis in the local y projection (on the sensor surface)

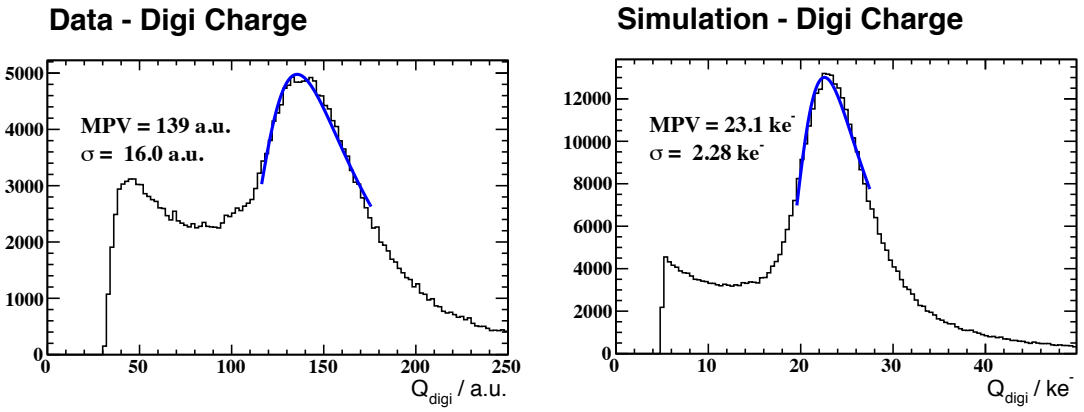

Figure 4.12: Energy calibration performed on the Tracking Station data (4 GeV/c electrons perpendicular on sensor no. 1, front-end no. 1). Matching the Landau peak (most probable value) of the charge distribution with simulations, to which the corresponding energy loss is proportional with 3.6 eV [48].

and only one in x are present in the plot for $n_{\text{clust}} > 1$. The width of that contribution, the bottom of the distribution, is less than the single-hit clusters, so a lower estimate on the error may be made to aid the track fitting.

4.4.5 Energy Calibration

Experiment data contains the charge measurement in arbitrary units originating from the ADC channel numbering or the Time-over-Threshold (TOT) measured in clock cycles. Differences in the front-end electronics, e.g. from different optimum settings to reduce noise or from varying amplification gain due to manufacturing, will require individual calibration for each front-end channel. One possibility of calibration is by the Landau peak in the energy loss distribution for perpendicular tracks, another one by injection of a defined calibration charge pulse in the front-end chip. Relative calibration between the readout channels is performed with that calibration pulse for each front-end individually. Between the front-ends the calibration is done with the charge spectrum.

In figure 4.12 such a calibration is shown for Tracking Station data. The front-end number 1 on sensor 1 was chosen with the 0.0° setup and compared to its simulation. For the calibration in the charge spectrum a Landau distribution was fitted to the peak. Figure 4.12 shows charge distributions of the measurement and the simulation, including the fits. The most probable value (MPV, a parameter of the Landau distribution) was used to obtain the calibration constant at $k = 0.166\,\text{ke}^-/\text{a.u.}$ As a crosscheck the discriminator thresholds (nominal $5\,\text{ke}^-$) are compared. In the data the first bin is at 30 a.u. which corresponds to $4.98\,\text{ke}^-$.

Variable	Initial Range
x	$-1.5 \ldots 1.5\,\mathrm{cm}$
y	$-1.5 \ldots 1.5\,\mathrm{cm}$
z	$-1.5 \ldots 1.5\,\mathrm{cm}$
p_t	$0.9 \ldots 1.1$ GeV/c
θ	$(\theta_\mathrm{v} - 0.3\pi) \ldots (\theta_\mathrm{v} + 0.3\pi)$
ϕ	$0 \ldots 2\pi$

Variable	"Smearing"
x	$\sigma = 50\,\mu\mathrm{m}$
y	$\sigma = 50\,\mu\mathrm{m}$
z	$\sigma = 50\,\mu\mathrm{m}$
p_x	$\sigma = 0.01$ GeV/c
p_y	$\sigma = 0.01$ GeV/c
p_z	$\sigma = 0.01$ GeV/c

Table 4.4: Clean particle property distribution. Momenta are created by their angular orientation and transverse component but redistributed in their cartesian representation. θ_v is the vertex vector's polar angle.

	POCA		Fast Fit		Full Fit		Pulls (Full Fit)	
Variable	$2\pi^\pm$	$4\pi^\pm$	$2\pi^\pm$	$4\pi^\pm$	$2\pi^\pm$	$4\pi^\pm$	$2\pi^\pm$	$4\pi^\pm$
$x/\,\mu\mathrm{m}$	73.2	46.5	62.5	38.4	52.7	31.9	1.00	0.979
$y/\,\mu\mathrm{m}$	71.0	48.1	61.6	38.5	52.2	32.4	0.988	1.00
$z/\,\mu\mathrm{m}$	86.4	51.0	63.4	40.9	59.5	36.9	1.01	0.991
$p_x/(\mathrm{MeV}/c)$	-	-	-	-	9.98	10.0	0.990	1.00
$p_y/(\mathrm{MeV}/c)$	-	-	-	-	10.0	9.96	0.996	0.993
$p_z/(\mathrm{MeV}/c)$	-	-	-	-	9.95	10.0	0.998	1.00

Table 4.5: Collection of the Gaussian fit widths σ of the vertexing residuals for the two and four artificial pion cases with the POCA finder, fast fit, and full fit as well as the full fit pull distribution widths.

4.5 Vertexing Performance

As the MVD is designed to do the vertexing in $\overline{\mathsf{P}}\mathsf{ANDA}$, detailed knowledge of its performance is necessary. Several simulation studies have been performed to monitor the behavior of the system. The performance of the vertex fitting tools themselves were tested as well as the vertexing resolutions and their homogeneity in the MVD.

4.5.1 Vertex Fitter Validation

Clean Samples Understanding the fitting tools in detail requires a clean data sample at the fitters input to eliminate all other distorting effects the real setup will have. Therefore tracks have been created "by hand" with well defined properties. Each event a randomly chosen vertex and a set of n randomly chosen three-momenta have been created. Their values have been redistributed randomly by a Gaussian to emulate the measurement in a controlled way. In table 4.4 these properties are summarized.

Two cases with different track multiplicities have been studied, the first consisting of two and the second of four charged pions, their charges adding up to zero. Three vertexing tools were used on the same data: The POCA finder, the fast vertex fit as well as the full vertex and momentum fit. All residual distributions are centered around zero and are matched well with the Gaussian fit functions, although the POCA

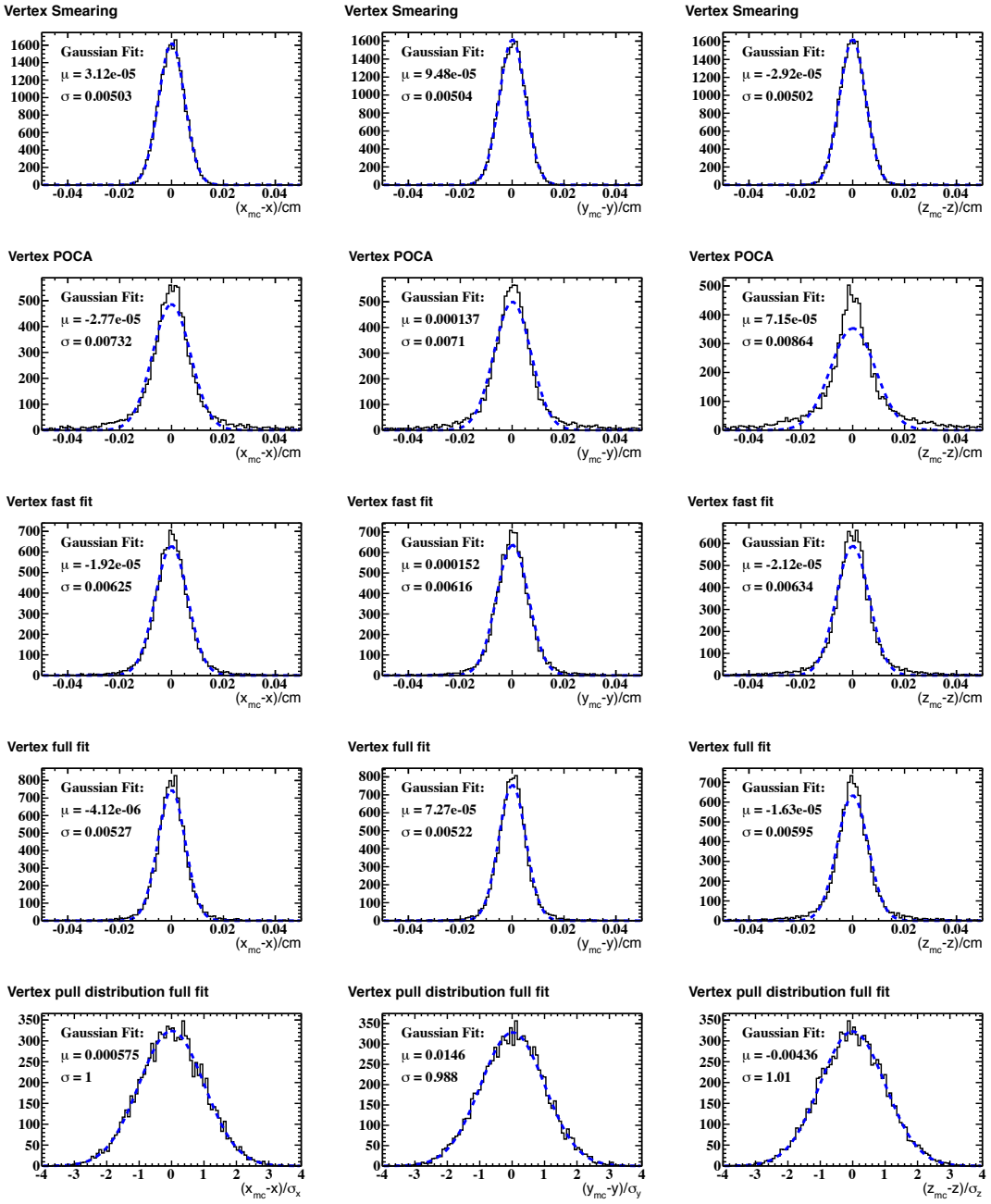

Figure 4.13: Vertex resolutions for two artificial pions. Different vertex fitters are compared. Top to bottom rows: Vertex input, POCA Finder, Fast Fit, Full Fit, Full Fit pulls.

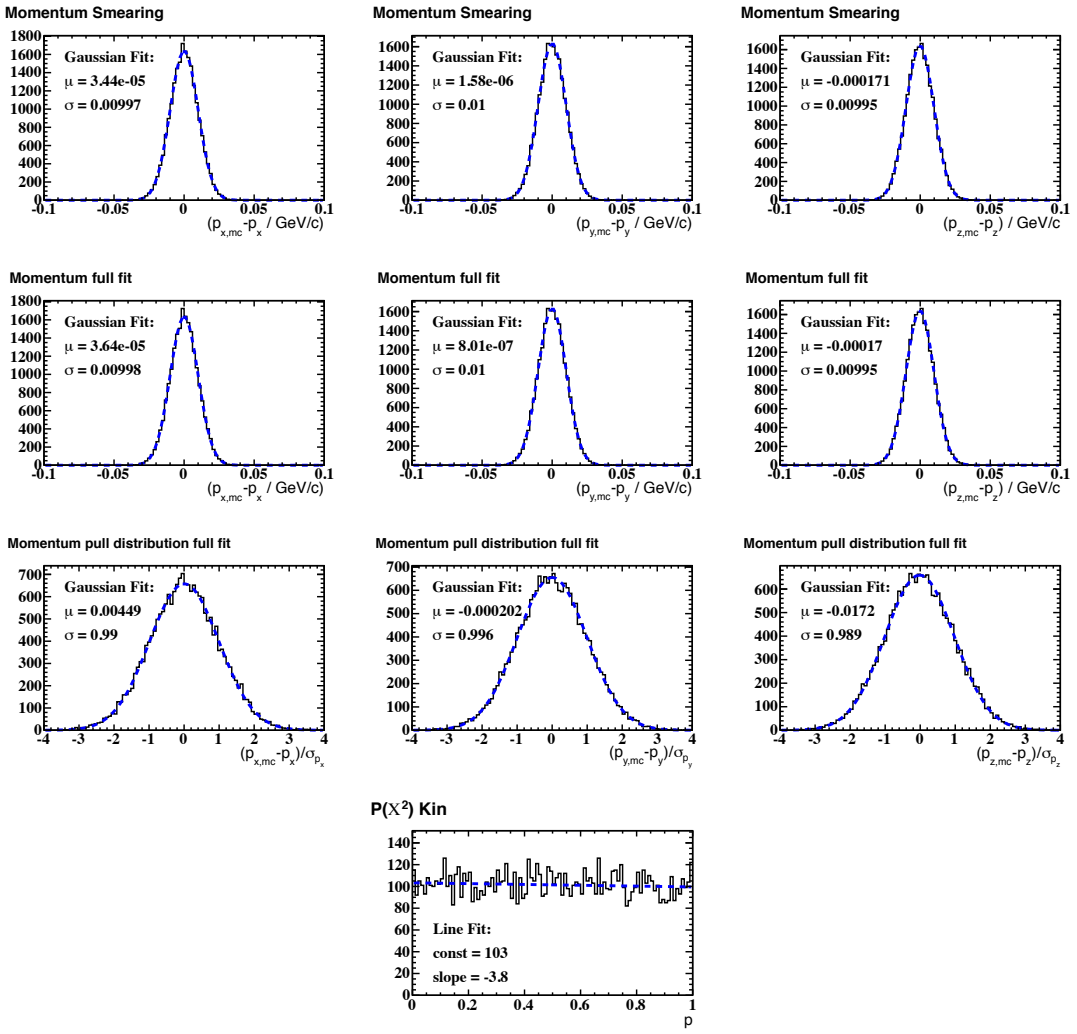

Figure 4.14: Momentum resolutions for two artificial pions. Top to bottom rows: Momentum input, Full Fit, Full Fit pulls and the probability distribution of the χ^2 values.

finder residuals don't need to be Gaussian distributed. In figures 4.13 and 4.14 the resulting residuals are shown for the two pion case. The residuals are slightly wider than the original smeared values. Obviously the full fit delivers the best resolution here, very close to the 50 µm used for the smearing, while the fast fit is with about $\sigma_V \approx 60\,\mu m$ less precise. With a width of about $1.5 \cdot \sigma_{smear}$ the POCA finder produces residuals which are expectedly larger. However, that resolution is quite good considering the small amount of mathematical operations and thus the availability of a very fast method to separate secondary decays. The pull distributions (residuals divided by their uncertainty) for the full fit have a width of 1 and the probability distribution of the χ^2 values is flat (figure 4.14, bottom), showing that the fit is performing well. Furthermore, the full fit reconstructs the momenta as good as the measurement uncertainty allows because the fit adjusts only the momentum azimutal angle.

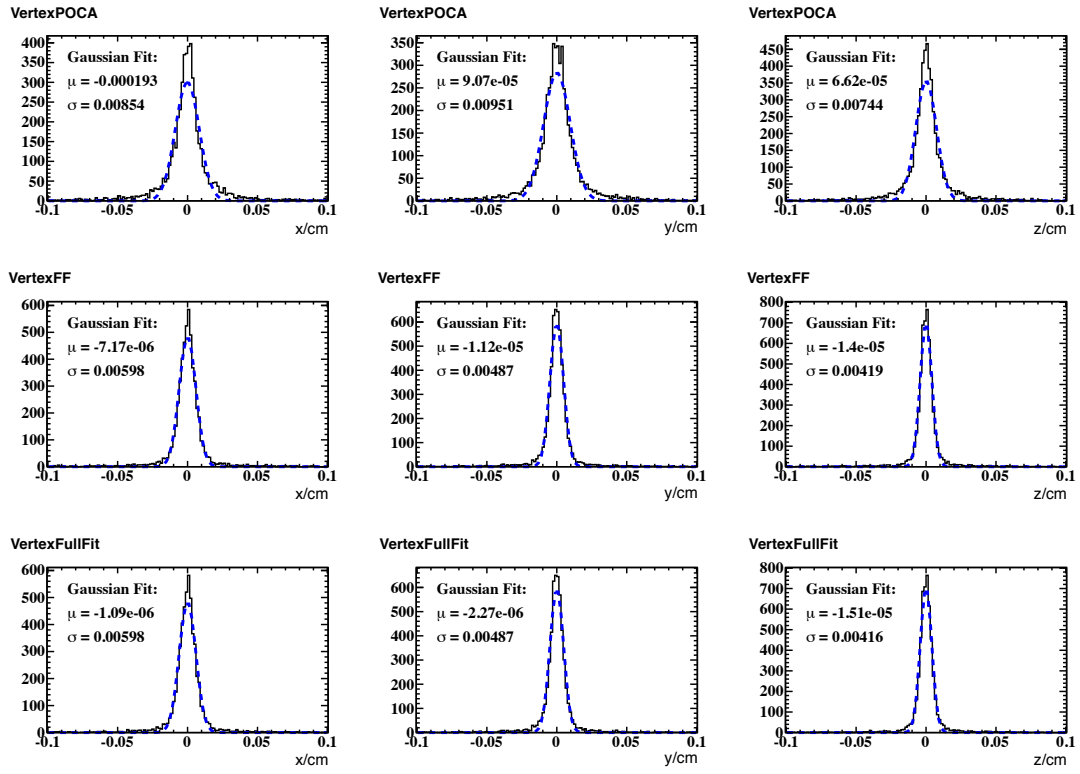

Figure 4.15: Vertex resolutions with four pions simulated in the complete $\overline{\text{P}}$ANDA detector. POCA finder, fast fit and full fit are compared.

Adding two more tracks to each event adds information and improves the vertex resolution significantly. Table 4.5 summarizes the residual distribution widths of both cases. Even the POCA finder achieves a resolution better than the single track position accuracy due to the fact that all tracks have different directions. Tracks going into similar directions, e.g. from a decay of a fast particle, would not improve the resolutions as much.

Full detector with four pions After verifying the vertexing tools' stability in a very controlled environment, simulation data with the full $\overline{\text{P}}$ANDA detector and its simulation chain were used to compare the tools, again. The data is a subset of the study in the MVD TDR [1] which is shown in 4.5.2 below. Four charged pions (two positive, two negative) with 1 GeV/c momentum have been ejected from the interaction point with evenly distributed directions. The vertex resolutions achieved after the whole reconstruction chain are presented in figure 4.15. Both fitters achieve resolutions of about 50 µm, the full fit being slightly better with the center of the distribution and the POCA finder results are all below 100 µm.

Full detector with neutral secondary D meson decays Finding secondary decay vertices is a central goal of the MVD. A simulation of the $\overline{p}p \to D^0\overline{D}^0$ reaction

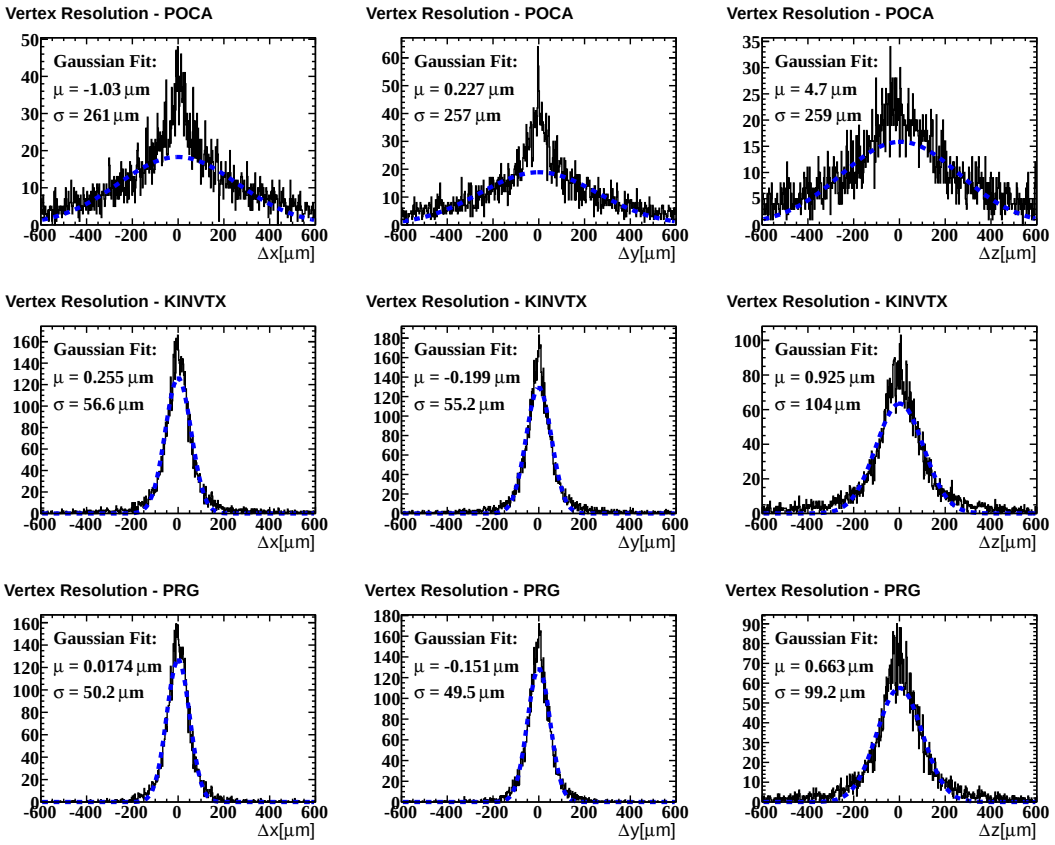

Figure 4.16: Vertex resolutions for neutral D meson decays ($\overline{D}^0 \to K^0\pi^+\pi^-$). The initial state is at $\sqrt{s} = 3770\,\mathrm{GeV}/c^2$) which corresponds to $p_{\mathrm{lab}} = 6.6\,\mathrm{GeV}/c$. POCA finder, kinematic vertex fit and full fit are compared.

at a center-of-mass energy of the $\Psi(3770)$ meson ($p_{\mathrm{lab}} = 6.6\,\mathrm{GeV}/c$) was used to investigate the $\overline{D}^0$ decay. The selected decay channel is $\overline{D}^0 \to K^0\pi^+\pi^-$ where only two charged tracks contribute to the vertex measurement. Figure 4.16 shows the resolutions achieved with the POCA finder, the vertex fitter described in chapter 3 and the kinematic vertex fitter. Both fitters achieve resolutions around the 50 µm mark in x and y and twice as much in z. The POCA finder struggles because the pions are not as fast as in the studies above and scattering deviates the tracks much more.

4.5.2 Vertexing Consistency

The MVD is only roughly symmetric and its symmetry is broken when looking closer at the details. First there is the beam-target pipe cross, cutting the geometry in half. Second, the sensor arrangement is tilted or staggered to accommodate with the available space while covering the gaps. So the question arises whether these deviations of the symmetry effect the vertex resolution, or not. That study was performed for

the MVD TDR [1] and its results are repeated here to show the performance of the software tools in relation with the whole $\overline{\text{P}}$ANDA setup.

Each event two positively and two negatively charged pions are produced. Their directions are distributed uniformly in the full azimutal range ($0° \leq \phi \leq 360°$) and the polar angle in the sensitive region of the MVD ($10° \leq \theta \leq 140°$). A momentum of 1 GeV/$c$ was chosen for reasonably curved trajectories, to get always a similar behavior from the tracking code and to be less effected by energy loss and scattering. The positions where the pions are ejected were chosen from three paths:

Radial Along the y-axis, between 0 cm and +1 cm

Longitudinal Along the z-axis, the beam pipe, going from −1 cm to +1 cm

Circular On a circle in the x-y-plane with a radius of 0.1 cm

Each initial vertex setting was simulated with 10000 events using the default settings described in 4.2. The POCA finder was used to obtain the reconstructed vertices. Gaussian fits to the residual distributions around the nominal values produce the resolution values shown in figure 4.17. The three scans show a good flatness over a wide range up to the limitation of the preliminary tracking which performs well at the interaction point and up to 0.5 cm away.

One interesting effect can be seen by comparing the resolution in x and y. Symmetry arguments say that these should be the same, however the x-coordinate is measured worse then y. When investigating the resolution distribution in the polar angle the region of the MVD barrel part can be identified as the region with the resolution difference (figure 4.18). A detailed investigation [1] shows that the measurement performance is not symmetric in ϕ. The target pipe is going straight along the y-axis so scattering worsens the x resolution of tracks from the interaction point as they travel through the pipe wall. Furthermore the acceptance gaps of the first pixel layer are large around the target pipe hole and tracks there have the first measured hit further away form the interaction point.

4.6 Benchmark Channel: D mesons

Studying charm physics mostly involves open-charm, D mesons, in the intermediate states. Especially charmonium states above the $D\overline{D}$ threshold have a high probability to decay into a state featuring a $D\overline{D}$ pair which then decay into the final state of kaons, pions etc. Also, charm physics include studying the spectrum of exited D mesons, which will decay into the D ground states. Typically the cross sections to create charm are very low (in the order of nb to pb), thus the identification and precise measurement of D mesons as well as a performant background suppression are vital.

D mesons contain one charmed and one light quark. Such as kaons they can decay only weakly due to the quark flavor content what leads to a comparably long life time and thus a long distance of flight. For the charged ground state D mesons the decay length is $c\tau = 311.8\,\mu\text{m}$ and $122.9\,\mu\text{m}$ for the neutral D mesons [63]. With the momentum from the excess energy in the center-of-mass system the relativistic decay length in the laboratory system ($\gamma\beta c\tau = \frac{p}{m}c\tau$) will be even larger. A good

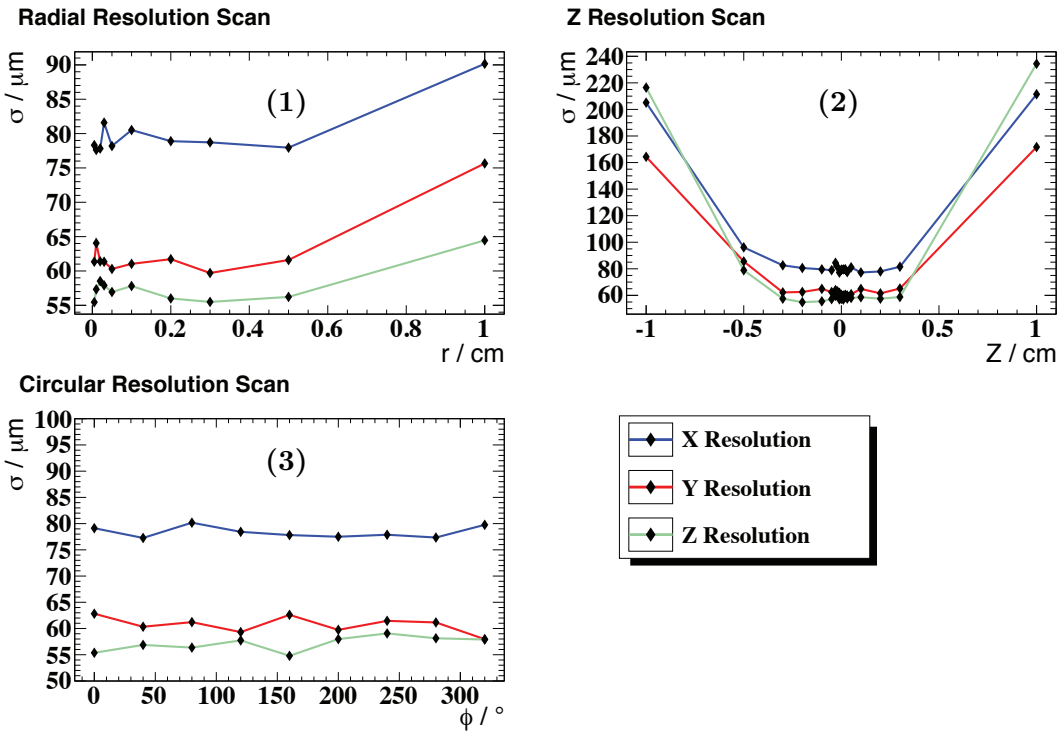

Figure 4.17: Mapping of the four-pion vertexing results, changing the creation point: **(1)** along the radius r (with $\phi = 0°$ and $z = 0$). **(2)** along the z axis of the MVD. **(3)** on a circle of 1 mm radius in the transverse plane at $z = 0$.

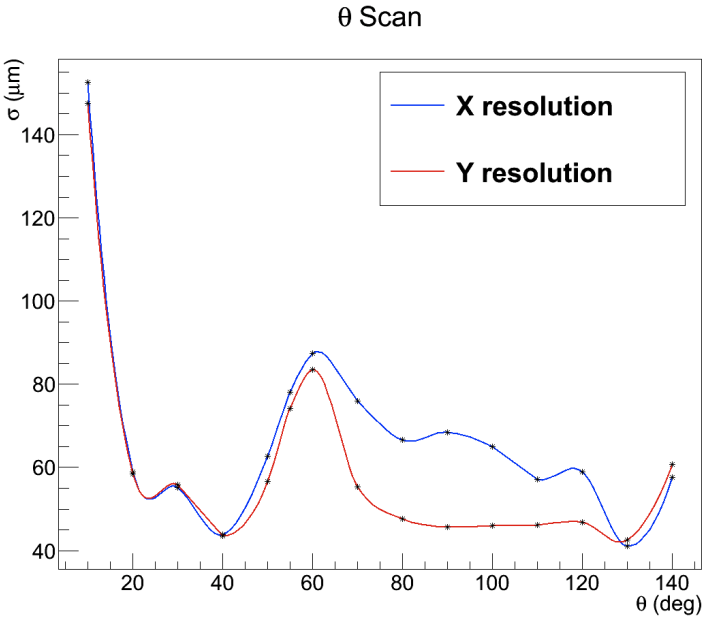

Figure 4.18: Vertex resolution behavior for four pions emitted under the same polar angle but randomly chosen azimutal angles. Both x and y resolutions are plotted, showing the deviation in the MVD barrel part.

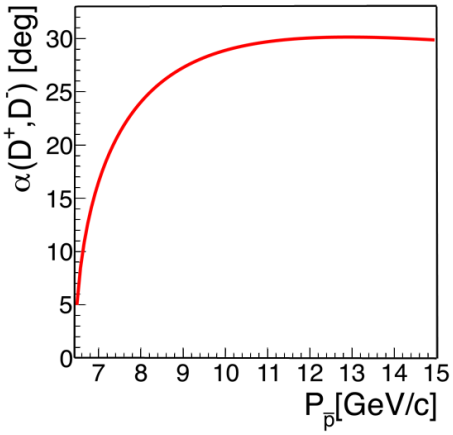

Figure 4.19: Maximum opening angle between the D^+ and D^- in direct formation from $\overline{p}p$ depending on the $\overline{p}$ beam momentum

vertexing will largely contribute to the separation of such events containing D mesons from all the background events with the same final state by discriminating the decay vertex positions. Background will originate from the interaction point, while the decay vertices of the D mesons are distributed further away.

In order to have a clean signal channel, the production of one $D\overline{D}$ pair from the initial $\overline{p}p$ state has been chosen over the decay of an intermediate resonance. Both charged and neutral D pairs were under investigation, decaying to the most prominent final state, each, comprising only charged particles:

$$\begin{aligned} (1) \quad & \overline{p}p \to D^0\overline{D}^0 \quad \to K^-\pi^+K^+\pi^- \\ (2) \quad & \overline{p}p \to D^+D^- \quad \to K^-2\pi^+K^+2\pi^-. \end{aligned}$$

At the interaction point the $\overline{p}p$ system creates a $D\overline{D}$ pair, which decays separately at secondary vertices under emission of the daughter particles. In terms of monitoring the vertexing performance these channels provide vertices from two and three tracks, which are the most prominent cases in a low multiplicity experiment such as $\overline{\text{P}}$ANDA.

Both channels have only two particles exiting the primary vertex. The maximum opening angle between the D mesons is kinematically determined (back-to-back in the center-of-momentum frame) by the beam momentum which, as shown in figure 4.19, has a maximum representing a balance point between the excess energy adding to the transverse momentum and the forward boost of the whole system. A small opening angle would cause most of the final state particles to be measured in the forward spectrometer of $\overline{\text{P}}$ANDA whose reconstruction presently is based on the Monte-Carlo truth information. It is convenient to avoid that part of the detector for this study and to produce most of the tracks in the barrel spectrometer's acceptance. Usually the choice of the center-of-momentum energy $\sqrt{s}$ falls to one of the charmonium resonance masses, however a moderately high antiproton momentum of $p_{\text{lab}} = 9\,\text{GeV}/c$ ($\sqrt{s} = 4.33\,\text{GeV}$) has been chosen which yields a reasonably large maximum opening angle of about 27° for the $D\overline{D}$ pair.

D^0	POCA	Fast*	KinVtx
σ_x/ µm	47.3	57.9	44.3
σ_y/ µm	45.6	51.6	42.9
σ_z/ µm	88.4	94.9	90.2

$\overline{D}^0$	POCA	Fast*	KinVtx
σ_x/ µm	47.5	58.3	44.6
σ_y/ µm	46.3	51.9	43.5
σ_z/ µm	88.4	94.1	89.3

D^+	POCA	Fast*	KinVtx
σ_x/ µm	56.9	86.1	46.9
σ_y/ µm	56.3	84.8	46.1
σ_z/ µm	113	125	93.2

D^-	POCA	Fast*	KinVtx
σ_x/ µm	57.4	85.3	46.3
σ_y/ µm	56.0	84.4	45.7
σ_z/ µm	110	123	94.1

Table 4.6: D^0, $\overline{D}^0$, D^+ and D^- vertex resolutions (beam momentum $p_{\text{lab}} = 9\,\text{GeV}/c$) obtained with the available vertex fitters. (*A preliminary version of the fast fit was used.)

4.6.1 D Reconstruction

Decay Vertices After the full simulation and reconstruction chain (with ideal PID) particle candidates for kaons and pions are combined according to one D meson type (e.g. one negative kaon and two positive pions for a D^+). The resolutions are presented in table 4.6, obtained from three vertexing tools. In all cases the x and y resolutions are similar to each other (in the order of 50 µm) and better by a factor of two than the z resolutions. That difference is expected qualitatively considering the maximum opening angle of about 27° as most tracks have a shallow polar angle and deviations have more effect on the z coordinate than on the others. Comparing the performance for the two-track vertices (neutral D's) with the three-track vertices (charged D's) one finds that adding another track with a similar direction to the set does not help the vertex finding and even makes the vertex less precise through the additional uncertainty. There is no visible difference between particle and antiparticle vertex reconstruction. In the comparison between the vertexing tools the POCA finder performs very well, showing residuals in the same order of magnitude as the kinematic fitter for the neutral and slightly larger ones for the charged D mesons.

Because the kinematic fitter as well as the fast fitter were in a preliminary state the POCA finder was selected in this analysis. With the reconstructed vertex at hand and the track momenta recalculated at the vertex position the properties of the mesons are accessible.

Background Reduction Background is produced additionally to the signaling channel. Non-resonant background producing the same final state gives the largest contribution. Another source are different final states where one or more particles were not measured, e.g. a photon escaped the acceptance, or where particles were wrongly identified, thus mimicking the signature of the signal channel.

In addition to the signal channel there will be a huge contribution by non-resonant background yielding the same final state as well as from mismeasured events of a similar final state. Typically the cross section for these non-resonant channels is several orders of magnitude higher than the signal. Removing this background while maintaining the small signal yield is the biggest challenge in particle physics analysis.

	$D^0/\overline{D}^0$	comb.	nonres.
Simulated events	98800	–	198025
Simulated D's	197600	(197600)	(396050)
D's After reconstruction	135024	27161	322771
150MeV Mass window	102763	2232	23301
Vertex r and z cut	17255	194	543
4C kinematic fit	1592	18	2
Total efficiency ϵ	$8.06{\cdot}10^{-3}$	$9.11{\cdot}10^{-5}$	$5.05{\cdot}10^{-6}$

	D^+/D^-	comb.	nonres.
Simulated events	99200	–	344525
Simulated D's	198400	(198400)	(689050)
D's After reconstruction	120835	67039	688188
150MeV Mass window	61579	21963	67650
Vertex r and z cut	15004	689	1060
4C kinematic fit	1058	25	0
Total efficiency ϵ	$5.33{\cdot}10^{-3}$	$1.26{\cdot}10^{-4}$	$< 1.45{\cdot}10^{-6}$

Table 4.7: Effect of sequentially applying the selection criteria. The D meson counts comprise the signal, fake signal ("combinatorics") and non-resonant background.

Common background reduction techniques employ cuts on kinematical values as well as fits to the particle set with special constraints.

This study[2] focusses on the non-resonant background with the same final state as the signal. Because $\overline{\mathsf{PANDA}}$ will measure events exclusively it is expected to distinguish background originating from another final state very efficiently by the difference in the sum of four-momenta to the precisely known initial state. For example, wrong particle identification would lead to a differing $\sqrt{s}$ and such an event could be discarded easily. The approach for the D mesons is first to combine suiting pion and kaon tracks to D candidates. A broad cut on the mass is performed with a 150 MeV window around the nominal D mass. A selection on the D candidate vertices are made using the POCA finder for vertex reconstruction. Vertices with a "distance" value calculated from the POCA finder (cf. 3.1) of more than 300 µm are considered to be bad track combinations and vertex positions smaller in the z-coordinate than 478 µm are likely to be a set of tracks originating directly from the interaction point. In the end a computing intensive fit (4C-fit) is performed using the initial $\overline{p}p$ system's four-momentum as constrains. The fit's χ^2 probability $p(\chi^2, \text{n.d.f.})$ is required to yield more than 0.001 in order to reject the last fraction of badly matching combinations. Table 4.7 shows the effect of these selections on the D meson and background yields.

Signal-to-Background Ratio One of the main goals of the MVD is to reduce the background when measuring D mesons by vertex separation. The question is how

[2]Background reduction performed in collaboration for the MVD TDR [1].

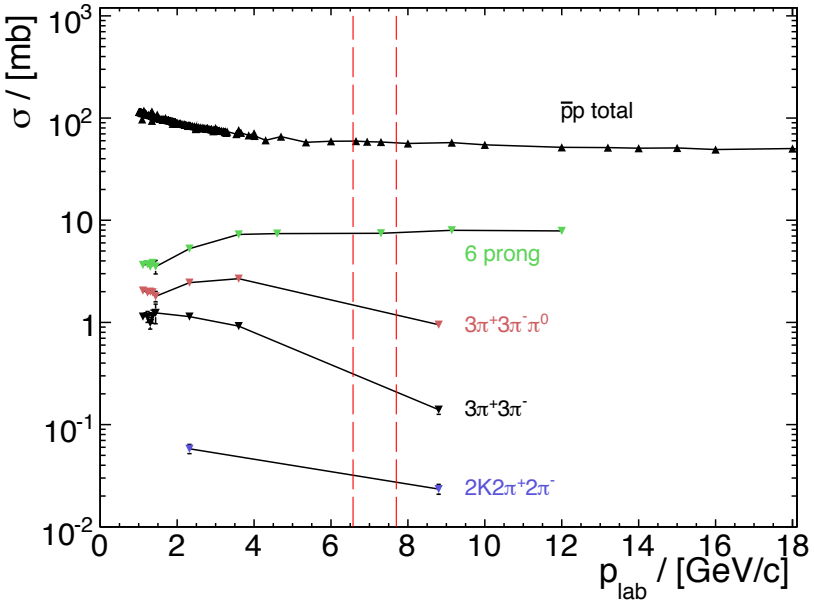

Figure 4.20: Collection of non-resonant 6-prong cross-sections in the $\overline{p}p$ reaction, depending on the antiproton momentum [18].

well D mesons are identified overall in the background. A common way of referring to the signal significance is the signal-to-background ratio which is calculated from the expected cross-sections and the suppression factors according to detector acceptance and reconstruction efficiency.

Data on direct D meson production from the $\overline{p}p$ reaction are sparse and cross-sections will also have to be measured by $\overline{\text{P}}$ANDA. One estimate on the cross-section is done by the quark-gluon string model (QGSM) with $\sigma_{\overline{p}p\to D\overline{D}} \approx 4 \cdot 10^{-8}$ b [64]. The branching fractions of the secondary decays are $BR_{D^0\to K^-\pi^+} = 3.89\%$ and $BR_{D^+\to K^-2\pi^+} = 9.4\%$ [63] for the neutral and charged mesons, respectively. Because the full inclusive channels require both secondary decays to follow the same (charge conjugated) branches the inclusive branching fractions are:

$$BR_{D^0\overline{D}^0\to K^+K^-\pi^+\pi^-} = (BR_{D^0\to K^-\pi^+})^2 = 0.15\%$$

$$BR_{D^+D^-\to K^+K^-2\pi^+2\pi^-} = (BR_{D^+\to K^-2\pi^+})^2 = 0.88\%.$$

Many D decay channels will have to be considered simultaneously for a high efficiency when measuring e.g. a charmonium state.

Background events mainly originate from the non-resonant production and "combinatorics". The latter occur not due to the final state combinations which can build up the decay tree but rather from spurious tracks found by the pattern recognition. A better cleanup procedure to remove spurious tracks is under development. Non-resonant channels were measured only at a few antiproton momenta. Figure 4.20 shows the cross-sections of selected six-prong channels[3]. It becomes clear that not

[3] final states with six charged particles

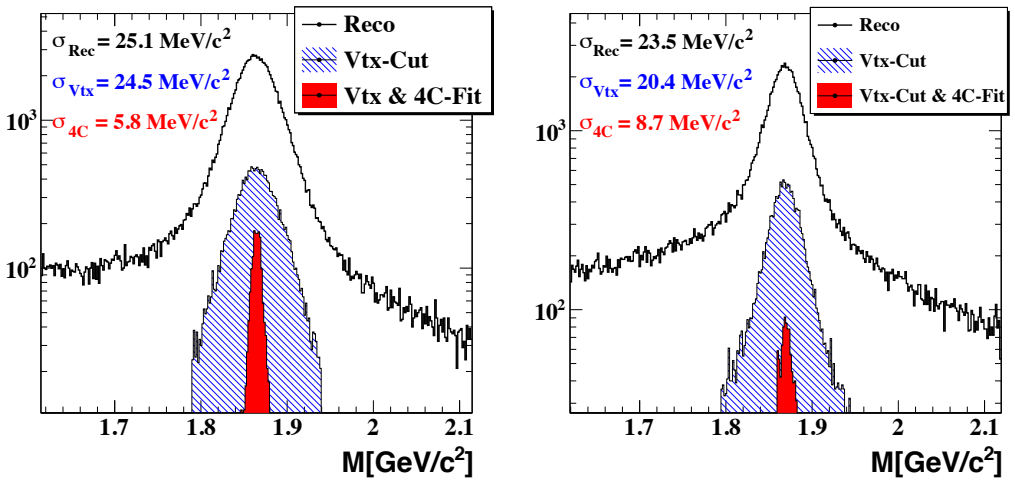

Figure 4.21: Mass resolution for neutral (left) and charged (right) D mesons. The effect of the background reduction is shown in three stages, the raw reconstruction, mass and vertex selected events and finally with the 4C fit. Mass resolutions are better than 10 MeV/c^2.

only the final state of the signal channel will contribute but also other channels with misidentified particle species. Small inefficiencies will produce significant contributions due to the high cross-sections of other channels, e.g. $\bar{p}p \to 3\pi^+3\pi^-$. The cross-section for the direct production of the final state can be approximated with $\sigma_{\mathrm{NR}} \approx 8.5\,\mu\mathrm{b}$ for the neutral and $\sigma_{\mathrm{NR}} \approx 23.4\,\mu\mathrm{b}$ for the charged D's by measurements at 8.8 GeV/c antiproton momentum [65].

Event rates of the signal and the background types are proportional to their production cross-section, modified by the branching ratios, and then decreased by the efficiency from reconstruction and selections of the analysis ϵ (see table 4.7). The signal-to-background ratio is calculated by

$$S/B = \frac{\epsilon_{\mathrm{signal}} \cdot \sigma_{\mathrm{signal}} \cdot BR_D^2}{\epsilon_{\mathrm{NR}} \cdot \sigma_{\mathrm{NR}} + \epsilon_{\mathrm{combin.}} \cdot \sigma_{\mathrm{signal}} \cdot BR_D^2} \tag{4.7}$$

For the neutral D mesons the signal-to-background ratio is $S/B = 0.012$ and for the charged D's $S/B = 0.055$. These results have to be improved strongly in order to achieve precise measurements in the charm sector. Several issues can be identified already to help the reconstruction. First, the tracking algorithm is being developed further. Especially the track finding of tracks further away from the interaction point and a tuned cleanup procedure will increase efficiency and purity of the signal events. To aid the background reduction on the analysis level a more precise vertexing than the POCA finder has to be employed, which will allow a tighter vertex selection. Because the D decay vertices are more abundant close to the interaction point this will find much more D mesons in pairs, which is one of the conditions to be able to use the 4C fitter.

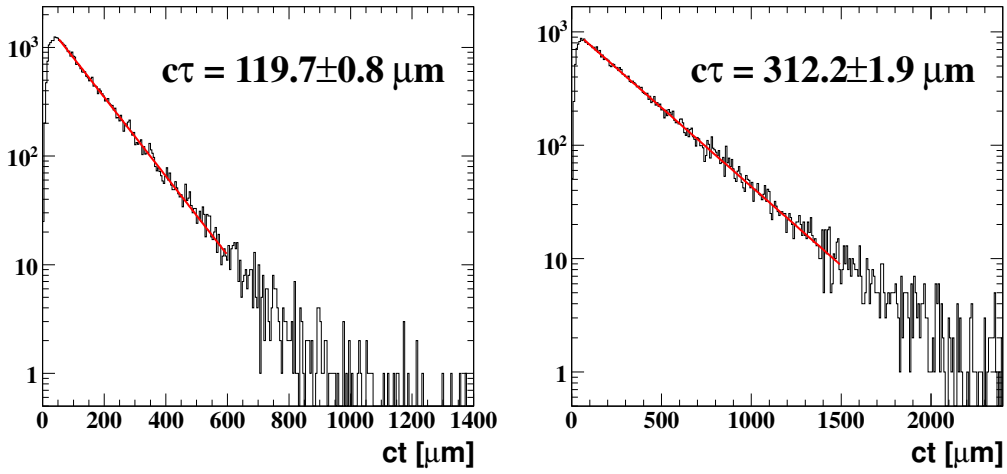

Figure 4.22: Decay length reconstruction for neutral (left) and charged (right) D mesons. PDG values are $c\tau = 122.9\,\mu\text{m}$ for $D^0/\overline{D}^0$ and $c\tau = 311.8\,\mu\text{m}$ for D^+/D^- [63].

Mass Resolution Combining the four-momenta from the kaons and pions defines the four-momentum of the D meson. The invariant masses of D^+D^- and $D^0\overline{D}^0$ are plotted in figure 4.21 showing resolutions of about $25\,\text{MeV}/c^2$ and $23\,\text{MeV}/c^2$, respectively. Subtracting background events outside of the $150\,\text{MeV}/c^2$ mass window and cutting on the vertex improves the resolution just slightly. However the yield of true signal events is much higher. Employing the 4C kinematic fit, which is adding the information on the beam four-momentum, the resolution improves strongly to $5.8\,\text{MeV}/c^2$ and $8.7\,\text{MeV}/c^2$ for the charged and neutral D mesons. For these very good resolutions there has to be considered that the real particle identification will introduce inefficiencies and additional background. Additionally the beam four-momentum used in the 4C fit is produced at a design accuracy of $\Delta p/p \approx 10^{-4}$. For a $9\,\text{GeV}/c$ beam this will be about $1\,\text{MeV}/c$, an effect neither negligible nor dominant.

Decay Length Measuring the decay length of the D mesons gives an estimateon how well the detector and its reconstruction tools are understood. The distances of the decay vertices to the interaction point are the actual flight paths $d = \gamma ct$ of neutral particles in the laboratory system. For charged D mesons the approximation of straight line tracks is made because the distances to the decay spot are relatively short (still inside the beam pipe vacuum). For the particles that distances are seen as $ct = d/\gamma$ which are distributed exponentially, folded with a Gaussian due to the resolution. Figure 4.22 shows these distributions of ct in the case of the neutral and charged D mesons. Because the tracking procedure yields reconstruction efficiencies depending on the decay vertex, a correction for that efficiency has been applied beforehand. Using an exponential fit to the slope, the decay length $c\tau$ is obtained. For the neutral D mesons $c\tau = (119.7 \pm 0.8)\,\mu\text{m}$ which agrees with the PDG literature, $c\tau = 122.9\,\mu\text{m}$ [63], which is also used by the decay model in the beginning. In the charged case the decay length yields $c\tau = 312.2 \pm 1.9\,\mu\text{m}$ which agrees with the literature ($c\tau = 311.8\,\mu\text{m}$), too.

Chapter 5

Conclusions and Outlook

Simulations for the $\overline{\text{P}}$ANDA experiment require detailed software descriptions of the subsystems. For the MVD and other systems based on silicon sensors such a software has been designed, developed and intensively tested. Detailed studies have been performed to monitor the MVD performance as a standalone system and integrated in the whole $\overline{\text{P}}$ANDA setup. Experimental data was used to verify the detector description as well as to prove the concept of using one and the same reconstruction as the simulations do.

Three vertexing tools have been adapted and implemented in PandaRoot. Detailed studies were performed to test the algorithms as well as the MVD capabilities in depth. The importance of a good vertexing has been shown with a physics benchmark channel.

The packages and tools from this work are already used with great success in the $\overline{\text{P}}$ANDA simulations.

In the future the simulations of the MVD will mainly focus on the newly developed time ordered simulations in PandaRoot. Questions on how event pileup and data rates can be handled in a realistic environment and in connection to other subsystems with differing timing characteristics have to be answered. Magnetic field effects on the hit reconstruction have to be studied, preferably with measurements, e.g. from the Tracking Station. It is foreseen to implement the MVD reconstruction into hardware, most likely into FPGA's. The feasibility has to be investigated, especially for computing-intensive algorithms, such as tracklet finding or the top-bottom correlation for strip sensors.

For the vertexing tools several features are foreseen to be added. A better treatment of neutral particles in the fast and full vertex fit is needed, adding a small contribution by pointing restrictions form EMC and DIRC hits. The possibility to automatically find the complete set of vertices in an ensemble of tracks is necessary for event filters on the analysis level and maybe even before to select for secondary decays more efficiently. Furthermore the fit is planned to support a pointing constraint to the interaction zone, which will be known precisely through vertex reconstruction of non-resonant background events.

List of Figures

List of Tables

Bibliography

[1] PANDA Collaboration. Technical Design Report for the: PANDA Micro Vertex Detector. *ArXiv e-prints*, July 2012.

[2] `http://en.wikipedia.org/wiki/Moore's_law`, last visited June 2012.

[3] The PANDA Collaboration. Technical progress report, 2005.

[4] The PANDA Collaboration. Physics Performance Report for PANDA: Strong Interaction Studies with Antiprotons. 2009.

[5] Baseline Technical Report, subproject HESR. Technical report, Gesellschaft für Schwerionenforschung (GSI), Darmstadt, 2006.

[6] Th. Würschig. *Design Optimization of the PANDA Micro-Vertex-Detector for High Performance Spectroscopy in the Charm Quark Sector*. PhD thesis, Universität Bonn, 2011.

[7] Kai-Thomas Brinkmann, Paola Gianotti, and Inti Lehmann. Exploring the Mysteries of Strong Interactions - The PANDA Experiment. *Nuclear Physics News*, 16(1):15–18, 2006.

[8] R. Muto, J. Chiba, H. En'yo, Y. Fukao, H. Funahashi, H. Hamagaki, M. Ieiri, M. Ishino, H. Kanda, M. Kitaguchi, S. Mihara, K. Miwa, T. Miyashita, T. Murakami, T. Nakura, M. Naruki, K. Ozawa, F. Sakuma, O. Sasaki, M. Sekimoto, T. Tabaru, K. H. Tanaka, M. Togawa, S. Yamada, S. Yokkaichi, and Y. Yoshimura. Evidence for In-Medium Modification of the ϕ Meson at Normal Nuclear Density. *Phys. Rev. Lett.*, 98:042501, Jan 2007.

[9] L. Äystö et al. An international accelerator facility for beams of ions and antiprotons. Conceptual design report, GSI, Darmstadt, 2001.

[10] W. Erni et al. Technical Design Report for the PANDA Solenoid and Dipole Spectrometer Magnets. 2009.

[11] HESR-Project. Construction of a glue/charm-factory at gsi. Letter of intent, Darmstadt, 1999.

[12] HESR-Project. Contributions to the scientific case. Letter of intent, GSI, Darmstadt, 1999.

[13] PANDA Collaboration. Technical Design Report for the: PANDA Straw Tube Tracker. *ArXiv e-prints*, May 2012.

[14] *Simulations of Luminosity monitor for PANDA experiment*, volume 56. Proceedings of the DAE Symp. on Nucl. Phys., 2011.

[15] A. Sanchez Lorente. Double Λ-hypernuclei at the PANDA experiment. *Hyperfine Interactions*, page 326, November 2011.

[16] G.F. Knoll. *Radiation detection and Measurement*. John Wiley & Sons, 3rd edition, 2000.

[17] W.R. Leo. *Techniques for Nuclear and Pparticle Physics Experiments*. Springer, second revised edition edition, 1987/1994.

[18] René Jäkel. *Resolution Studies for the Micro Vertex Detector of the PANDA Experiment and the Reconstruction of Charmed Mesons for Specific Hadronic Channels*. PhD thesis, TU Dresden, 2009.

[19] Rene Brun and Fons Rademakers. Root - an object oriented data analysis framework. *Nucl. Inst. & Meth. in Phys. Res.*, A 389:81–86, 1996. Proceedings AIHENP'96 Workshop, Lausanne, Sep. 1996.

[20] Root - an object oriented data analysis framework. `http://root.cern.ch`, last visited June 2012.

[21] Geant - detector description and simulation tool. `http://wwwasd.web.cern.ch/wwwasd/geant/`, last visited Nov. 2011.

[22] J. Allison et al. Geant4 developments and applications. *Nuclear Science, IEEE Transactions on*, 53(Issue:1):270 – 278, Feb. 2006.

[23] Geant4: An object oriented toolkit for simulation in HEP. `http://geant4.cern.ch`, last visited Nov. 2011.

[24] S. Agostinelli et al. Geant4–a simulation toolkit. *Nuclear Instruments and Methods in Physics Research Section A: Accelerators, Spectrometers, Detectors and Associated Equipment*, 506(3):250 – 303, 2003.

[25] Torbjorn Sjostrand, Stephen Mrenna and Peter Z. Skands. A brief introduction to PYTHIA 8.1. *Comput. Phys. Commun.*, 178:852–867, 2008.

[26] Pythia website. `http://home.thep.lu.se/~torbjorn/Pythia.html`, last visited Nov. 2011.

[27] I. Frohlich et al. Pluto: A Monte Carlo Simulation Tool for Hadronic Physics. *PoS*, ACAT2007:076, 2007.

[28] Short introduction to pluto on the hades web. `http://www-hades.gsi.de/computing/pluto/html/snapshot.html`, last visited Nov. 2011.

[29] M.Al-Turany. "FairRoot framework". Talk at HIC for FAIR Workshop, Feb. 2010.

[30] *EvtGen documentation.* `http://www.slac.stanford.edu/~lange/EvtGen`, last visited Nov 22, 2011.

[31] A. Capella et al. Dual parton model. *PHYSICS REPORTS*, 236(4&5):225–329, 1994.

[32] S.A. Bass et al. Microscopic Models for Ultrarelativlstic Heavy Ion Colllslons. *Prog. Part. Nucl. Phys.*, 41:255–369, 1998.

[33] M. Bleicher et al. Relativistic hadron–hadron collisions in the ultra-relativistic quantum molecular dynamics. *Nucl. Part. Phys.*, 25:1859–1896, 1999.

[34] Pablo Yepes. A fast track pattern recognition. *Nuclear Instruments and Methods in Physics Research Section A: Accelerators, Spectrometers, Detectors and Associated Equipment*, 380(3):582 – 585, 1996.

[35] R. Frühwirth, A. Strandlie, and W. Waltenberger. Helix fitting by an extended riemann fit. *Nuclear Instruments and Methods in Physics Research Section A: Accelerators, Spectrometers, Detectors and Associated Equipment*, 490(1–2):366–378, 9 2002.

[36] C. Höppner, S. Neubert, B. Ketzer and S. Paul. A novel generic framework for track fitting in complex detector systems. *Nucl. Instr. Meth.*, A620(2-3):518 – 525, 2010.

[37] R.E. Kalman. A new approach to linear filtering and prediction problems. *J. Basic Eng.*, 82:34, 1961.

[38] R. Frühwirth. Application of Kalman filtering to track and vertex fitting. *Nucl. Instr. Meth.*, A262(2-3):444 – 450, 1987.

[39] V. Innocente et al. The GEANE program. CERN Program Library, 1991. W5013-E.

[40] A. Fontana, P. Genova, L. Lavezzi and A. Rotondi. Track following in dense media and inhomogeneous magnetic fields. *PANDA report PV/01-07*, 2007.

[41] L. Lavezzi. *The fit of nuclear tracks in high precision spectroscopy experiments.* PhD thesis, Università degli Studi di Pavia, 2007.

[42] Marcel Kunz. Rho: A set of analysis tools for ROOT. `http://savannah.fzk.de/websites/hep/rho/`, last visited Oct. 2011, 2001.

[43] Beta: A package for analysis access to reconstructed data. `http://www.slac.stanford.edu/BFROOT/www/Computing/Offline/Beta/Beta.html`, last visited June 2012.

[44] ISO 10303-1:1994. Industrial Automation Systems and Integration Product Data Representation and Exchange - Overview and Fundamental Principles. *International Standard*, ISOTC184/SC4, 1994.

[45] Cadconverter documentation. `http://panda-wiki.gsi.de/cgi-bin/view/Computing/CadConverter`, last visited June 2011.

[46] Th. Würschig. Basic Conventions for the CAD-Modelling of the Micro-Vertex-Detector. *Panda MVD-note*, 003, 2008.

[47] S. Bianco et al. Measurements with a Si-strip telescope. In *PoS (RD11) 025*, 2011.

[48] Gerhard Lutz. *Semiconductor Radiation Detectors*. Springer, 2007.

[49] David-Leon Pohl. Charakterisierung eines Silizium-Pixel-Auslesechips für den PANDA Mikro-Vertex-Detektor. Master Thesis (M.Sc./Physics), Ruhr-Universität Bochum.

[50] R.A. Boie V. Radeka. Centroid finding method for position-sensitive detectors. *IEEE Trans. Nucl. Sci.*, 178:543–554, 1980.

[51] R. Frühwirth, A. Strandlie and W. Waltenberger. Helix fitting by an extended riemann fit. *Nuclear Instruments and Methods in Physics Research Section A: Accelerators, Spectrometers, Detectors and Associated Equipment*, 490(1-2):366–378, 2002.

[52] Pierre Billoir and S. Qian. Fast vertex fitting with a local parametrization of tracks. *Nucl.Instrum.Meth.*, A311:139–150, 1992.

[53] P. Avery. Applied fitting theory I: General least squares theory. CBX 91–72.

[54] P. Avery. Applied fitting theory II: Determining systematic effects by fitting. CBX 91–73.

[55] P. Avery. Applied fitting theory III: Non-optimal least squares fitting and multiple scattering. CBX 91–74.

[56] P. Avery. Applied fitting theory IV: Formulas for track fitting. CBX 92–45.

[57] R. Schnell et al. FPGA-based readout for double-sided silicon strip detectors. In *JINST 6 C01008*, 2011.

[58] L Jones. *APV25-S1: User guide version 2.2*. RAL Microelectronics Design Group, Chilton, 2001.

[59] S. Bianco. Characterization of the panda micro-vertex-detector and analysis of the first data measured with a tracking station. In *Nuclear Science Symposium Conference Record (NSS/MIC), 2010 IEEE*, pages 1149 –1152, 30 2010-nov. 6 2010.

[60] M. Mertens, Th. Würschig and R. Jäkel. Count rate studies for the Micro-Vertex-Detector. *PANDA MVD-note*, 004, 2010.

[61] L. Zotti, D. Calvo and R. Kliemt. Rate study in the pixel part of the MVD. *PANDA MVD-note*, 007, 2011.

[62] G. L. Bashindzhagyan and N. A. Korotkova. The use of capacitive charge division in silicon microstrip detectors. *Instruments and Experimental Techniques*, 49(3):318–330, 2006.

[63] K. Nakamura et al. (Particle Data Group). Review of particle physics. *J. Phys.*, G 37:075021, 2010.

[64] A.B. Kaidalov and P.E. Volkovitsky. Binary reactions in anti-p p collisions at intermediate-energies. *Z.Phys.*, C63:517–524, 1994.

[65] J. C. Hill et al. Strange particle production in anti-p p annihilations at 8.8-GeV/c. *Nucl. Phys.*, B227:387, 1983.

Acknowledgements

I want to thank my supervisor, Professor Brinkmann, for the continuity and support through a time of many changes. Thanks go to my colleagues, especially Hans, René, Thomas, Simone and Andreas, who made these times fun ones. I'm especially grateful to my wife Franza for her steady support and love.

Ralf Kliemt